

New Approaches to Boost SABRE Signals

by

Xiaoqing Li

Department of Physics
Duke University

Date: _____

Approved:

Warren S. Warren, Supervisor

Martin Fischer

Phillip Barbeau

Ying Wu

Bastiaan Driehuys

Thesis submitted in partial fulfillment of
the requirements for the degree of Doctor
of Philosophy in the Department of
Physics in the Graduate School
of Duke University

2023

ABSTRACT

New Approaches to Boost SABRE Signals

by

Xiaoqing Li

Department of Physics
Duke University

Date: _____

Approved:

Warren S. Warren, Co-Supervisor

Martin Fischer, Co-Supervisor

Phillip Barbeau

Ying Wu

Bastiaan Driehuys

An abstract of a thesis submitted in partial
fulfillment of the requirements for the degree
of Doctor of Philosophy in the Department of
Physics in the Graduate School of
Duke University

2023

Copyright by
Xiaoqing Li
2023

Abstract

SABRE (Signal Amplification by Reversible Exchange) methods provide a simple, fast, and cost-effective method to hyperpolarize a wide variety of molecules in solution, and have been demonstrated with protons and, more recently, with heteronuclei (X-SABRE). In this dissertation, we first present oscillating pulse SABRE that use magnetic fields far away from the resonance condition of continuous excitation and can commonly triple the polarization. An analysis with average Hamiltonian theory indicates that the oscillating pulse, in effect, adjusts the J-couplings between hydrides and target nuclei and that a much weaker coupling produces maximum polarization. This theoretical treatment, combined with simulations and experiment, shows substantial magnetization improvements relative to traditional X-SABRE methods. It also shows that, in contrast to most pulse sequence applications, waveforms with reduced time symmetry in the toggling frame make magnetization generation more robust to experimental imperfections.

A high-pressure SABRE approach is presented to enhance the exchange rate of the dihydride by increasing its concentration. To achieve this, two methods are proposed to improve the concentration of hydrogen gas: the brute-force high-pressure method and the supercritical SABRE method. The brute-force approach has been found to effectively increase the polarization by over three times. Further numerical analysis has shown that combining the oscillating pulse technique with the high-pressure method, and

implementing temperature control, can effectively further enhance the polarization to higher levels.

Contents

Abstract.....	iv
List of Tables	viii
List of Figures.....	ix
Acknowledgements	xiii
Chapter 1: Introduction	1
Chapter 2: The Basis of NMR and SABRE.....	6
2.1 The origin and theory of NMR	6
2.2 The Application of NMR	23
2.3 SABRE and Parahydrogen.....	25
Chapter 3: Oscillating Pulse Sequence SABRE	40
3.1 Theoretical Perspective of Pulse Sequence.....	43
3.1.1 Hamiltonian in the Interaction Frame	43
3.1.2 Average Hamiltonian	46
3.1.3 Correctly Attenuated J-coupling Enhances Polarization	55
3.1.4 Symmetry Reduces Robustness	58
3.2 Numerical and Experimental Verification	62
3.3 Validity of Level Anti-crossings.....	67
3.4 Robustness to Exchange Rate	71
3.5 Some Expansions of Oscillating Pulse SABRE.....	73
3.6 Conclusion and Outlook	79
Chapter 4: High-pressure SABRE	81

4.1 Ways to Improve the Accessibility of Dihydrogen.....	83
4.2 Experimental Results of Brute-force High-pressure SABRE.....	90
4.3 Experimental Results of Super-critical SABRE	97
4.4 Combination of High-pressure and Oscillating Pulse.....	103
4.5 Conclusion and Outlook	106
Chapter 5: Attempt to Polarize Xenon with SABRE	108
5.1 Motivation.....	108
5.2 Current Experimental Observations.....	111
Chapter 6: Conclusions	120
References	123

List of Tables

Table 4.1: Critical parameters of some commonly used solvents	86
---------------------------------------------------------------------	----

List of Figures

Figure 1.1: Comparison of thermal polarization and hyperpolarization.....	1
Figure 1.2: Polarization as a function of both the offset field and the diminished effective J-coupling between the dihydride and the target nuclei.....	4
Figure 2.1: A schematic diagram shows how a 90° pulse rotates a spin initially along the z-axis in both the Zeeman interaction frame and the lab frame.....	12
Figure 2.2: Schematic interpretation of J-coupling in terms of a two-spin system with the chemical shift difference much larger than the J-coupling.....	15
Figure 2.3: The basic $90^\circ x$ pulse-acquire NMR experiment	23
Figure 2.4: Population of parahydrogen and orthohydrogen as a function of temperature	28
Figure 2.5: Schematical representation of generation of hyperpolarized ^{15}N labelled acetonitrile.....	30
Figure 2.6: Molecular diagram of SABRE complex with acetonitrile as the substrate and the pyridine as the co-ligand	31
Figure 2.7: The population of both spin-up and spin down states in two subspaces of the three-spin system and the polarization as a function of time.....	33
Figure 2.8: Molecular diagram of SABRE complex with pyridine as the substrate.....	37
Figure 2.9: Polarization of the target nuclei as a function of time.....	38
Figure 2.10: Magnetic field profile of a AA'B system.....	39
Figure 3.1: Pulse sequences for enhanced SABRE excitation.....	41
Figure 3.2: Schematic representation of the unbalanced square pulse and the final polarization level simulation with DMEx.....	42
Figure 3.3: Polarization of a AA'BB' system varies with the square pulse period and the offset field.	51
Figure 3.4: The matrix elements of the higher order average Hamiltonian in both the case of square pulses and ramp pulse changes as a function of the pulse period.....	54

Figure 3.5: Curves of M and N and the final polarization as a function of $\frac{\theta}{\pi}$	57
Figure 3.6: Depiction of how M_0 , N_0 , and $\sqrt{M_0^2 + N_0^2}$ vary as a function of the pulse period and/or pulse amplitude.....	59
Figure 3.7: Examples of center axisymmetric pulses and a coordinate transformation by rotating the original rectangular coordinate system an angle θ to the new system.	60
Figure 3.8: Experimental procedure of SABRE-SHEATH.	63
Figure 3.9: Experimental validation of the theoretical predictions.....	64
Figure 3.10: Level crossing and level anti-crossing of a two -level system.....	68
Figure 3.11: The optimal magnetic field of CW SABRE-SHEATH varies as the chemical exchange rates of both the dihydride and the target substrate	69
Figure 3.12: Eigenvalues as a function of the offset field	69
Figure 3.13: The prediction of LAC agrees with experimental optimum.....	70
Figure 3.14: Different optimal polarization conditions caused by different exchange rates of substrate.	71
Figure 3.15: Polarization generated by quantum evolution of the 3-spin system.....	73
Figure 3.16: Polarization of a 3-spin system undergoing a square pulse as a function of the offset field	74
Figure 3.17: A depiction of how the final polarization varies with the period of a sine wave sequence	76
Figure 3.18: A numerical simulation indicating that the polarization varies periodically with the offset field	76
Figure 3.19: A combination of square pulse and a constant field which have the identical amplitude yields a unidirectional oscillating square pulse	77
Figure 3.20: A two-state square pulse and the experimental verification of its signal enhancement	78

Figure 3.21: Polarization varies as the pulse period of a unidirectional sine wave and a unidirectional triangle wave.....	79
Figure 4.1: Maximum polarization as a function of the chemical exchange rates	82
Figure 4.2: SABRE signal decreases as the increased probability of dihydrogen rebinding and varies with the flow rate of hydrogen gas	83
Figure 4.3: Carbon dioxide pressure-temperature phase diagram	85
Figure 4.4: High-pressure system setup.....	87
Figure 4.5: Schematic representation of the highly increased concentration of hydrogen gas.	89
Figure 4.6: Signal build-up processes of both the open and closed SABRE system.....	90
Figure 4.7: Proton spectra of SABRE solutions with and without SABRE catalyst	92
Figure 4.8: Schematic representation of methanol binding to the catalyst center and the NMR spectrum of the dihydride	94
Figure 4.9: Signal of the high-pressure SABRE varies with the gas pressure.....	96
Figure 4.10: Proton spectrum obtained from a super-critical SABRE sample.	98
Figure 4.11: Molecular diagram of the phosphorous catalyst and the proton spectrum of the new supercritical SABRE sample including this phosphorous catalyst	99
Figure 4.12: Hyperpolarized hydride signal of the new SABRE system	100
Figure 4.13: Illustration of the polarization of the supercritical SABRE changes with temperature, exposure time in the low field, and magnitude of the low field	101
Figure 4.14: Compare the signal build-up curves of four different scenarios	104
Figure 4.15: Polarization build-up process with respect to different exchange rates	106
Figure 5.1: Electron configuration of xenon.....	110
Figure 5.2: Molecular diagram of the tree available SABRE catalysts	112
Figure 5.3: A comparison of the absorption spectra of the sample before and after the addition of xenon gas	112

Figure 5.4: Proton spectra and ^{31}P spectra of the SABRE sample before and after the addition of xenon	114
Figure 5.5: Xenon spectrum of the SABRE sample.	115
Figure 5.6: Illustrations of the ^{31}P decoupled proton spectrum and the proton decoupled ^{31}P spectrum of the SABRE sample in the presence of the xenon	116
Figure 5.7: 2D COSY of the SABRE sample with xenon	118
Figure 5.8: 2D DOSY of the SABRE sample with xenon.....	119

Acknowledgements

I would like to express my deepest gratitude to my advisor, Dr. Warren S. Warren, for his guidance, support, and encouragement throughout my research. I would also like to thank the members of my research group, Dr. Martin Fischer, Dr. Jacob Lindale, Dr. Shannon Eriksson, Dr. David Grass, Dr. Guannan Zhang, Dr. Xiaomeng Jia, Dr. Yuheng Liao, Yue Zhou, Ge Chen, Heidi Kastenholz, Finn Tran, Luke Everhart, Loren Smith, Matthew McEneaney, Rajiv Raman, for their valuable inspire, collaboration and help. Additionally, I am grateful to NIH for providing the financial support that made this research possible.

Chapter 1: Introduction

The inherent limitation of nuclear magnetic resonance (NMR) is its low sensitivity, which arises from the small energy difference between the Zeeman splitting and thermal energy. Consequently, the resulting equilibrium fractional magnetization is typically low, ranging from 10^{-5} to 10^{-6} . However, there are hyperpolarization techniques that can produce significantly higher magnetization by obtaining spin order from other sources (Fig. 1.1). Three major methods have evolved over the last several decades:

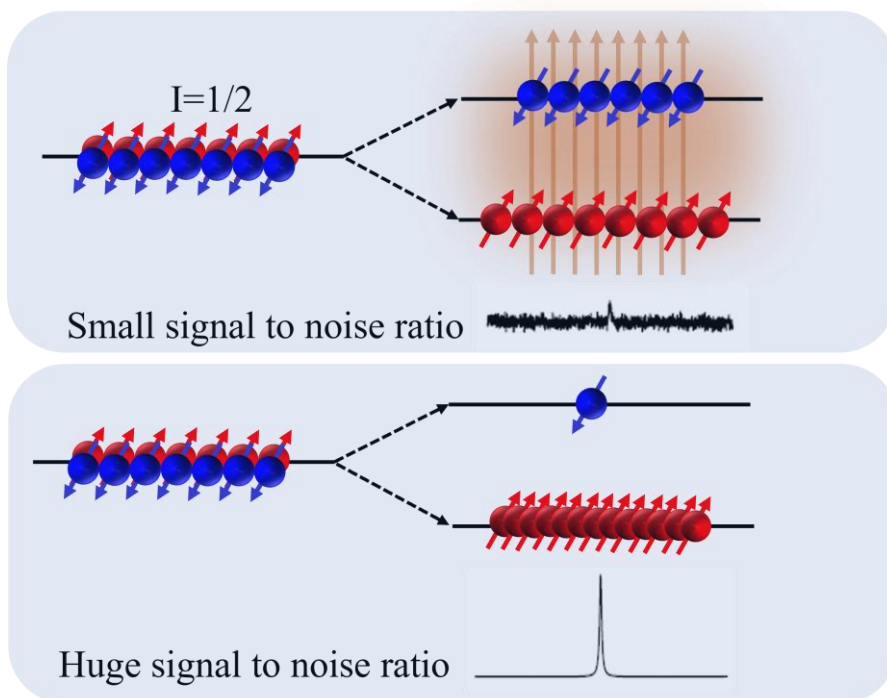


Figure 1.1: Comparison of thermal polarization and hyperpolarization dissolution dynamic nuclear polarization (d-DNP)^{1, 2}, which derives nuclear spin order from unpaired electrons, spin exchange optical pumping (SEOP)³, which derives it indirectly from circularly pumped optical transitions, and hydrogenative para-hydrogen-

induced polarization (PHIP)^{4,5}, which derives spin order from parahydrogen, the singlet isomer of the H₂ molecule. Despite their benefits, all these methods have limitations, which have prompted ongoing research. For example, SEOP is limited to a few noble gases, d-DNP requires expensive hyper-polarization hardware and requires a long hyperpolarization time (often an hour or so for ¹³C and ¹⁵N), and PHIP requires a suitable precursor molecule and catalyst.

Recently, various techniques have emerged that employ reversible interactions between parahydrogen, a target molecule, and an iridium catalyst. These techniques originated from Signal Amplification By Reversible Exchange (SABRE)⁶ method and involve the exchange of both parahydrogen and target substrate with sites on the catalyst metal center in a rapid and reversible manner. At a low magnetic field strength of approximately 6 mT, J-couplings between the hydrides and protons on the bound species enable the transfer of spin order between them, leading to the spontaneous creation of excess magnetization on the target protons. Over time, a range of extended SABRE methods (X-SABRE)⁷⁻¹¹ have been developed, which have fewer experimental restrictions. One such technique is SABRE-SHEATH (Signal Amplification By Reversible Exchange in SHield Enables Alignment Transfer to Heteronuclei), which allows direct targeting of heteronuclei (such as ¹⁵N, ¹³C, ¹⁹F, and ³¹P) with much longer T₁ values than ¹H. For this technique, the optimal magnetic field strength is around 0.6 μT, so experiments are typically conducted in a magnetic shield. Other X-SABRE methods have been modified to transfer spin order directly from parahydrogen in a high field magnet¹⁰.

SABRE and X-SABRE are simpler, faster, and less expensive compared to hyperpolarization methods available commercially, and more general than PHIP. However, the amount of polarization produced at any one time is generally lower than with d-DNP or SEOP, although there is no fundamental reason why this must be true. We have recently discovered that a big part of the reason is that the novel field regime for SABRE and X-SABRE (where even heteronuclear couplings can be readily interconverted between the strong and weak coupling limits), combined with the very complex exchange dynamics, imply that the method is theoretically underexplored; there are clearly better (but nonintuitive) approaches to creating polarization than a simple continuous field. Specifically, an alternating two-field pulse sequence (both fields high, but with a small average) can produce very large SABRE enhancements.

We have conducted a systematic investigation into the use of periodic field perturbations to create enhanced magnetization with reduced sensitivity to experimental imperfections such as field inhomogeneity¹². This approach capitalizes on a significant advantage of operating in the low field regime: the ability to rapidly change the main magnetic field using simple hardware, much faster than any couplings. We first obtained general insight from average Hamiltonian theory and then performed highly precise calculations using an exact dissipative master equation treatment¹³. Optimal pulse sequences in all cases appeared non-intuitive and did not match continuous excitation, either in their peak or average field strength. In both simulations and experiments, we generated maximal magnetization ($\sim 5\%$) with a continuous $\sim 0.6 \mu\text{T}$ field, but much larger magnetization ($\sim 18\%$) was produced by a properly timed oscillating pulse with an

offset from a zero average field by approximately one-fifth that value ($\sim 0.13 \mu\text{T}$) (Fig. 1.2). An analysis using average Hamiltonian theory revealed that the oscillating pulse adjusts the J-couplings between hydrides and target nuclei, and that a much weaker coupling produces maximum polarization. This theoretical treatment, combined with

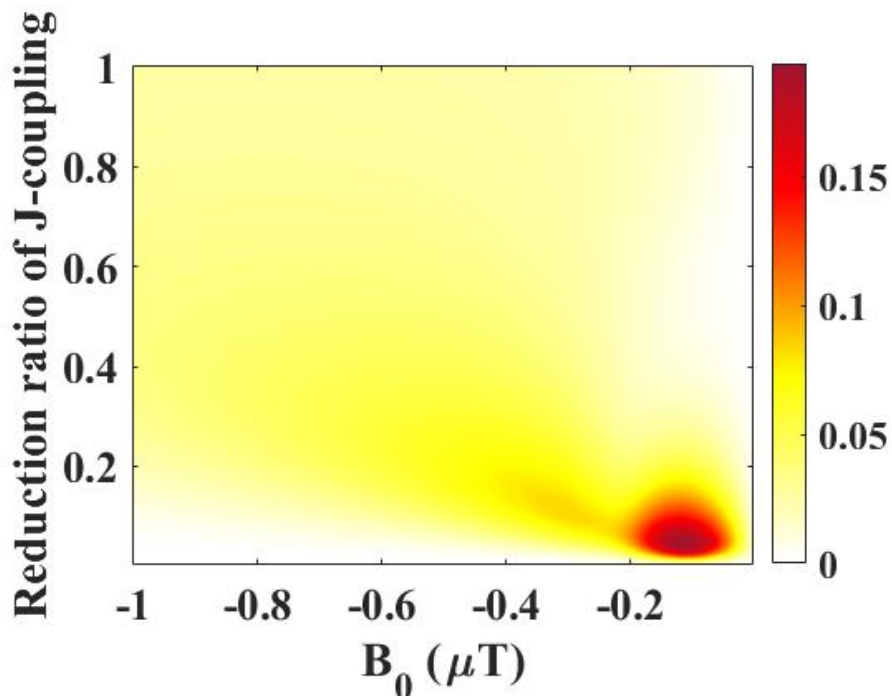


Figure 1.2: Polarization as a function of both the offset field and the diminished effective J-coupling between the dihydride and the target nuclei.

simulations and experiments, led to substantial improvements in magnetization compared to traditional X-SABRE methods. We also demonstrated that, unlike most pulse sequence applications, waveforms with reduced time symmetry in the toggling frame make magnetization generation more robust to experiment imperfections.

In the oscillating pulse sequence case, only the efficiency of the coherent quantum evolution is improved. The second part of my research is to improve the efficiency associated with the chemical exchange processes. In principle, a faster chemical exchange rate of the dihydride induced higher final polarization. Since the chemical exchange rate is positively proportional to the concentration of the component, we proposed two different methods to dramatically increase the concentration of hydrogen gas. The first one is to brutally increase the gas pressure of the hydrogen gas and then accordingly increase its solubility. Another method is to create a supercritical mixture of hydrogen gas and the SABRE solution. This approach has the advantage of the supercritical fluid being miscible with gas, thus overcoming the limitation of low gas solubility in solution. The brute-force high-pressure SABRE method resulted in a three-fold enhancement of polarization at 300 bar, but beyond this pressure, the magnetization signal exhibited a decline whose underlying reason remains unclear and necessitates further investigation. In the case of supercritical SABRE, CO₂ was utilized as the solvent due to its green nature and convenient supercritical parameters. However, it was found that CO₂ is capable of binding to the SABRE catalyst and competing with the substrate and hydrogen gas, which greatly reduces the final polarization. The ease of binding depends on the specific catalyst complex. The utilization of a more suitable SABRE catalyst for CO₂ could lead to practical applications for the supercritical SABRE method. Because the release of the SABRE solvent is straightforward through depressurizing the gas mixture, rendering it ideal for research and applications that involve biological injections.

Chapter 2: The Basis of NMR and SABRE

Nuclear magnetic resonance (NMR) is a physical phenomenon in which the magnetic moment of a nucleus, a consequence of its intrinsic spin angular momentum, precesses at a specific frequency in an added magnetic field. When the precession is perturbed by an oscillating magnetic field along a different direction the nucleus produces an oscillating magnetic field, and this is a signal that can be picked up by a receiver. An NMR spectrum is able to display detailed dynamical and structural information about molecules. NMR has become a powerful tool for a wide range of applications in physics, chemistry, biology, medicine, after decades of development¹⁴⁻¹⁷. However, it has intrinsically low sensitivity especially for heteronuclei due to the fact that the magnetic energy difference between different spin states is far less than thermal energy. Consequently, hyperpolarization NMR techniques have been developed to lift this limitation.

2.1 The origin and theory of NMR

The concept of spin had been firmly established in the 1930s after the verification with the Stern – Gerlach experiment¹⁸. In this experiment, a narrow beam of atoms is deflected into discrete directions after traversing a strong magnetic field with a gradient. The force on a dipole $\vec{\mu}$ in the magnetic field \vec{B} is given by $\vec{F} = \nabla(\vec{\mu} \cdot \vec{B})$, therefore, the deflections demonstrated the quantization of the dipole moment. The intrinsic property that causes the magnetic moment is now known as “spin” or spin angular momentum¹⁹. The magnetic moment is proportional to spin angular momentum, $\vec{\mu} = \gamma \vec{S}$, where γ is

the gyromagnetic ratio and different for each particle, which indicates that the spin angular momentum is quantized as well. A spin quantum number of m leads to $(2m+1)$ discrete states. Electron, proton, and neutron are all spin- $\frac{1}{2}$ particles. Most nuclei possess spin as well if the proton spin and the neutron spin don't cancel out, and the spin quantum number of a nucleus depends on how many protons and neutrons it has. The most widely used nuclei in NMR are spin-1/2 nuclei, such as ^1H , ^{13}C , ^{15}N , ^{19}F , ^{31}P and ^{129}Xe , and I will predominantly treat nuclei with spin-1/2 in all my work.

In quantum physics, every physical quantity is mapped to a quantum operator. Spin angular momentum is directional thus mapped to a vector operator labelled with $\hat{S} = (\hat{S}_x, \hat{S}_y, \hat{S}_z)$. Spin operators pointing in x, y, and z directions correspond to the well known Pauli matrices multiplied by $\frac{\hbar}{2}$ so that they have the dimensions of angular momentum.

$$\hat{S}_x = \frac{\hbar}{2}\sigma_x = \frac{\hbar}{2}\begin{pmatrix} 0 & 1 \\ 1 & 0 \end{pmatrix}, \quad \hat{S}_y = \frac{\hbar}{2}\sigma_y = \frac{\hbar}{2}\begin{pmatrix} 0 & -i \\ i & 0 \end{pmatrix}, \quad \hat{S}_z = \frac{\hbar}{2}\sigma_z = \frac{\hbar}{2}\begin{pmatrix} 1 & 0 \\ 0 & -1 \end{pmatrix}. \quad (2.1)$$

The two stationary spin states of each spin operator and the magnitude of their angular momentum are the eigenstates and the eigenvalues of each matrix, respectively. For

example, the two sets of eigenstates and eigenvalues of \hat{S}_z are $\left\{ \frac{\hbar}{2}; |\alpha\rangle = \begin{pmatrix} 1 \\ 0 \end{pmatrix} \right\}$ and

$\left\{ -\frac{\hbar}{2}; |\beta\rangle = \begin{pmatrix} 0 \\ 1 \end{pmatrix} \right\}$, which are known as “spin-up” and “spin-down” states. The spin

operator in an arbitrary direction

$$\vec{n} = (n_x, n_y, n_z) = (\sin \theta \cos \phi, \sin \theta \sin \phi, \cos \theta) \quad (2.2)$$

is

$$\hat{S}_n = \vec{n} \cdot \hat{S} = \frac{\hbar}{2} \begin{pmatrix} \cos \theta & \sin \theta e^{-i\phi} \\ \sin \theta e^{i\phi} & -\cos \theta \end{pmatrix}. \quad (2.3)$$

By solving the eigenstates and eigenvalues of this matrix, we obtain the spin state parallel to \vec{n} with spin angular momentum $\frac{\hbar}{2}$ and the state antiparallel to \vec{n} with spin angular momentum $-\frac{\hbar}{2}$

$$\begin{aligned} |\vec{n}; +\rangle &= \cos \frac{\theta}{2} |\uparrow\rangle + \sin \frac{\theta}{2} e^{i\phi} |\downarrow\rangle \\ |\vec{n}; -\rangle &= \sin \frac{\theta}{2} |\uparrow\rangle - \cos \frac{\theta}{2} e^{i\phi} |\downarrow\rangle \end{aligned} \quad (2.4)$$

If a spin is inserted in a magnetic field \vec{B} , the Hamiltonian (energy operator) of this spin is

$$\hat{\mathcal{H}} = -\hat{\mu} \cdot \vec{B} = -\gamma B \hat{S}_z, \quad (2.5)$$

by assuming the direction of the magnetic field is along \hat{z} . The associated time evolution unitary operator is

$$\hat{U} = \exp\left(-i \frac{\hat{\mathcal{H}} t}{\hbar}\right) = \exp\left(i \frac{\gamma B t}{\hbar} \hat{S}_z\right). \quad (2.6)$$

At time zero, a spin state pointing along the direction specified by the angles (θ, ϕ) is the upper Eq. (2.4). After time t , it evolved into

$$\begin{aligned}
|\Psi, t\rangle &= \hat{\mathcal{U}}|\Psi, 0\rangle = e^{i\gamma B t \hat{S}_z / \hbar} \left(\cos \frac{\theta}{2} |\uparrow\rangle + \sin \frac{\theta}{2} e^{i\phi} |\downarrow\rangle \right) \\
&= e^{i\gamma B t / 2} \left(\cos \frac{\theta}{2} |\uparrow\rangle + \sin \frac{\theta}{2} e^{i(\phi - \gamma B t)} |\downarrow\rangle \right),
\end{aligned} \tag{2.7}$$

in which the overall phase is negligible. The polar angle θ of the spin state stays the same, while the azimuth angle varies with frequency $-\gamma B$, which means the spin rotates about the field direction at this frequency. This precessing frequency is called the Larmor frequency and in the range of radio frequency at common field strength (1-10T).

$$\bar{\omega} = -\gamma \bar{B}. \tag{2.8}$$

The pre-degenerate energy levels $E = -\bar{\mu} \cdot \bar{B} = \bar{\omega} \cdot \bar{S}$ of a spin split with an added magnetic field because of the distinct eigenvalues of the spin operator. This phenomenon is Zeeman splitting²⁰. The energy difference between the splitting levels will be absorbed or emitted as the nucleus flips from one orientation to the other. This physical phenomenon is Nuclear Magnetic Resonance (NMR).

In 1938 Rabi et al. made the first direct measurement of nuclear magnetic moment, which was also the first observation of NMR²¹. A stream of hydrogen molecules was sent through three magnetic fields in sequence. The first and third magnetic fields were similar with the inhomogeneous one used in Stern – Gerlach experiment and the inverse of each other to refocus the split beam which were. However, the middle field is homogeneous, where the molecules were also subjected to a radio frequency (rf) electromagnetic radiation at right angles to the constant field. If the rf energy was

absorbed by the molecules, the beam was re-oriented and failed to refocus. As a result, the intensity at the detector located at the refocused spot went down.

However, making a stream of molecules is not easy or feasible for every molecule species, especially for large molecules, which limited the practicability of Rabi's technique. In 1946, Felix Bloch and Edward Mills Purcell expanded on Rabi's method by detecting the displaced macroscopical nuclear magnetization formed by the magnetic moment of each nucleus in a bulk sample instead of detecting the single magnetic moment one by one in a particle stream^{22, 23}. With this technique, NMR was demonstrated for the first time on liquids and solids. The magnetic field Bloch used consists of a time-independent z component and a circularly polarized field representing a magnetic field rotating on the (x, y) plane, which is the same as the middle field used in Rabi's experiment

$$\vec{B}(t) = B_0 \vec{z} + B_1 (\bar{x} \cos \omega t - \bar{y} \sin \omega t). \quad (2.9)$$

The spin Hamiltonian is

$$\hat{\mathcal{H}}(t) = -\gamma \left(B_0 \hat{S}_z + B_1 (\hat{S}_x \cos \omega t - \hat{S}_y \sin \omega t) \right), \quad (2.10)$$

which is time dependent. This system can be radically simplified to a time-independent one after being transformed to the Zeeman interaction frame which rotates about the z-axis with angular frequency $-\omega$. A spin state which is fixed in the lab frame rotates about the z-axis with angular frequency ω in the interaction frame. The operator that generates this rotation is $\hat{\mathcal{U}}(t) = \exp\left(\frac{i\omega t}{\hbar} \hat{S}_z\right)$. Generally, states in the original and

interactive pictures obeys a mapping rule of $|\Psi(t)\rangle = \hat{U}(t)|\Psi(0)\rangle$, and the Hamiltonian of the interaction frame could be obtained by submitting $|\Psi(t)\rangle$ into the time dependent Schrodinger equation, which is

$$\hat{\mathcal{H}}_g = \mathcal{U}^\dagger(t)\hat{\mathcal{H}}_g\mathcal{U}(t) + i\hbar\left(\frac{d\mathcal{U}}{dt}\right)\mathcal{U}^\dagger \quad (2.11)$$

Accordingly, after being transferred into the Zeeman interaction frame under the transformation of $\hat{U}(t) = \exp\left(\frac{i\omega t}{\hbar}\hat{S}_z\right)$, the Hamiltonian expressed in Eq. (2.10) becomes

$$\hat{\mathcal{H}} = (\omega_0 - \omega)\hat{S}_z + \omega'\hat{S}_x, \quad (2.12)$$

where $\omega_0 = -\gamma B_0$ and $\omega' = -\gamma B_1$. In NMR experiment $B_1 \ll B_0$ is held in the vast majority of cases. If the frequency of the oscillating field is far away from the Larmor frequency of the spin, i.e., $|\omega_0 - \omega| \gg 0$, the static magnetic field in the z-direction dominates. While, if $\omega \cong \omega_0$, the field in the x-direction dominates, and resonance happens. The x-field forces a spin to precess about x-direction at frequency ω' in the form of

$$|\Psi(t)\rangle = \exp\left(-i\frac{\omega't}{\hbar}\hat{S}_x\right)|\Psi(0)\rangle. \quad (2.13)$$

A spin initially pointing in the positive z direction, in time $\tau = \frac{\pi}{2\omega'}$, will be rotated into -y axis (Fig. 2.1 (a)). Therefore, an oscillating magnetic field rotating at a frequency close to ω_0 in the x-y plane with pulse duration of $\frac{\pi}{2\omega'}$ is a 90° pulse. When moving back to

the lab frame, $|\Psi(t)\rangle = \exp\left(i\frac{\omega_0\tau}{\hbar}\hat{S}_z\right)|\Psi(t)\rangle$, the spin is slowly rotating at ω_1 towards the x-y plane, while rapidly rotating around the z direction at ω_0 . In short, the spin spirals into the x-y plane (Fig. 2.1 (b)).

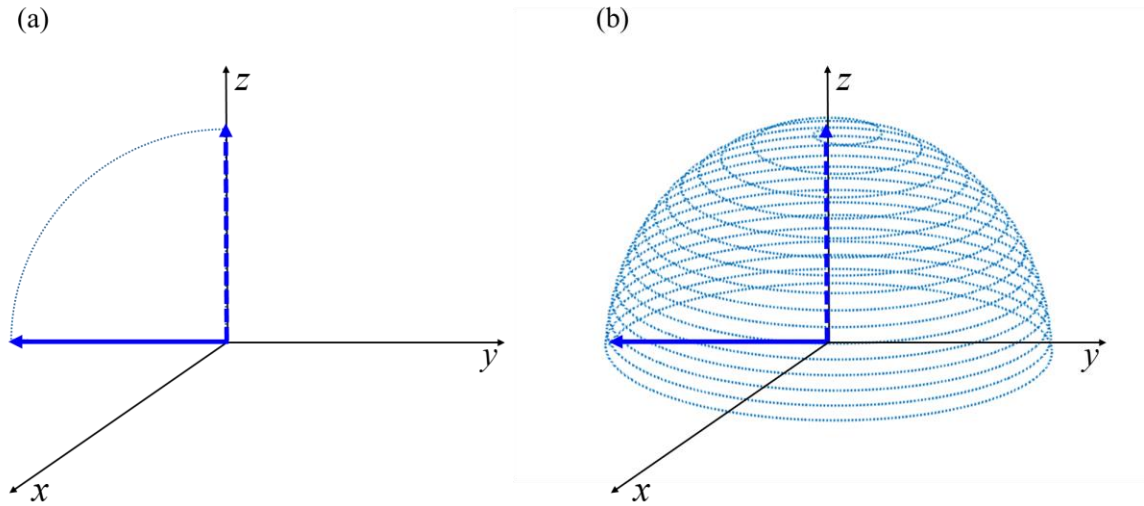


Figure 2.1: A schematic diagram shows how a 90° pulse rotates a spin initially along the z-axis in both the Zeeman interaction frame (a) and the lab frame (b). $B_1 / B_0 \sim 0.1$ illustrated here, whereas in realistic cases in high field NMR the ratio is $1/10000$.

A realistic NMR experiment involves studying a collection of interacting nuclear spins in a bulk sample. A group of spins of nuclei in a molecule is called a spin system, and the entire sample consists of an ensemble of spin systems. For a system that contains more than one particle, the dimensions of the whole system will be expanded in the form

of $\prod_i^{\text{spin}} \dim(V_i)$, where V_i is the Hilbert space (complex vector space) of the spin i . A

quantum operator acting on the whole spin system is the tensor product (symbolized as \otimes) of the quantum operator acting on each spin, which is mathematically expressed as

$$\hat{O}_{system} = \hat{O}_1 \otimes \hat{O}_2 \otimes \dots \otimes \hat{O}_n \quad (2.14)$$

If the system operator \hat{O}_{system} only makes changes to one or some of the spins and keep the rest untouched, we update the operators of the unaffected spins to identify operator \hat{E} which, for the sake of simplification, are usually all omitted.

We restrict our study to diamagnetic materials in which electrons of the molecule are all paired so the total magnetic field produced by these two electrons is zero. A theoretical treatment of a spin system starts with its spin Hamiltonian. However, the Hamiltonian of a spin system inserted in a static magnetic field is not as simple as

$$\hat{\mathcal{H}} = - \sum_i^{spins} \gamma_i \vec{B} \cdot \hat{S}_i.$$

Even though the Coulomb interactions between the nuclei and electrons

are merely produce a static structure based on the Born-Oppenheimer approximation²⁴ (the ultra-fast freedom of motion of electrons could be averaged to a constant potential),

the electrons surrounding a nucleus in a molecule serves to provide a shielding of the applied magnetic field. A shift in the resonance frequency called the chemical shift is

caused by this shielding σ in terms of $\bar{\omega} = -\gamma \bar{B}_0 (1 - \sigma)$, where the value of σ depends

on the configuration and density of electrons. In addition to surrounding electrons, a

nuclear spin also interacts with other nuclear spins though direct dipole-dipole coupling²⁵

in the form of $\frac{-\mu_0 \gamma_1 \gamma_2 \hbar}{4\pi} \left(\frac{3(\vec{S}_1 \cdot \vec{r})(\vec{S}_2 \cdot \vec{r})}{r^5} - \frac{(\vec{S}_1 \cdot \vec{S}_2)}{r^3} \right)$, where μ_0 is the magnetic constant,

\vec{r} is the vector connecting the interacting dipoles, γ_1 and γ_2 are the gyromagnetic ratios

of the two spins. The value of this term averages to zero if all orientations of the molecule

are represented, which is why the direct magnetic dipole-dipole coupling are ignored for rapidly tumbling molecules in liquids and gases.

In general, an NMR spectrum does not only consist of clean and neat singlets. Multiple lines are very common even for molecules with rapid molecular tumbling. The splitting is caused by the indirect dipole-dipole coupling (also called J-coupling or scalar coupling) between nuclei. A qualitative interpretation of J-coupling is that the shared electrons in a chemical bond connecting two nuclei are paired (anti-parallel) according to the Pauli exclusion principle, which shifts the energy of the two bonded nuclei. Either the parallel spin states are more favorable and the antiparallel states less favorable ($J > 0$) or vice versa ($J < 0$) (Fig. 2.2). In the case of $J = 0$, the energy used to flip one of the nuclear spins has nothing to do with the state of the second spin. However, when $J \neq 0$, taking $J > 0$ as an example, antiparallel nuclear spin states are lowered in energy, and parallel states are raised in energy by the same amount, so flipping one spin with the other spin pointing up is no longer degenerate with the case that the second spin pointing down, which accounts for the signal splitting. Unlike chemical shifts, the magnitude of J-coupling is independent of the applied magnetic field because it is an interaction only induced by the spin magnetic moments instead of the applied field. Also, the J-coupling interaction does not average to zero with rapid molecular tumbling, and it was shown to be of the form of a scalar product, $2\pi J_{ij} \vec{S}_i \cdot \vec{S}_j$, where J_{ij} refers to the coupling strength²⁶,²⁷. The negative and positive sign of J-coupling cannot be distinguished in the NMR spectrum, and only its magnitude is displayed.

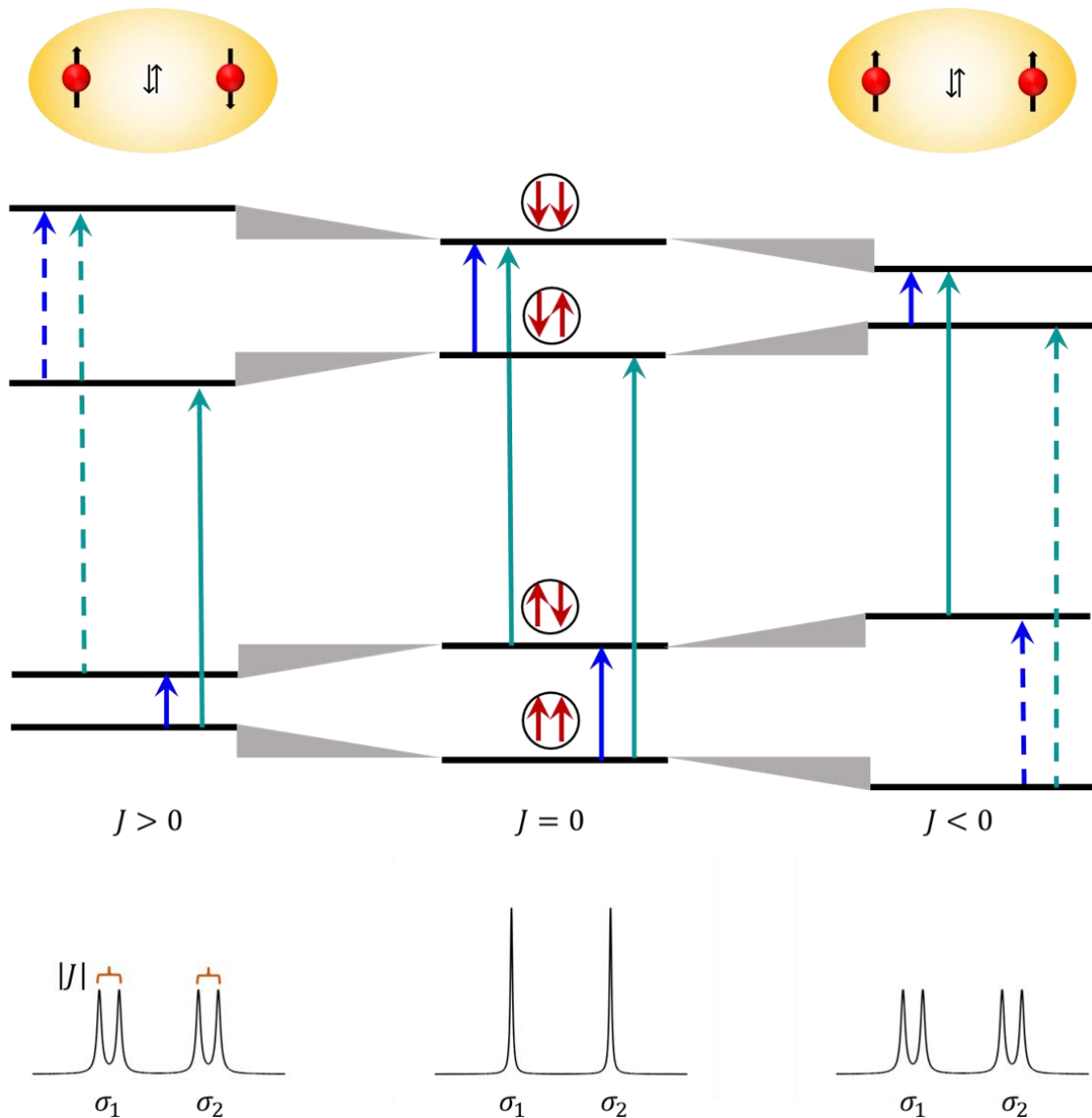


Figure 2.2: Schematic interpretation of J-coupling in terms of a two-spin system with the chemical shift difference much larger than the J-coupling $\Delta\sigma \gg J$.

Finally, the Hamiltonian of a spin system in liquid state immersed in a static magnetic field is

$$\hat{\mathcal{H}} = - \sum_i^{\text{spins}} \gamma_i B_0 (1 - \sigma_i) \hat{S}_{iz} + 2\pi \sum_i^{\text{spins}} \sum_{j < i}^{\text{spins}} J_{ij} \hat{S}_i \cdot \hat{S}_j \quad (2.15)$$

The interaction described by this simple form is limited to isotropic liquid solutions containing spin-1/2 nuclei. For solids, anisotropic liquids, and nuclei with spin greater than 1/2, the Hamiltonian becomes more complex due to the involvement of magnetic dipole and electric quadrupole interaction²⁷⁻²⁹. As is shown in Eq. (2.15), if there are no J-couplings each spin is independent and can be treated separately as a two-level system. However, due to the presence of the J-couplings the states of distinct spins are tunneled, and much more interesting spin dynamics are possible. What does a 90° pulse do to this multi-spin system? To deal with the quantum dynamics of a statistical ensemble, it is not practical to calculate the evolution of each spin. Instead, the density matrix (or density operator) $\hat{\rho}$ of the ensemble average was conceived, which is defined as

$$\hat{\rho} = \sum_i p_i |\Psi_i\rangle\langle\Psi_i|, \quad (2.16)$$

where $|\Psi_i\rangle$ are the pure states of the system, and p_i are the respective probabilities. The equation of motion for the density matrix is known as the Liouville-von Neumann equation,

$$\frac{\partial\hat{\rho}(t)}{\partial t} = -\frac{i}{\hbar}[\hat{\mathcal{H}}, \hat{\rho}(t)], \quad (2.17)$$

which derives from the Schrodinger equation, and the solution of this equation is

$$\hat{\rho}(t) = \hat{U}(t)\hat{\rho}(0)\hat{U}^\dagger(t) = \exp\left(-\frac{i\hat{\mathcal{H}}t}{\hbar}\right)\hat{\rho}(0)\exp\left(\frac{i\hat{\mathcal{H}}t}{\hbar}\right), \quad (2.18)$$

where the second equation holds for time-independent Hamiltonian or trivial time-dependent Hamiltonian (which means Hamiltonian at different instances commute with

each other $[\hat{\mathcal{H}}(t_1), \hat{\mathcal{H}}(t_2)] = 0$.

The initial density matrix is also necessary to know the evolution of the spin system. At equilibrium, the particles in a system distribute on different energy states with a certain probability. Since the identical molecules in a bulk sample are distinguishable, the energy distribution is managed by the Maxwell-Boltzmann equation³⁰

$$p_i = \frac{e^{-\varepsilon_i/(k_B T)}}{\sum_{j=1}^n e^{-\varepsilon_j/(k_B T)}}, \quad (2.19)$$

where, p_i is the probability of state i , ε_i is the energy of state i , k_B is the Boltzmann constant, T is the temperature of the system, and n is the number of all states. In the presence of an external magnetic field $B_0 \bar{z}$, the two static states $|\uparrow\rangle$ and $|\downarrow\rangle$ of a spin-1/2 nucleus have respective energy $\pm \frac{\gamma B_0 \hbar}{2}$, namely different probabilities based on Eq.

(2.19), and the density matrix is

$$\hat{\rho}_0 = \frac{1}{2} \hat{E} + \tanh\left(\frac{\gamma B_0 \hbar}{2k_B T}\right) \hat{S}_z. \quad (2.20)$$

In the absence of external magnetic field, i.e., $B_0 = 0$, the two stationary states $|\uparrow\rangle$ and $|\downarrow\rangle$ of a spin-1/2 nucleus are degenerate, and the density matrix degenerates to identity matrix which has no physical significance. According to the tensor product concept Eq. (2.14), the total density matrix of the whole spin system is the tensor production of each spin's density matrix.

Take the simplest interactional spin system, 2-spin system, as an example. With an added magnetic field $B_0\bar{z}$ the Hamiltonian of the spin system is

$$\hat{\mathcal{H}} = \omega_1\hat{S}_{1z} + \omega_2\hat{S}_{2z} + 2\pi J_{12}\hat{S}_1 \cdot \hat{S}_2, \quad (2.21)$$

where $\omega_1 = -\gamma_1 B_0(1-\sigma_1)$, and $\omega_2 = -\gamma_2 B_0(1-\sigma_2)$. The matrix form of this Hamiltonian with respect to the spin matrix in Eq. (2.1) is

$$\begin{array}{cccc} & |\alpha\alpha\rangle & |\alpha\beta\rangle & |\beta\alpha\rangle & |\beta\beta\rangle \\ \langle\alpha\alpha| & \frac{\omega_1 + \omega_2 + \pi J_{12}}{2} & 0 & 0 & 0 \\ \langle\alpha\beta| & 0 & \frac{\omega_1 - \omega_2 - \pi J_{12}}{2} & \pi J_{12} & 0 \\ \langle\beta\alpha| & 0 & \pi J_{12} & \frac{-\omega_1 + \omega_2 - \pi J_{12}}{2} & 0 \\ \langle\beta\beta| & 0 & 0 & 0 & \frac{-\omega_1 - \omega_2 + \pi J_{12}}{2} \end{array} \quad (2.22)$$

in which the spin-up $|\uparrow\rangle$ and spin-down $|\downarrow\rangle$ states are replaced by $|\alpha\rangle$ and $|\beta\rangle$, respectively, by convention, and the natural unit $\hbar=1$ is used from now on. If the two nuclei are distinguishable the two off-diagonal elements can be ignored because the chemical shift difference is much larger than the J-coupling $\omega_1 - \omega_2 \gg 2\pi J_{12}$. Consequently, the Hamiltonian is diagonalized, and the basis of this matrix are the eigenfunctions, and the diagonal elements are the eigenvalues. According to the selection rule that an allowed transition involves only the flip of one nuclear spin, the possible level transitions and their energy difference are

$$\begin{aligned}
|\alpha\alpha\rangle &\leftrightarrow |\alpha\beta\rangle, & \omega_2 + \pi J_{12} \\
|\alpha\alpha\rangle &\leftrightarrow |\beta\alpha\rangle, & \omega_1 + \pi J_{12} \\
|\beta\beta\rangle &\leftrightarrow |\alpha\beta\rangle, & \omega_1 - \pi J_{12} \\
|\beta\beta\rangle &\leftrightarrow |\beta\alpha\rangle, & \omega_2 - \pi J_{12},
\end{aligned} \tag{2.23}$$

which is the reason why the signal centered at ω_1 and ω_2 are split into doublet. However, for indistinguishable nuclei, not only they have identical chemical shift $\omega_1 = \omega_2$, but also the state $|\alpha\beta\rangle$ and $|\beta\alpha\rangle$ are superposed by the J-coupling J_{12} . Therefore, $|\alpha\beta\rangle$ and $|\beta\alpha\rangle$ are replaced by $\frac{|\alpha\beta\rangle + |\beta\alpha\rangle}{\sqrt{2}}$ (symmetric) and $\frac{|\alpha\beta\rangle - |\beta\alpha\rangle}{\sqrt{2}}$ (antisymmetric), and

the matrix form of the Hamiltonian in the new basis is

$$\begin{array}{ccccc}
& & |\alpha\alpha\rangle & \frac{|\alpha\beta\rangle + |\beta\alpha\rangle}{2} & \frac{|\alpha\beta\rangle - |\beta\alpha\rangle}{2} & |\beta\beta\rangle \\
\langle\alpha\alpha| & & \omega_1 + \frac{\pi J_{12}}{2} & 0 & 0 & 0 \\
\frac{|\alpha\beta\rangle + |\beta\alpha\rangle}{2} & & 0 & \frac{\pi J_{12}}{2} & 0 & 0 \\
\frac{|\alpha\beta\rangle - |\beta\alpha\rangle}{2} & & 0 & 0 & -\frac{3\pi J_{12}}{2} & 0 \\
\langle\beta\beta| & & 0 & 0 & 0 & -\omega_1 + \frac{\pi J_{12}}{2}
\end{array} \tag{2.24}$$

Based on the selection rule that an allowed transition only involves states with the same symmetry, there are only two possible transitions, $|\alpha\alpha\rangle \leftrightarrow \frac{|\alpha\alpha\rangle + |\beta\beta\rangle}{\sqrt{2}}$ with energy splitting ω_1 and $|\beta\beta\rangle \leftrightarrow \frac{|\alpha\alpha\rangle + |\beta\beta\rangle}{\sqrt{2}}$ with the same splitting. Therefore, for indistinguishable nuclei no signal splitting associated with J-coupling could be observed.

Above, the eigenvalues and eigenfunctions are calculated to analyze the splitting of signals. The quantum evolution method in terms of Eq. (2.18) yields the same results. Now take two distinguishable nuclei as an example. At equilibrium, the density matrix of the system is

$$\begin{aligned}\hat{\rho}_0 &= \hat{\rho}_{1_0} \otimes \hat{\rho}_{2_0} = \left(\frac{1}{2} \hat{E} + \tanh\left(\frac{\gamma_1 B_0}{2k_B T}\right) \hat{S}_{1z} \right) \otimes \left(\frac{1}{2} \hat{E} + \tanh\left(\frac{\gamma_2 B_0}{2k_B T}\right) \hat{S}_{2z} \right) \\ &= \frac{\hat{E}}{4} + \frac{1}{2} \left(\tanh\left(\frac{\omega_1}{2k_B T}\right) \hat{S}_{1z} + \tanh\left(\frac{\omega_2}{2k_B T}\right) \hat{S}_{2z} \right) + \cancel{\tanh\left(\frac{\omega_1}{2k_B T}\right) \tanh\left(\frac{\omega_2}{2k_B T}\right) \hat{S}_{1z} \hat{S}_{2z}}\end{aligned}\quad (2.25)$$

in which the non-linear term $\hat{S}_{1z} \hat{S}_{2z}$ is omitted because the interaction between a nuclear magnetic dipole and a magnetic field $\propto \gamma B_0$ generally is much smaller than the thermal

energy $k_B T$, thus $\left| \tanh\left(\frac{\omega}{2k_B T}\right) \right| \ll 1$, and all its higher orders could be omitted. This

approximation almost does not alter the trace of the matrix and is known as the high temperature approximation in NMR. In an NMR experiment an oscillating RF field with

frequency ω in Eq. (2.9) is superposed on the static field for a duration of $\frac{\pi}{2\gamma_1 B_1}$ to rotate

the bulk magnetization of the first spin species from z direction to -y direction (Eq.

(2.13)). If $\gamma_1 = \gamma_2$ i.e., spin 1 and spin 2 are the same species, with a relative strong

amplitude B_1 the oscillating field tilt both spin 1 and spin 2, however for a weak

amplitude only spin 1 are excited unless $\omega_1 = \omega_2$ (spin 1 and spin 2 are chemically

equivalent). The former is known as a hard pulse and the latter is a soft or selective pulse.

The density matrix of the 2-spin system after the 90_x° pulse is

$$\hat{\rho}_1 = \frac{\hat{E}}{4} - \frac{1}{2} \left(\tanh\left(\frac{\omega_1}{2k_B T}\right) \hat{S}_{1y} + \tanh\left(\frac{\omega_2}{2k_B T}\right) \hat{S}_{2y} \right) \quad (\text{for } \gamma_1 = \gamma_2)$$

or

$$\hat{\rho}_1 = \frac{\hat{E}}{4} + \frac{1}{2} \left(-\tanh\left(\frac{\omega_1}{2k_B T}\right) \hat{S}_{1y} + \tanh\left(\frac{\omega_2}{2k_B T}\right) \hat{S}_{2z} \right) \quad (\text{for } \gamma_1 \neq \gamma_2).$$
(2.26)

The identity matrix \hat{E} stays unchanged under any evolution, and \hat{S}_z commutes with the Hamiltonian of the system (Eq. (2.21)), thus does not change either. The only thing needed to take into account is how \hat{S}_y evolves. By submitting both the free precession Hamiltonian (2.21) and \hat{S}_{1y} into Eq. (2.18), we have

$$\begin{aligned} \hat{S}_{1y} \rightarrow & \cos(\pi J_{12} t) \sin(\omega_1 t) \hat{S}_{1x} + \sin(\pi J_{12} t) \sin(\omega_1 t) 2\hat{S}_{1y} \hat{S}_{2z} \\ & - \cos(\pi J_{12} t) \cos(\omega_1 t) \hat{S}_{1y} + \sin(\pi J_{12} t) \cos(\omega_1 t) 2\hat{S}_{1x} \hat{S}_{2z}, \end{aligned} \quad (2.27)$$

where only the \hat{S}_{1x} and \hat{S}_{1y} terms are observable by the magnetometer. The precessing transverse magnetization induces a signal voltage in an RF coil which can be digitized, stored, and displayed in a computer. In modern NMR spectrometer a Helmholtz coil is used to both provide and receive RF magnetic fields (Fig. 2.3). The NMR signal is usually represented as a complex number with the real part being proportional to the x-magnetization and the imaginary part being proportional to the y-magnetization. Therefore, the signal for spin 1 at time t is

$$\text{signal}(t) \propto \frac{i}{2} \left(e^{-i(\omega_1 + \pi J_{12})t} + e^{-i(\omega_1 - \pi J_{12})t} \right). \quad (2.28)$$

The tilted magnetization of spin 1 then precesses about the external field at the center frequency ω_1 but with a doublet splitting of $2\pi J_{12}$. If spin 2 is the same species with spin

1 and excited as well, similarly its rotation frequency is centered at ω_2 with the exact same splitting.

However, the precession of bulk magnetization is not permanent. According to thermodynamics, in the absence of other forces, a system will tend spontaneously to both an arrangement with maximum entropy and an equilibrium with minimum energy^{31, 32}. The time that the magnetic moments take to lose their synchronization (attain maximum entropy) in the horizontal direction is transverse relaxation time noted as T_2 . Even identical nuclei do not always experience the same magnetic field. Due to the fact that the nearby oscillating magnetic or electric fields that come from each nucleus and electron interfere with the applied magnetic field, some nuclei experience a slightly augmented magnetic field and precess faster while others experience a slightly diminished one and precess slower. Consequently, the magnetic moments of the identical nuclei will be dephased, and macroscopically, the transverse magnetization is zero. The revised signal expression of Eq (2.28) is

$$\text{signal}(t) \propto \frac{i}{2} \left(e^{-i(\omega_1 + \pi J_{12})t} + e^{-i(\omega_1 - \pi J_{12})t} \right) e^{-t/T_2}. \quad (2.29)$$

Therefore, what is detected is a damped oscillating electric signal which is named Free Induction Decay (FID) (Fig. 2.3). A Fourier Transform (FT) of the FID³³ gives this electric oscillation frequency, namely the nuclear Larmor Frequency.

The time that all the magnetic moments take to return back to their equilibrium (minimum energy) is longitudinal relaxation time noted as T_1 . The main mechanism for T_1 involves a direct dipole-dipole interaction. Imagine a target nuclear spin and an

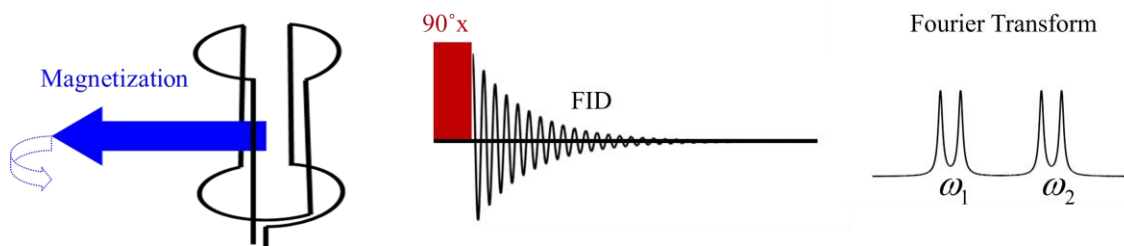


Figure 2.3: The basic $90^\circ x$ pulse-acquire NMR experiment.

adjacent spin undergoing constant rotational and translational motions. The local magnetic fields induced by their magnetic moments oscillate at the same frequency as their motion. If the oscillation frequency of one spin is comparable to the Larmor frequency of the other spin, spin flip occurs, and energy transfers between these two magnetic moments. This energy exchange keeps going at a rate governed by T_1 until equilibrium is reestablished.

2.2 The Application of NMR

The discovery of the chemical shift and J-coupling concept illuminated the direction that NMR could be used as an analytical method in interdisciplinary sciences such as chemistry, biology, and medicine. At the very beginning NMR was used to determine the structure of small molecules both organic and inorganic³⁴⁻³⁶. Biochemists realized that the same methods could also be applied to much larger biomolecules such as metabolites and to protein structure analysis³⁷⁻³⁹, especially with the development of two-dimensional NMR techniques⁴⁰⁻⁴². 2D refers to two time scales. Apart from the time scale of the acquisition stage in 1D NMR, the 2D NMR has an extra time scale of evolution. The complete stages of a 2D NMR is composed of (i) a preparation stage during which

RF pulses are applied to transfer nuclei away from the equilibrium state, (ii) an evolution stage during which the chemical shifts and/or coupling constants freely evolve, (iii) a mixing stage during which further RF pulses or delays are applied to transfer information between the nuclei, and (iv) a detection stage during which FID signal is collected. For example, 2D Correlation Spectroscopy (COSY)⁴³⁻⁴⁶ can explicitly display whether two nuclei are coupled or not with an off-diagonal data point, and J-Resolved spectroscopy (J-Res)^{41, 47-51} is able to directly show the splitting pattern of a peak caused by J-coupling, both of which are more useful than the 1D splitting peaks. NMR is also a powerful tool to investigate molecular dynamics. Intramolecular and intermolecular interactions associated with different nuclei can be linked to specific locations in the structure. Any changes of the locations could be mapped to the alter of the corresponding NMR signal. For example, diffusion ordered spectroscopy (DOSY)⁵² is used to detect the diffusion coefficient of each component in a sample, and exchange spectroscopy (EXSY)⁵³ is a tool to study the chemical shift processes in a system.

After the invention of NMR imaging known as MRI^{40, 54}, NMR application started booming in biomedicine^{55, 56}. It was discovered that 2D images and later 3D could be obtained by applying magnetic field gradients to a sample. In the presence of this gradient, the Larmor frequency is mapped to a function of position

$$\omega = -\gamma B_0 (1 - \sigma)(1 + Gr), \quad (2.30)$$

where G is the field gradient in direction r . A 2D image is constructed by repeating the measurement with gradients in different directions. NMR spectroscopy is a noninvasive technique, and compared to other radiological method like ultraviolet, X-ray, and higher

energy electromagnetic radiation, it is a nonionizing radiation and thus a safer diagnosis method⁵⁷⁻⁶⁰.

2.3 SABRE and Parahydrogen

In section 1.1 it is mentioned that the Zeeman splitting of nuclear spins is much smaller than the thermal energy. More specifically, consider protons in a 10 T magnetic field at room temperature 295K. The energy of spin-up and spin-down states are approximately $\pm \frac{\gamma_H B_0 \hbar}{2} \approx \pm 8.8 \times 10^{-7}$ eV, and the thermal energy is $k_B T \approx 2.5 \times 10^{-2}$ eV.

Using Boltzmann distribution (1.19), we can obtain the polarization of protons as

$(p_{up} - p_{down}) = \tanh\left(\frac{\gamma_H B_0 \hbar}{2k_B T}\right) \sim 10^{-5}$. The polarization of heteronuclei whose

gyromagnetic ratio is much smaller than proton is even lower. This low sensitivity is the intrinsic limitation of NMR and limits the potential application of NMR. To overcome this limitation, the concept of hyperpolarization has been conceived. The basic idea of hyperpolarization is transferring spin order from another species which is called spin source to the target nuclei. Nowadays there have developed various hyperpolarization methods, including Dynamic Nuclear Polarization (DNP)^{1, 2}, Spin-Exchange Optical Pumping (SEOP)³, ParaHydrogen-Induced Polarization (PHIP)^{4, 5}, Signal Amplification By Reversible Exchange (SABRE)⁶⁻⁹, and so on.

SABRE is the latest method which was invented in 2009 by Ralph Adams and co-workers⁶. Parahydrogen is used as the spin source in SABRE, and a proper organometallic acts as a catalyst which builds a connection between the parahydrogen

and the target molecule through chemical bounds. Both parahydrogen and target substrate rapidly and reversibly exchange with sites on the catalyst metal center. In a suitable static magnetic field, J-couplings between the hydrides and the target nuclei on the bound species transfer spin order between them, and this makes it possible to spontaneously create excess magnetization on the target nuclei.

Now, take a closer look at the spin source, parahydrogen⁶¹⁻⁶³. The two protons in the dihydrogen molecule are indistinguishable fermions, so their total state function must be antisymmetric under exchange. The Born-Oppenheimer approximation²⁴ is used to allow us to consider the motion of the electrons to be independent of those of the nuclei. The six degrees of freedom of the hydrogen molecule including the motion of electrons, the translational motion of the center of mass of the two protons, vibrational motion along the internuclear vector, rotational motion about the center of mass, nuclear interaction, and spin, are independent of each other. Consequently, the quantum state of the two protons could be written as

$$|\Psi\rangle = |\psi_e\rangle |\psi_T\rangle |\psi_V\rangle |\psi_R\rangle |\psi_N\rangle |\psi_S\rangle, \quad (2.31)$$

where T, V, R, N, and S refer to translation, vibration, rotation, nuclear interaction, and spin, respectively. $|\psi_T\rangle$, $|\psi_V\rangle$, and $|\psi_N\rangle$ are all symmetric wave functions with respect to nuclear interchange. $|\psi_R\rangle$ is a spherical harmonic function because the rotation model of the two protons is approximated to a rigid rotor. Therefore, the rotational wave function $|\psi_R\rangle$ associated with an even rotational quantum number is symmetric, while $|\psi_R\rangle$ associated with an odd rotational quantum number is antisymmetric. To make sure

that the whole quantum state $|\Psi\rangle$ is antisymmetric, either $|\psi_R\rangle$ is symmetric, and the spin state $|\psi_S\rangle$ is antisymmetric, or the opposite. A dihydrogen molecule with its two protons in symmetric spin states is called orthohydrogen and called parahydrogen with the two protons in antisymmetric spin state. The symmetric and antisymmetric spin states are

$$\begin{cases} |T_+\rangle = |\alpha\alpha\rangle \\ |T_0\rangle = \frac{1}{\sqrt{2}}(|\alpha\beta\rangle + |\beta\alpha\rangle) \\ |T_-\rangle = |\beta\beta\rangle \end{cases} \quad \text{total spin quantum number : 1} \quad (2.32)$$

$$|S_0\rangle = \frac{1}{\sqrt{2}}(|\alpha\beta\rangle - |\beta\alpha\rangle) \quad \text{total spin quantum number : 0.}$$

The state of protons on each rotational orbital with quantum number J is $(2J+1)$ -fold degenerate and has rotational energy $\frac{J(J+1)\hbar^2}{2I_m}$, where I_m is the moment of inertia of the two protons. Submitting this energy into Boltzmann distribution (2.19), we could calculate the ratio of parahydrogen to orthohydrogen as

$$p_p = \frac{\sum_{J=even} (2J+1) \exp\left(-\frac{J(J+1)\hbar^2}{2I_m k_B T}\right)}{3 \sum_{J=odd} (2J+1) \exp\left(-\frac{J(J+1)\hbar^2}{2I_m k_B T}\right)}, \quad (2.33)$$

where 3 in the denominator is because of the 3-fold degeneration of the symmetric spin states in Eq. (2.32). Figure 2.4 shows the population of both parahydrogen and orthohydrogen in equilibrium as a function of temperature. At room temperature or higher temperatures, the ratio of parahydrogen to orthohydrogen is 1:3. Around 80K, the

ratio is 1:1. At a temperature lower than 20K, the gas is almost pure parahydrogen. The density matrix of pure parahydrogen is

$$\hat{\rho}_{para} = |S_0\rangle\langle S_0| = \frac{1}{4}(\hat{E} - \hat{\sigma}_1 \cdot \hat{\sigma}_2), \quad (2.34)$$

where $\hat{\sigma}_1$ and $\hat{\sigma}_2$ are the Pauli matrices of the two protons.

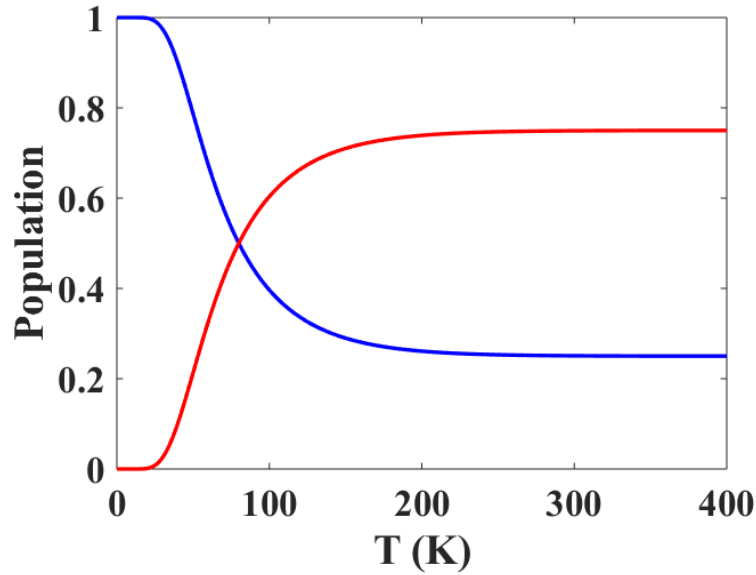


Figure 2.4: Population of parahydrogen and orthohydrogen as a function of temperature.

However, based on the selection rule mentioned before that a transition between states with different symmetry is not allowed, the transition probability between ortho and para states is zero. Therefore, even with temperature variation, the ortho-para ratio cannot change, and the system will not be at its thermal equilibrium because of the prohibited ortho-para transition. In practice, a magnetic material which generates a proximal inhomogeneous magnetic field is used as a catalyst to break the symmetry. The most common catalyst is rust. The easiest way to generate parahydrogen is flowing

thermal hydrogen through a copper coil which is filled with rust and immersed in liquid nitrogen(77K), and then around 50% parahydrogen is produced.

SABRE was first used to hyperpolarize protons in the target molecule, and the magnetic field used is close to 100 times that of the earth field (~6.5mT). Later, varieties of SABRE methods (X-SABRE)^{10, 11, 64-69} have extended the application to heteronuclei, such as ¹³C, ¹⁵N, ¹⁹F and ³¹P⁷⁰⁻⁷⁴. SABRE-SHEATH¹¹ (Signal Amplification by Reversible Exchange in Shield Enables Alignment Transfer to Heteronuclei) is the most popular variant by shielding the earth field and adjusting the added magnetic field. For example, the field used to hyperpolarize ¹⁵N is usually ~0.6μT⁷⁵. The mechanism of SABRE-SHEATH¹¹ is schematically represented in (Fig. 2.5). In a SABRE experiment, pre-activated catalyst and substrates are first dissolved in a solvent. Then a fully activated and stable SABRE sample is produced by bubbling hydrogen gas through the solution for a while. During the catalyst activation process, the cyclooctadiene moiety undergoes hydrogenation and removes from the metal complex, and the color of the catalyst gradually fades simultaneously. Finally, an octahedral molecular structure is created with the dihydride exchanging with hydrogen molecule and the transverse ligands exchanging with their free species. The spontaneous spin order transfer is only associated with the fully activated sample, so is our investigation.

The different molecules involved in the hyperpolarization process are hydrogen molecules, SABRE complex, and the target substrate, which are three different but non-independent spin systems by reason of chemical exchange. All the spin systems

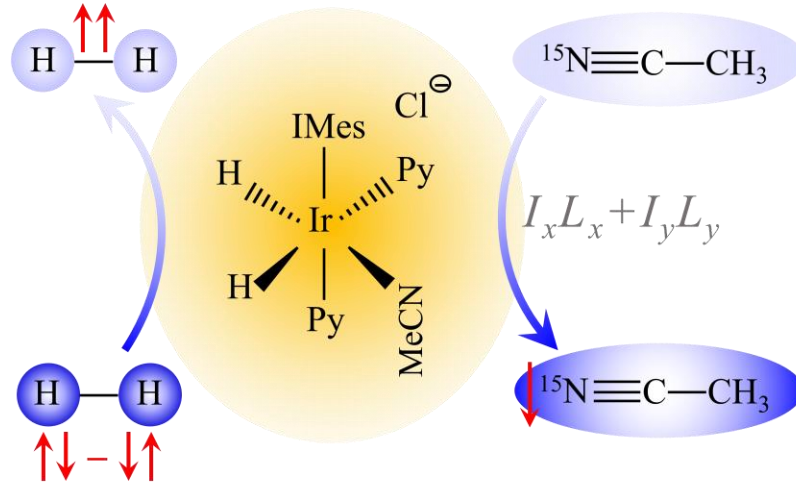


Figure 2.5: Schematical representation of generation of hyperpolarized ^{15}N labelled acetonitrile. IMes, Py and MeCN represent [1,3-bis(2,4,6-trimethylphenyl)-imidazol], pyridine ligands, and acetonitrile, respectively. Reprinted with permission from ref. 79.

experience quantum evolution, chemical exchange, and relaxation, therefore, the general master equation could be written as

$$\partial_t \begin{pmatrix} \hat{\rho}_H \\ \hat{\rho}_C \\ \hat{\rho}_S \end{pmatrix} = \begin{pmatrix} \mathcal{H}_H + \mathcal{R}_H + \mathcal{K}'_{HC} & \mathcal{K}'_{HC} & 0 \\ \mathcal{K}_{HC} & \mathcal{H}_C + \mathcal{R}_C + \mathcal{K}_{HC} + \mathcal{K}_{SC} & \mathcal{K}_{SC} \\ 0 & \mathcal{K}'_{SC} & \mathcal{H}_S + \mathcal{R}_S + \mathcal{K}'_{SC} \end{pmatrix} \begin{pmatrix} \hat{\rho}_H \\ \hat{\rho}_C \\ \hat{\rho}_S \end{pmatrix}, \quad (2.35)$$

in which \mathcal{H} , \mathcal{R} , and \mathcal{K} are the super operators of quantum evolution, relaxation, and chemical exchange, respectively, and the subscript H , C , and S indicate hydrogen molecule, activated complex, and free substrate, respectively⁷⁶. Both the quantum evolution and the relaxation of the dihydrogen system are ignored. Because the inflow and outflow of dihydrogen makes an open system, and we assume that a dissociated dihydrogen will be immediately replaced by a fresh one. The substrate molecule usually contains more than one spin, but the spins that weakly couple with the target nuclei could

be neglected. Similarly, this weak couple approximation also works for the SABRE complex system.

Take ^{15}N labelled acetonitrile as an example (Fig. 2.6), which consists of the dihydride and the target ^{15}N nucleus. The rest of the spins are neglected because of the zero or near zero couplings. The Hamiltonian of this 3-spin system in a static low magnetic field $B_0\bar{z}$ is

$$\hat{\mathcal{H}} = \omega_H (\hat{I}_{1z} + \hat{I}_{2z}) + \omega_L \hat{L}_z + 2\pi J_{HH} \hat{I}_1 \cdot \hat{I}_2 + 2\pi J_{HL} \hat{I}_1 \cdot \hat{L}, \quad (2.36)$$

where \hat{I} exclusively represents the spin operator of a proton, and L refers to the target nuclei in the substrate ligand. $\omega_H = -\gamma_H B_0$ and $\omega_L = -\gamma_L B_0$. Since the magnetic field applied is very low $\sim 0.6\mu\text{T}$, the chemical shift of the nuclei is neglected, and the secular approximation is not applicable here, i.e., $xx + yy$ in the J-coupling terms cannot be

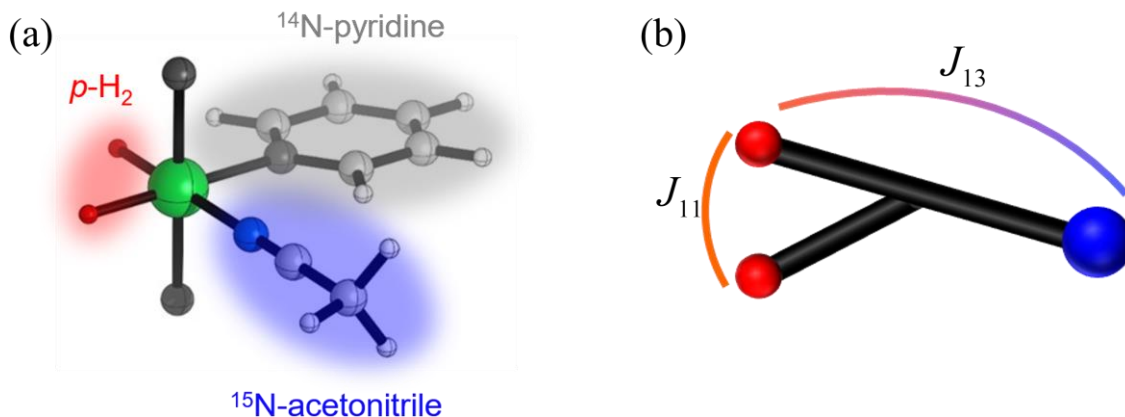


Figure 2.6: (a) Molecular diagram of the SABRE complex with acetonitrile as the substrate and pyridine as the co-ligand. (b) reduced 3-spin system of the SABRE complex

omitted. The matrix form of the Hamiltonian is

$$\begin{array}{cccccccc}
& T_H^+ \alpha_L & T_H^+ \beta_L & T_H^0 \alpha_L & S_H^0 \alpha_L & T_H^- \alpha_L & T_H^0 \beta_L & S_H^0 \beta_L & T_H^- \beta_L \\
T_H^+ \alpha_L & \frac{2\omega_H + \omega_L + \pi(J_{HH} + J_{HL})}{2} & & & & & & & \\
T_H^+ \beta_L & & \frac{2\omega_H - \omega_L + \pi(J_{HH} - J_{HL})}{2} & \frac{\pi J_{HL}}{\sqrt{2}} & \frac{-\pi J_{HL}}{\sqrt{2}} & & & & \\
T_H^0 \alpha_L & & \frac{\pi J_{HL}}{\sqrt{2}} & \frac{\omega_L + \pi J_{HH}}{2} & \frac{\pi J_{HL}}{2} & & & & \\
S_H^0 \alpha_L & & \frac{-\pi J_{HL}}{\sqrt{2}} & \frac{\pi J_{HL}}{2} & \frac{\omega_L - 3\pi J_{HH}}{2} & & & & \\
T_H^- \alpha_L & & & & & \frac{-2\omega_H + \omega_L + \pi(J_{HH} - J_{HL})}{2} & \frac{\pi J_{HL}}{\sqrt{2}} & \frac{\pi J_{HL}}{\sqrt{2}} & \\
T_H^0 \beta_L & & & & & \frac{\pi J_{HL}}{\sqrt{2}} & \frac{-\omega_L + \pi J_{HH}}{2} & \frac{-\pi J_{HL}}{2} & \\
S_H^0 \beta_L & & & & & \frac{\pi J_{HL}}{\sqrt{2}} & \frac{-\pi J_{HL}}{2} & \frac{-\omega_L - 3\pi J_{HH}}{2} & \\
T_H^- \beta_L & & & & & & & & \frac{-2\omega_H - \omega_L + \pi(J_{HH} + J_{HL})}{2}
\end{array} \quad (2.37)$$

Each empty spot in the matrix means number zero. The basis used here is the singlet-triplet states $(T_H^+, T_H^0, T_H^-, S_H^0)$ of the two protons times the spin-up (α) and spin-down (β) of the target nucleus. The whole Hamiltonian is block diagonalized into two one-dimensional and two 3×3 submatrices. The one-dimensional submatrices have no physical significance and will be omitted in all the following content. A close look at the two 3×3 subspaces reveals that they are not the same even though very similar. The off-diagonal terms have a slight phase difference which is not important. The difference between their diagonal elements is the key point which breaks the balance between states $|\alpha_L\rangle$ and $|\beta_L\rangle$, and thus generate polarization of the target nuclei. Assume the system is initially composed of parahydrogen and thermally balanced target nuclei, then the initial state could be expressed as $\hat{\rho}_0 = \frac{1}{2} |S_H^0 \alpha_L\rangle \langle S_H^0 \alpha_L| + \frac{1}{2} |S_H^0 \beta_L\rangle \langle S_H^0 \beta_L|$. The two terms of $\hat{\rho}_0$ evolve under the management of the first and second 3×3 submatrices, respectively. Figure 2.7 shows how the population of the target nuclei's spin-up α_L and spin-down β_L

states evolve with time in each subspace and the total polarization as a function of time. In the absence of a magnetic field, the two submatrices are the same, and the fluctuations of the α_L and β_L states in one subspace cancel out the other. However, with an appropriate magnetic field ($-0.5\mu\text{T}$ is used in the simulation) the spin-up and down population oscillations are no longer the same, and the polarization is created. It is

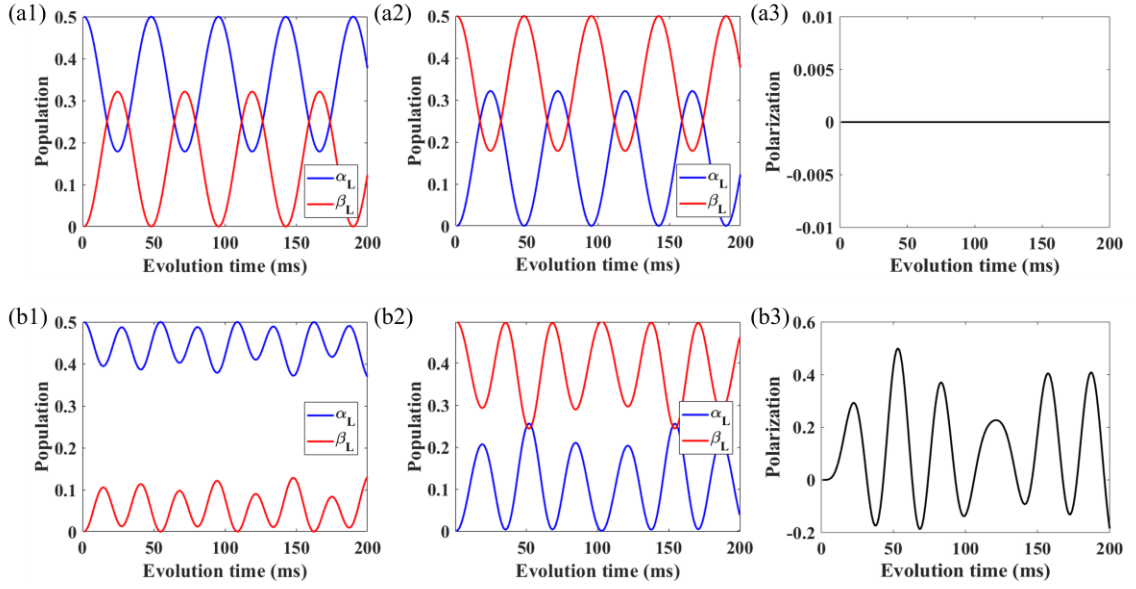


Figure 2.7: (a) In the case of no external magnetic field, the population of both the spin-up α_L (blue) and spin-down β_L (red) states in subspace #1 (a1) and subspace #2 (a2) (shown in Eq. 2.37) as a function of time, and how the polarization vary with time (a3). More specifically, in the first 3×3 subspace the populations of state $T_H^0 \alpha_L$ and $S_H^0 \alpha_L$ are summed up to yield the total population of α_L , and similarly, in the second 3×3 subspace the populations of state $T_H^0 \beta_L$ and $S_H^0 \beta_L$ are summed up to generate the total population of β_L (b) A counterpart of (a) in the case of a proper magnetic field.

obvious that when the added magnetic field is so large that $|\omega_H - \omega_L| \gg |J_{HL}|$, the off-diagonal element in the first row and column of both the submatrices in Eq. (2.36) are negligible based on Secular Approximation. Consequently, the spin-up and down states

of the target nuclei are mutually independent, and there is no longer any population transfer between them. With only the quantum evolution being considered, the density matrix of the SABRE complex evolves in terms of the Liouville-von Neumann Eq. (2.17)

$$\partial_t \hat{\rho}_C = \mathcal{H}_C \hat{\rho}_C = -i \left[\hat{\mathcal{H}}, \hat{\rho}_C \right]. \quad (2.38)$$

Spin relaxation must be taken into account since hyperpolarized spin are always returning back to equilibrium. The two dominant relaxation process – losing synchronization (T_2) and losing energy (T_1) could be mathematically expressed as

$$\partial_t \hat{\rho} = \sum_i^{spin} \left[\frac{Diag(\hat{\rho}_i) - \hat{\rho}}{T_{2,i}} + \frac{\hat{\rho}_i^{equ} - Diag(\hat{\rho})}{T_{1,i}} \right]. \quad (2.39)$$

$Diag(\hat{\rho}_i)$ and $Diag(\hat{\rho})$ in the above equation are reduced matrix of $\hat{\rho}_i$ and $\hat{\rho}$ with all the diagonal elements staying unchanged while all the off-diagonal elements vanishing. $Diag(\hat{\rho}_i)$ is fully out of phase but have the same energy with $\hat{\rho}_i$. $\hat{\rho}_i^{equ}$ is the equilibrium state of spin i. $T_{1,i}$ and $T_{2,i}$ are the respective longitudinal and transversal relaxation time of spin i. In the case of small molecules, T_1 and T_2 are approximately equal. Therefore,

Eq. (2.39) can be further simplified into $\partial_t \hat{\rho} = \sum_i^{spin} \frac{\hat{\rho}_i^{equ} - \hat{\rho}}{T_{1,i}}$.

The quantum process explained why spin order could be transferred back and forth between the dihydride and the target nuclei. However, to accumulate polarization chemical exchange is crucial. Both dihydrogen and substrates have two existent forms, freely tumbling in the sample solution as an independent molecule or binding to the catalyst center. The two forms are exchangeable at an average frequency known as

exchange rate and denoted with k_H and k_L , respectively. This chemical exchange rate depends on many different factors, such as concentration of the component, temperature of the sample, chemical-bond energy, and so on. Each time an exchange happens, the quantum evolution process is interrupted, and the bound species dissociates and takes away its spin state information (mathematically manipulated using reduced density matrix), while a free species takes up the empty spot and integrates its spin state information into the spin system (mathematically manipulated using tensor product). More specifically, in the situation that one of the bound ligand exchanges with its free species, the new density matrix of the SABRE complex becomes $Tr_{\{H\}}(\hat{\rho}_C) \otimes \hat{\rho}_S$ where $Tr_{\{ \}}()$ is a reduce density matrix with the remaining spins displayed in the curly brackets, and the density matrix of the dissociated target spin is $Tr_{\{L\}}(\hat{\rho}_C)$. However, in the situation that the dihydride exchange with dihydrogen, the new density matrix of the SABRE complex is $\hat{\rho}_{paraH_2} \otimes \hat{\rho}_S$, which mean both a new parahydrogen and a new substrate molecule associate to the catalyst center. This is because the complex which is only composed of substrate ligands without dihydride is not a possible configuration. In other words, each exchange of the dihydride is accompanied by the exchange of the transverse substrates. Consequently, the density matrix evolution of the SABRE complex and the free substrate caused by chemical exchange are expressed as

$$\begin{aligned} \partial_t \hat{\rho}_C &= \mathcal{K}_{HC}(\hat{\rho}_H, \hat{\rho}_C) + \mathcal{K}_{SC}(\hat{\rho}_S, \hat{\rho}_C) \\ &= (k_L - k_H) Tr_{\{H\}}(\hat{\rho}_C) \otimes \hat{\rho}_S + k_H \hat{\rho}_{paraH_2} \otimes \hat{\rho}_S - k_L \hat{\rho}_C, \end{aligned} \quad (2.40)$$

and

$$\partial_t \hat{\rho}_S = \mathcal{K}'_{SC}(\hat{\rho}_S, \hat{\rho}_C) = \frac{[C]}{[S]} k_L \left(\text{Tr}_{\{L\}}(\hat{\rho}_C) - \hat{\rho}_S \right), \quad (2.41)$$

where the exchange operators \mathcal{K}_{HC} , \mathcal{K}_{SC} , and \mathcal{K}'_{SC} are prementioned in Eq (2.35); $[C]$ and $[S]$ are the concentration of the SABRE complex and the concentration of the free substrate, respectively. This is the traditional way to treat the exchange process. It is obvious that quantum evolution \mathcal{H} , spin relaxation \mathcal{R} , and chemical exchange \mathcal{K} do not commute with each other. Therefore, to reliably execute the evolution of the density matrix the time step must be very short. A recent work released this limitation of small step size by solving the exact form of chemical exchange in dynamic quantum systems using infinite-order perturbation theory¹³. Surprisingly, the modification of chemical exchange converges to a simple exponential form

$$\tilde{k} \equiv k \exp\left(-\frac{k\Delta t}{2}\right), \quad (2.42)$$

where \tilde{k} and k are the modified and pre-modified exchange rate, respectively, and Δt is the evolution time step. By replace k_H and k_L in Eq. (2.40) and (2.41) with $\tilde{k}_H \equiv k_H \exp\left(-\frac{k_H\Delta t}{2}\right)$ and $\tilde{k}_L \equiv k_L \exp\left(-\frac{k_L\Delta t}{2}\right)$, we obtain the modified chemical exchange operation.

Now we could easily expand the chemical exchange operator to a symmetric 4-spin AA'BB' system. Figure 2.8 gives a typical example of this spin system – dihydride and two pyridine binding to the catalyst center. Similar with Eq. (2.40) and (2.41), the

corresponding differential equation of motion of both the SABRE complex density matrix and free substrate density matrix in terms of chemical exchange are

$$\begin{aligned} \partial_t \hat{\rho}_C = & \frac{(\tilde{k}_L - \tilde{k}_H)}{2} \left(\text{Tr}_{\{HL_1\}}(\hat{\rho}_C) \otimes \hat{\rho}_S + \mathcal{U}_{L_1 \leftrightarrow L_2}^{-1} \left(\text{Tr}_{\{HL_2\}}(\hat{\rho}_C) \otimes \hat{\rho}_S \right) \mathcal{U}_{L_1 \leftrightarrow L_2} \right) \\ & + \tilde{k}_H \hat{\rho}_{paraH_2} \otimes \hat{\rho}_S \otimes \hat{\rho}_S - \tilde{k}_L \hat{\rho}_C, \end{aligned} \quad (2.43)$$

and

$$\partial_t \hat{\rho}_S = \frac{[C]}{[S]} \tilde{k}_L \left(\frac{\text{Tr}_{\{L_1\}}(\hat{\rho}_C) + \text{Tr}_{\{L_2\}}(\hat{\rho}_C)}{2} - \hat{\rho}_S \right). \quad (2.44)$$

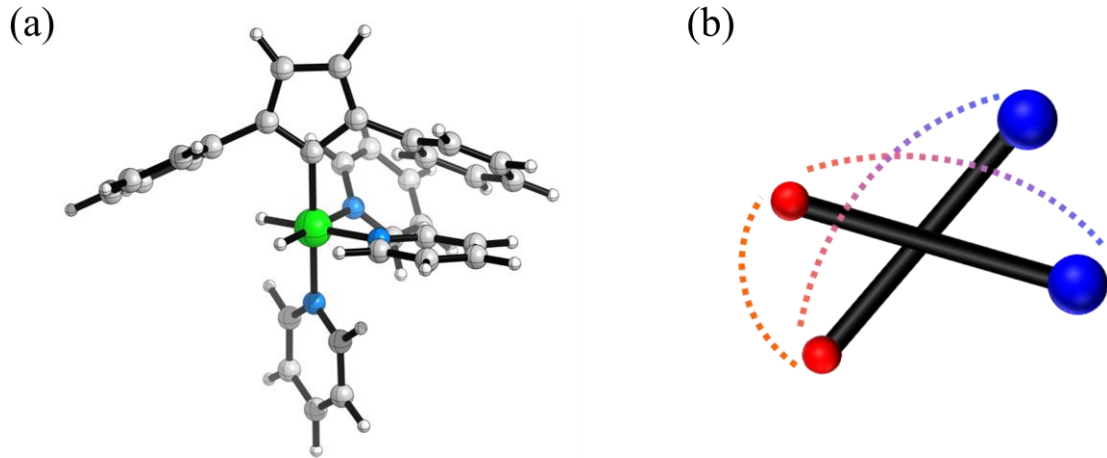


Figure 2.8: (a) Molecular diagram of the AA'BB' SABRE complex with pyridine as the substrate (b) reduced spin system of the SABRE complex.

Combining all these dynamics together, we have the exact Dissipative Master Equation (DMEx), which is extremely powerful for numerically simulating the evolution of spin systems. Figure 1.9 displays how the hyperpolarization of the target nuclei is built up with time. As time goes by more and more free substrates have contacted with the parahydrogen and been hyperpolarized, and in the meantime, they keep losing

polarization as well. Consequently, the total polarization of the target spin ensemble reaches a new level of balance. The red curve simulates an ideal evolution without any

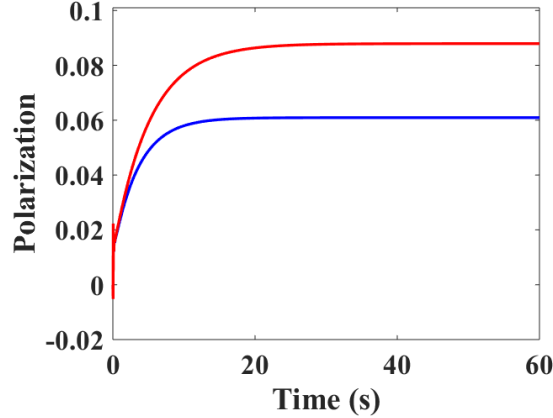


Figure 2.9: Polarization of the target nuclei as a function of time. Red curve refers to the ideal case without relaxation, while blue curve takes relaxation into account. An AA'B spin system and 100% parahydrogen are used in the numerical simulation, and the specific parameters are $B_0 = -0.5\mu T$, $J_{HH} = -8Hz$, $J_{HL} = -24Hz$, $k_L = 20s^{-1}$,

$$k_H = 2s^{-1}, \text{ and } \frac{[C]}{[S]} = \frac{1}{10}.$$

spin relaxation, while the blue curve refers to a situation with $T_{1L,free} = 30s$, $T_{1L,bound} = 3s$, and $T_{1H,bound} = 1s$. We can also figure out the optimal low field ($\sim \pm 0.6\mu T$) applied to the 3-spin system by sweeping the magnitude of B_0 (Fig. 2.10).

SABRE enjoys a lot of advantages. Its polarization process is easy since both the chemical exchanges and spin order transfer are spontaneous, and the maximum polarization is achieved quickly, which is usually 30 – 60s (displayed in (Fig. 2.9)) and much shorter than other techniques like DNP and SEOP (generally, several hours are needed). What's more, SABRE is a cost-effective method, because all the materials and

the low magnetic field are easily available and low-cost. However, SABRE has not become a perfect hyperpolarization method. One major reason is that the hyperpolarization yielded by SABRE is not very high – the optimized polarization is 63% for ^1H , 25% for ^{13}C , and 43% for ^{15}N , which are not close to 100%, especially for heteronuclei. Therefore, improvement of SABRE is highly necessary.

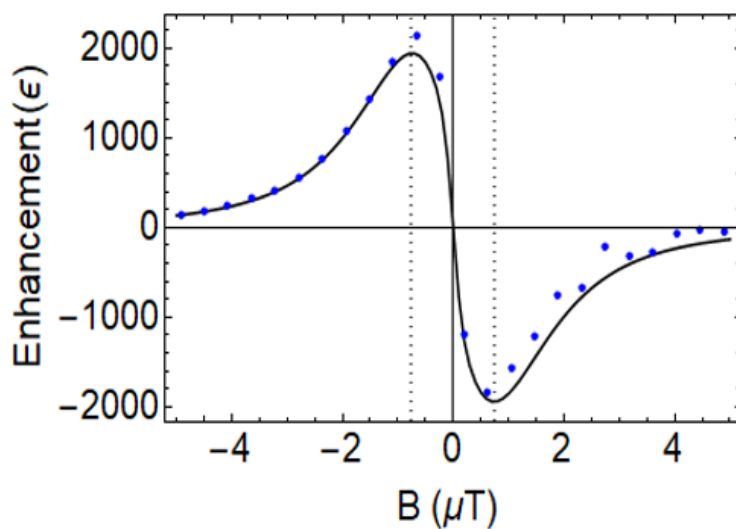


Figure 2.10: Magnetic field profile of a AA'B spin system, which shows both experiment (dots) and simulation (curve) results. Image courtesy of S. Eriksson, et al., *Sci. Adv.* 8, 11, (2022).

Chapter 3: Oscillating Pulse Sequence SABRE

The traditional SABRE-SHEATH method is limited in its ability to produce high levels of polarization. A big part of the reason is that the novel field regime for SABRE and X-SABRE (where even heteronuclear couplings can be readily interconverted between the strong and weak coupling limits), combined with the very complex exchange dynamics, imply that the method is theoretically underexplored; there are clearly better (but nonintuitive) approaches to creating polarization than a simple continuous field. Specifically, ref. 76 shows that an alternating two-field pulse sequence (both fields high, but with a small average) can produce very large SABRE enhancements. Therefore, novel techniques are required to achieve a breakthrough⁷⁷⁻⁷⁹. Here we more systematically explore the use of the periodic field perturbations, with the goal of creating enhanced magnetization with low sensitivity to experimental imperfections such as field inhomogeneity¹². In particular, we have studied four pulse sequences: square pulse, sine wave pulse, chirped pulse, and ramp pulse, as illustrated in Fig. 3.1. These investigations hold promise for the development of improved magnetic resonance techniques. Each pulse sequence consists of a low offset field ($< 1\mu T$) and an oscillating pulse with interleaving positive and negative amplitude ($10-100\mu T$). Every pulse is specified by three parameters – the constant offset field B_0 , the oscillating field $B(t)$, and the pulse period T . A simulation with DMEx¹³ verifies the efficiency of square pulse (Fig. 3.2). A 3-spin system (shown in Fig. 2.6) undergoes a square pulse whose pulse amplitude is fixed at $10\mu T$. The ultimate polarization of the target nuclei is plotted as a function of

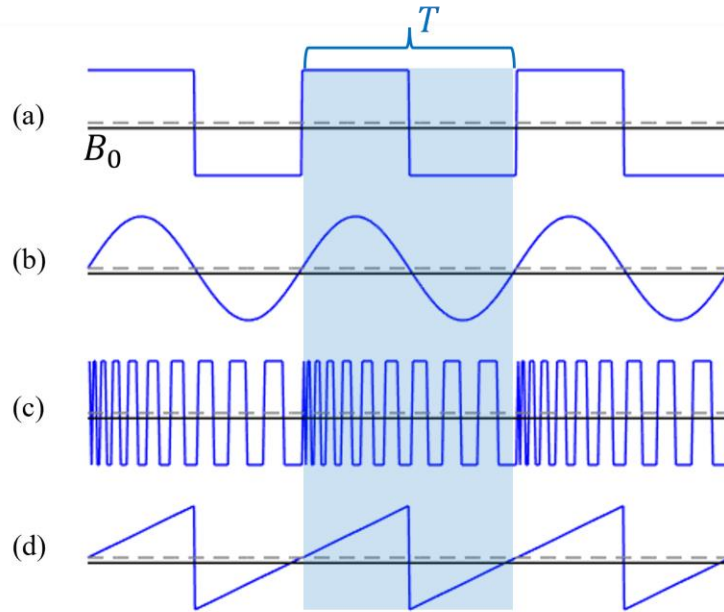


Figure 3.1: Pulse sequences for enhanced SABRE excitation. (a) square pulse, (b) sine wave pulse, (c) chirped pulse, and (d) ramp pulse. The dashed grey line refers to zero magnetic field, and the black line is an offset field, $B_0 \bar{z}$. Reprinted with permission from ref. 79.

both the offset field B_0 and the pulse period T . If the pulse oscillates extremely fast ($T \approx 0$), it does not make any difference to the spins, and the whole system recovers to a CW situation (the very left column of the 3D plot in Figure 3.2). The maximal polarization ($\sim 5\%$) is generated with a continuous $\sim \pm 0.5 \mu T$ field (shown in Fig. 2.10). However, a far larger polarization ($\sim 18\%$) is produced by a correctly timed square wave offset from a zero average field by about one-fourth that value ($\sim \pm 0.13 \mu T$). Apart from numerical verification, a theoretical understanding of the improved performance of the pulse sequences is very helpful.

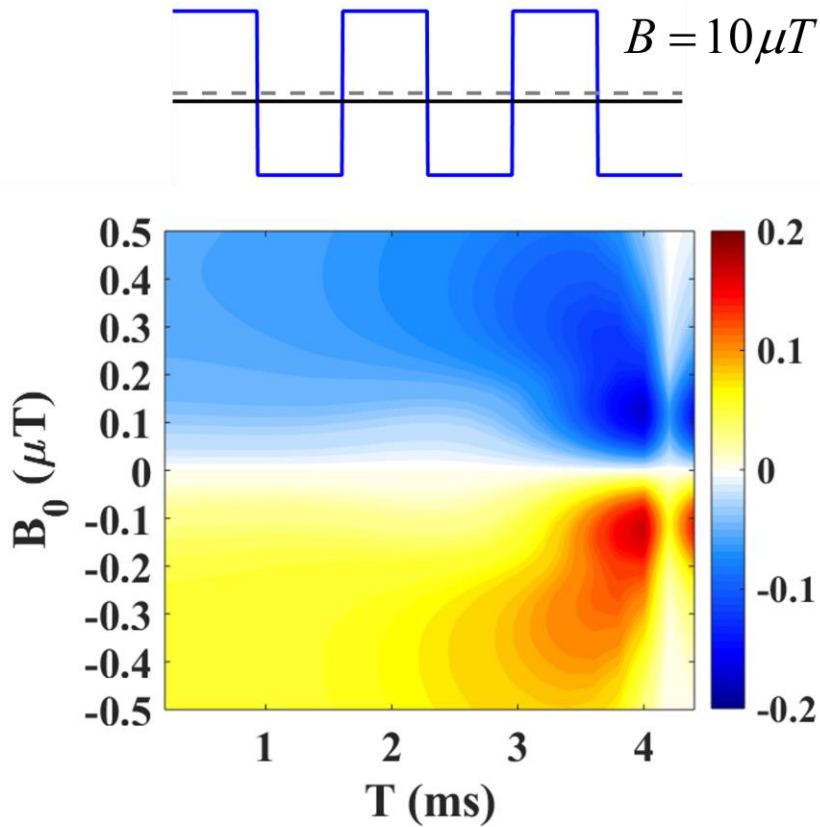


Figure 3.2: Schematic representation of the unbalanced square pulse and the final polarization level simulated with DMEx. The coupling strength between the two hydrides is $J_{HH} = -8\text{Hz}$, and the coupling between the hydride and the target nuclei is $J_{HL} = -25\text{Hz}$. The offset field B_0 is varied from $-0.5\mu\text{T}$ to $0.5\mu\text{T}$, and the pulse period T is scanned in the range of 0 to 4.4ms , while the pulse amplitude B is fixed at $10\mu\text{T}$. Simulation parameters: 100% parahydrogen, $k_L = 24\text{s}^{-1}$, $k_H = 8\text{s}^{-1}$, $\frac{[C]}{[S]} = \frac{1}{10}$. A pulse with $B_0 = \pm 0.13\mu\text{T}$ and $T = 4\text{ms}$ yields the maximal polarization ($\sim 18\%$), which is much larger than the continuous wave counterpart ($\sim 5\%$). Reprinted with permission from ref. 79.

3.1 Theoretical Perspective of Pulse Sequence

3.1.1 Hamiltonian in the Interaction Frame

For the sake of comprehensiveness, we analyze both AA'B 3-spin system and AA'BB' 4-spin system. The full Hamiltonian of the three-spin AA'B system is expressed as:

$$\hat{\mathcal{H}}_{prime}(t) = -(B_0 + B(t))(\gamma_H(\hat{I}_{1z} + \hat{I}_{2z}) + \gamma_L\hat{L}_z) + 2\pi J_{HH}(\hat{I}_1 \cdot \hat{I}_2) + 2\pi J_{HL}(\hat{I}_1 \cdot \hat{L}) \quad (3.1)$$

The Hamiltonian could be rearranged as:

$$\begin{aligned} \hat{\mathcal{H}}_{rearranged}(t) = & -(B_0 + B(t))\gamma_H(\hat{I}_{1z} + \hat{I}_{2z} + \hat{L}_z) + (\Delta\omega_0 + \Delta\omega(t))\hat{L}_z \\ & + 2\pi J_{HH}(\hat{I}_1 \cdot \hat{I}_2) + 2\pi J_{HL}(\hat{I}_1 \cdot \hat{L}), \end{aligned} \quad (3.2)$$

in which $\Delta\omega_0 = B_0(\gamma_H - \gamma_L)$ and $\Delta\omega(t) = B(t)(\gamma_H - \gamma_L)$ are the Larmor frequency difference between hydrides and the target nuclei caused by the offset field and the oscillating pulse, respectively. The first term in the rearranged Hamiltonian which is directly proportional to the z component of the total spin angular momentum can be ignored since it commutes with the rest of the Hamiltonian, giving a simplified Hamiltonian of the form

$$\hat{\mathcal{H}}(t) = (\Delta\omega_0 + \Delta\omega(t))\hat{L}_z + 2\pi J_{HH}(\hat{I}_1 \cdot \hat{I}_2) + 2\pi J_{HL}(\hat{I}_1 \cdot \hat{L}), \quad (3.3)$$

which is not trivially time dependent. According to Eq. (2.11), we know that an interaction picture transformation could simplify the Hamiltonian or even remove the time-dependence. Here, we use the only time-dependent term $\Delta\omega\hat{L}_z$ to create a rotating operator

$$\hat{U}(t) = \exp(-i\hat{L}_z \int_0^t \Delta\omega(t') dt'). \quad (3.4)$$

The corresponding Hamiltonian in the interaction frame is

$$\begin{aligned} \tilde{\mathcal{H}}(t) &= \hat{U} \left\{ \Delta\omega_0 \hat{L}_z + 2\pi J_{HH} \left(\hat{I}_1 \cdot \hat{I}_2 \right) + 2\pi J_{HL} \left(\hat{I}_1 \cdot \hat{L} \right) \right\} \hat{U}^\dagger \\ &= \Delta\omega_0 \hat{L}_z + 2\pi J_{HH} \left(\hat{I}_1 \cdot \hat{I}_2 \right) \\ &\quad + 2\pi J_{HL} \left\{ \hat{I}_{1z} \hat{L}_z + M(t) \left(\hat{I}_{1x} \hat{L}_x + \hat{I}_{1y} \hat{L}_y \right) + N(t) \left(\hat{I}_{1x} \hat{L}_y - \hat{I}_{1y} \hat{L}_x \right) \right\} \end{aligned} \quad (3.5)$$

in which

$$\begin{aligned} M(t) &= \cos \left(\int_0^t \Delta\omega(t') dt' \right) \\ N(t) &= \sin \left(\int_0^t \Delta\omega(t') dt' \right). \end{aligned} \quad (3.6)$$

The time-dependent information has been passed on from a Zeeman term to the J-coupling between the hydride and the target nuclei. The original J-coupling term, $\hat{I}_{1x} \hat{L}_x + \hat{I}_{1y} \hat{L}_y$, and the new interaction form, $\hat{I}_{1x} \hat{L}_y - \hat{I}_{1y} \hat{L}_x$, are tuned by the factor $M(t)$ and $N(t)$, respectively. Replacing the spin operators in the x and y directions with the raising and lowering operator, $\hat{I}_+ = \hat{I}_x - i\hat{I}_y$ and $\hat{I}_- = \hat{I}_x + i\hat{I}_y$ we could rewrite the Hamiltonian as

$$\begin{aligned} \tilde{\mathcal{H}}(t) &= \Delta\omega_0 \hat{L}_z + 2\pi J_{HH} \left(\hat{I}_1 \cdot \hat{I}_2 \right) \\ &\quad + 2\pi J_{HL} \left\{ \hat{I}_{1z} \hat{L}_z + \frac{M(t) - iN(t)}{2} \hat{I}_{1+} \hat{L}_- + \frac{M(t) + iN(t)}{2} \hat{I}_{1-} \hat{L}_+ \right\}. \end{aligned} \quad (3.7)$$

When the oscillating pulse vanishes, the system recovers to the CW SABRE-SHEATH with $M = 1$ and $N = 0$, and the flip-flop terms $\hat{I}_{1+} \hat{L}_-$ and $\hat{I}_{1-} \hat{L}_+$ have fixed coefficient $\frac{1}{2}$.

It is worth noting that the change of the J-coupling is only caused by frame transformation and has nothing to do with the pulse sequence, which means it is a generic result. The offset term survives because it commutes with the rotation operator \hat{U} , and the role of it is to provide a small external magnetic field to the system, which works the same as the continues wave used in the ordinary SABRE-SHEATH.

A similar calculation could be executed to the AA'BB' system. The original full Hamiltonian of the 4-spin system experiencing an extra oscillating pulse is

$$\begin{aligned} \hat{\mathcal{H}}(t) = & -(B_0 + B(t))\gamma_H (\hat{I}_{1z} + \hat{I}_{2z} + \hat{L}_{1z} + \hat{L}_{2z}) + (\Delta\omega_0 + \Delta\omega(t))(\hat{L}_{1z} + \hat{L}_{2z}) \\ & + 2\pi \left\{ J_{HH} (\hat{I}_1 \cdot \hat{I}_2) + J_{HL} (\hat{I}_1 \cdot \hat{L}_1 + \hat{I}_2 \cdot \hat{L}_2) \right\}. \end{aligned} \quad (3.8)$$

Simplifying the Hamiltonian by taking out the first term which commutes with the rest of the Hamiltonian gives

$$\hat{\mathcal{H}}(t) = (\Delta\omega_0 + \Delta\omega(t))(\hat{L}_{1z} + \hat{L}_{2z}) + 2\pi \left\{ J_{HH} (\hat{I}_1 \cdot \hat{I}_2) + J_{HL} (\hat{I}_1 \cdot \hat{L}_1 + \hat{I}_2 \cdot \hat{L}_2) \right\}. \quad (3.9)$$

Then transfer this Hamiltonian to the toggling frame

$$\hat{U}(t) = \exp(-i(\hat{L}_{1z} + \hat{L}_{2z}) \int_0^t \Delta\omega(t') dt'). \quad (3.10)$$

The corresponding Hamiltonian is expressed as

$$\begin{aligned} \tilde{\mathcal{H}}(t) = & \hat{U} \left\{ (\Delta\omega_0 + \Delta\omega(t))(\hat{L}_{1z} + \hat{L}_{2z}) + 2\pi \left\{ J_{HH} (\hat{I}_1 \cdot \hat{I}_2) + J_{HL} (\hat{I}_1 \cdot \hat{L}_1 + \hat{I}_2 \cdot \hat{L}_2) \right\} \right\} \hat{U}^\dagger \\ = & \Delta\omega_0 (\hat{L}_{1z} + \hat{L}_{2z}) + 2\pi J_{HH} (\hat{I}_1 \cdot \hat{I}_2) \\ & + 2\pi J_{HL} \left\{ \hat{I}_{1z} \hat{L}_{1z} + M(t) (\hat{I}_{1x} \hat{L}_{1x} + \hat{I}_{1y} \hat{L}_{1y}) + N(t) (\hat{I}_{1x} \hat{L}_{1y} - \hat{I}_{1y} \hat{L}_{1x}) \right\} \\ & + 2\pi J_{HL} \left\{ \hat{I}_{2z} \hat{L}_{2z} + M(t) (\hat{I}_{2x} \hat{L}_{2x} + \hat{I}_{2y} \hat{L}_{2y}) + N(t) (\hat{I}_{2x} \hat{L}_{2y} - \hat{I}_{2y} \hat{L}_{2x}) \right\}, \end{aligned} \quad (3.11)$$

in which $M(t)$ and $N(t)$ are the same with the 3-spin case Eq. (3.6). Since there are two target nuclei in every SABRE complex, and each one couples with one of the two hydrides, these two couplings are adjusted identically by the oscillation pulse.

3.1.2 Average Hamiltonian

It seems that the Hamiltonian is not simplified at all, but the physics is much clearer by transferring the time dependent information to the J-coupling, and another bonus of this frame transformation is that the average Hamiltonian converges way faster in the rotation frame. Analyzing a time-varying Hamiltonian is usually very difficult, therefore the average Hamiltonian tool⁸⁰⁻⁸² is applied here to get rid of the time dependence. The general principle of the average Hamiltonian is that under suitable conditions, a time-dependent Hamiltonian can be replaced with the time-independent effective Hamiltonian over a time period. The evolution of a spin system driven by a time-dependent external field can be described by the average effect of the field over one cycle of its oscillation.

$$\hat{U}(t) = \exp\left(-i\mathcal{D}\int_0^T \tilde{\mathcal{H}}(t) dt\right) = \exp(-i\bar{\mathcal{H}}T), \quad (3.12)$$

where \mathcal{D} is the Dyson time order operator. Usually, it is impossible to analytically calculate the propagator of a non-trivial time-dependent Hamiltonian. Therefore, Eq. (3.12) is for numerical purposes only. The analytical solution of the average Hamiltonian is expanded in a series expansion, known as the Magnus expansion

$$\bar{\mathcal{H}} = \bar{\mathcal{H}}^{(0)} + \bar{\mathcal{H}}^{(1)} + \bar{\mathcal{H}}^{(2)} + \bar{\mathcal{H}}^{(3)} + \dots \quad (3.13)$$

The first three orders of the Magnus expansion are given by

$$\bar{\mathcal{H}}^{(0)} = \frac{1}{T} \int_0^T \tilde{\mathcal{H}}(t) dt \quad (3.14)$$

$$\bar{\mathcal{H}}^{(1)} = \frac{1}{2iT} \int_0^T dt_1 \int_0^{t_1} dt_2 [\tilde{\mathcal{H}}(t_1), \tilde{\mathcal{H}}(t_2)] \quad (3.15)$$

$$\bar{\mathcal{H}}^{(2)} = \frac{-1}{6T} \int_0^T dt_1 \int_0^{t_1} dt_2 \int_0^{t_2} dt_3 \left\{ [\tilde{\mathcal{H}}(t_1), [\tilde{\mathcal{H}}(t_2), \tilde{\mathcal{H}}(t_3)]] + [[\tilde{\mathcal{H}}(t_1), \tilde{\mathcal{H}}(t_2)], \tilde{\mathcal{H}}(t_3)] \right\}. \quad (3.16)$$

If the Magnus expansion converges fast enough, a good approximation of the Hamiltonian could be made by truncating at the first few orders.

We focus on the AA'B system during the whole average Hamiltonian analysis.

The generic expression of the zero-order average Hamiltonian of the 3-spin system is

$$\begin{aligned} \bar{\mathcal{H}}^{(0)} &= \frac{1}{T} \int_0^T \tilde{\mathcal{H}}(t) dt \\ &= \Delta\omega_0 \hat{L}_z + 2\pi J_{HH} \left(\hat{I}_1 \cdot \hat{I}_2 \right) \\ &\quad + 2\pi J_{HL} \left\{ \hat{I}_{1z} \hat{L}_z + M_0 \left(\hat{I}_{1x} \hat{L}_x + \hat{I}_{1y} \hat{L}_y \right) + N_0 \left(\hat{I}_{1x} \hat{L}_y - \hat{I}_{1y} \hat{L}_x \right) \right\}. \end{aligned} \quad (3.17)$$

A matrix expression of this zero-order Hamiltonian is powerful for providing physical insight. The basis used here to express the matrix of the AA'B system is a singlet-triplet basis for the AA' pair and the Zeeman basis for the B spin. We only give the two 3×3 subspaces of the zero-order Hamiltonian, which indicate that $M_0 \pm iN_0$ alter the interaction between the spin up states α_L and spin down states β_L of the target nuclei, and that the interaction strength only depends on its magnitude, $\sqrt{M_0^2 + N_0^2}$.

$$\begin{array}{c}
T_H^+ \beta_L \\
T_H^0 \alpha_L \\
S_H^0 \alpha_L
\end{array}
\begin{pmatrix}
T_H^+ \beta_L & T_H^0 \alpha_L & S_H^0 \alpha_L \\
\frac{\pi(J_{HH} - J_{HL}) - \Delta\omega_0}{2} & \frac{\pi J_{HL}}{\sqrt{2}}(M_0 + iN_0) & \frac{-\pi J_{HL}}{\sqrt{2}}(M_0 + iN_0) \\
\frac{\pi J_{HL}}{\sqrt{2}}(M_0 - iN_0) & \frac{\pi J_{HH} + \Delta\omega_0}{2} & \frac{\pi J_{HL}}{2} \\
\frac{-\pi J_{HL}}{\sqrt{2}}(M_0 - iN_0) & \frac{\pi J_{HL}}{2} & \frac{\Delta\omega_0 - 3\pi J_{HH}}{2}
\end{pmatrix}
\begin{array}{c}
T_H^- \alpha_L \\
T_H^0 \beta_L \\
S_H^0 \beta_L
\end{array}
\begin{pmatrix}
T_H^+ \beta_L \\
T_H^0 \alpha_L \\
S_H^0 \alpha_L
\end{pmatrix}
\begin{pmatrix}
\frac{\pi(J_{HH} - J_{HL}) + \Delta\omega_0}{2} & \frac{\pi J_{HL}}{\sqrt{2}}(M_0 - iN_0) & \frac{\pi J_{HL}}{\sqrt{2}}(M_0 - iN_0) \\
\frac{\pi J_{HL}}{\sqrt{2}}(M_0 + iN_0) & \frac{\pi J_{HH} - \Delta\omega_0}{2} & \frac{-\pi J_{HL}}{2} \\
\frac{\pi J_{HL}}{\sqrt{2}}(M_0 + iN_0) & \frac{-\pi J_{HL}}{2} & \frac{-\Delta\omega_0 - 3\pi J_{HH}}{2}
\end{pmatrix}
\tag{3.18}$$

This is a generic matrix form of the zero-order expansion, and the features of each specific pulse are carried by the coefficients M_0 and N_0 . For the sake of simplification, we denote the rotation angle in a half cycle as

$$\theta(B, T) = \int_0^{T/2} \Delta\omega(t) dt, \tag{3.19}$$

so θ is a function of both pulse amplitude and pulse period. In the squared pulse situation,

$$\begin{aligned}
M_0 &= \frac{\sin(\theta)}{\theta} \\
N_0 &= \frac{1 - \cos(\theta)}{\theta}.
\end{aligned}
\tag{3.20}$$

When θ is an integer multiple of 2π , both M_0 and N_0 go to zero, which means the coupling between hydrides and the target nuclei disappear at this situation, and no spin

order transfer could take place. Similarly, in the sine wave case, the expressions of M_0 and N_0 are

$$\begin{aligned} M_0 &= \frac{1}{T} \int_0^T \cos \left[\frac{\Delta\omega T}{2\pi} \left(1 - \cos \frac{2\pi t}{T} \right) \right] dt \\ N_0 &= \frac{1}{T} \int_0^T \sin \left[\frac{\Delta\omega T}{2\pi} \left(1 - \cos \frac{2\pi t}{T} \right) \right] dt, \end{aligned} \quad (3.21)$$

Alike, for the ramp pulse, we have

$$\begin{aligned} M_0 &= \frac{2}{\sqrt{\Delta\omega T}} \int_0^{\sqrt{\Delta\omega T}/2} \cos x^2 dx \\ N_0 &= \frac{2}{\sqrt{\Delta\omega T}} \int_0^{\sqrt{\Delta\omega T}/2} \sin x^2 dx. \end{aligned} \quad (3.22)$$

The zero-order average Hamiltonian of the AA'BB' system have a similar expression

$$\begin{aligned} \bar{\mathcal{H}}^{(0)} &= \Delta\omega_0 (\hat{L}_{1z} + \hat{L}_{2z}) + 2\pi J_{HH} (\hat{I}_1 \cdot \hat{I}_2) \\ &+ 2\pi J_{HL} \left\{ \hat{I}_{1z} \hat{L}_{1z} + M_0 (\hat{I}_{1x} \hat{L}_{1x} + \hat{I}_{1y} \hat{L}_{1y}) + N_0 (\hat{I}_{1x} \hat{L}_{1y} - \hat{I}_{1y} \hat{L}_{1x}) \right\} \\ &+ 2\pi J_{HL} \left\{ \hat{I}_{2z} \hat{L}_{2z} + M_0 (\hat{I}_{2x} \hat{L}_{2x} + \hat{I}_{2y} \hat{L}_{2y}) + N_0 (\hat{I}_{2x} \hat{L}_{2y} - \hat{I}_{2y} \hat{L}_{2x}) \right\}, \end{aligned} \quad (3.23)$$

and its matrix form is displayed in Eq. (3.24). The basis used here is the singlet-triplet basis for both the dihydride and the two target nuclei. The coupling between states S_L^0 and T_L^0 stays unchanged, and the coupling between states T_L^+ and T_L^- is always zero. The rest couplings which are directly associated with the spin order transfer are adjustable. The signal enhancement of this 4-spin system is also confirmed by the numerical DMEx method (Fig. 3.3). A square pulse with fixed amplitude $B = 10\mu T$ is

$$\begin{aligned}
& \begin{matrix} T_H^+ S_L^0 \\ S_H^0 T_L^+ \end{matrix} \begin{pmatrix} T_H^+ S_L^0 & S_H^0 T_L^+ \\ \frac{\pi J_{HH}}{2} & \pi J_{HL}(M_0 - iN_0) \\ \pi J_{HL}(M_0 + iN_0) & -\frac{3\pi J_{HH}}{2} - \Delta\omega_0 \end{pmatrix} \\
& \begin{matrix} T_H^- S_L^0 \\ S_H^0 T_L^- \end{matrix} \begin{pmatrix} T_H^- S_L^0 & S_H^0 T_L^- \\ \frac{\pi J_{HH}}{2} & \pi J_{HL}(M_0 + iN_0) \\ \pi J_{HL}(M_0 - iN_0) & -\frac{3\pi J_{HH}}{2} + \Delta\omega_0 \end{pmatrix} \\
& \begin{matrix} T_H^+ T_L^- \\ T_H^0 T_L^0 \\ S_H^0 S_L^0 \\ T_H^- T_L^+ \end{matrix} \begin{pmatrix} T_H^+ T_L^- & T_H^0 T_L^0 & S_H^0 S_L^0 & T_H^- T_L^+ \\ \frac{\pi(J_{HH} - 2J_{HL})}{2} + \Delta\omega_0 & \pi J_{HL}(M_0 - iN_0) & -\pi J_{HL}(M_0 - iN_0) & 0 \\ \pi J_{HL}(M_0 + iN_0) & \frac{\pi J_{HH}}{2} & \pi J_{HL} & \pi J_{HL}(M_0 - iN_0) \\ -\pi J_{HL}(M_0 + iN_0) & \pi J_{HL} & -\frac{3\pi J_{HH}}{2} & -\pi J_{HL}(M_0 - iN_0) \\ 0 & \pi J_{HL}(M_0 + iN_0) & -\pi J_{HL}(M_0 + iN_0) & \frac{\pi(J_{HH} - 2J_{HL})}{2} - \Delta\omega_0 \end{pmatrix} \quad (3.24)
\end{aligned}$$

used, and the corresponding M_0 and N_0 have the same expression as that of the AA'B system (Eq. 3.20). If $(\gamma_H - \gamma_L)BT / 2 = 2n\pi$, the coupling between the dihydride and the target nuclei vanish, so the resulting polarization is zero along the vertical line of $T = 4.3ms$. The optimal condition for polarization by scanning both the offset field B_0 and the pulse period T is $B_0 = -0.16\mu T$, and $T = 4ms$ when the pulse amplitude is maintained at $B = 10\mu T$. Compared with the 3-spin system, the optimal offset shifted a little bit which is caused by the different spin configuration of the SABRE complex, but the optimal pulse period stays the same since J_{HL} is tuned identically in both 3-spin and 4-spin cases.

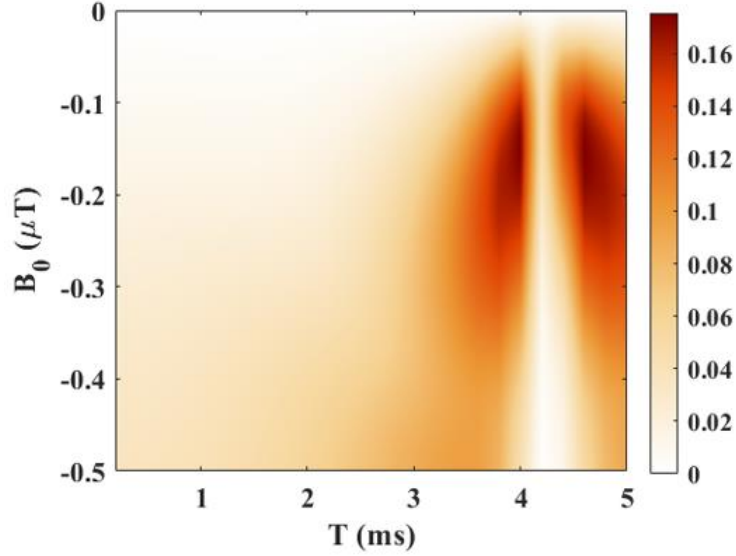


Figure 3.3: Polarization of a AA'BB' system varies with the square pulses period and the offset field. The pulse amplitude is pinned at $B = 10\mu T$, and the optimal condition of polarization is $B_0 = -0.16\mu T$ and $T = 4ms$. Simulation parameters: 100%

parahydrogen, $k_L = 24s^{-1}$, $k_H = 8s^{-1}$, $\frac{[C]}{[S]} = \frac{1}{10}$, $J_{HH} = -8Hz$, $J_{HL} = -25Hz$. Reprinted with permission from ref. 79.

Another important consideration is determining the appropriate truncation point for the Magnus expansion. The zero-order expansion is much simpler and more intuitive than the higher order terms, so it is helpful to find conditions where the zero-order term suffices. We analytically calculate the first and second order Magnus expansions. Based on Eq. (3.15) and (3.16), the commutation relations of $[\tilde{\mathcal{H}}(t_1), \tilde{\mathcal{H}}(t_2)]$ and $[[\tilde{\mathcal{H}}(t_1), \tilde{\mathcal{H}}(t_2)], \tilde{\mathcal{H}}(t_3)]$ are needed.

$$\begin{aligned}
& [\tilde{\mathcal{H}}(t_1), \tilde{\mathcal{H}}(t_2)] / (2\pi J_{HL}) \\
&= \frac{i\pi}{2} \Delta\omega_0 \left\{ \begin{aligned} & (M(t_2) - M(t_1)) (\hat{I}_{1x} \hat{L}_y - \hat{I}_{1y} \hat{L}_x) \\ & - (N(t_2) - N(t_1)) (\hat{I}_{1x} \hat{L}_x + \hat{I}_{1y} \hat{L}_y) \end{aligned} \right\} \\
&+ i\pi J_{HH} (M(t_2) - M(t_1)) \left\{ \begin{aligned} & \hat{I}_{1z} (\hat{I}_{2x} \hat{L}_y - \hat{I}_{2y} \hat{L}_x) \\ & + \hat{I}_{2z} (\hat{I}_{1y} \hat{L}_x - \hat{I}_{1x} \hat{L}_y) \end{aligned} \right\} \\
&+ i\pi J_{HH} (N(t_2) - N(t_1)) \left\{ \begin{aligned} & -\hat{I}_{1z} (\hat{I}_{2x} \hat{L}_x + \hat{I}_{2y} \hat{L}_y) \\ & + \hat{I}_{2z} (\hat{I}_{1x} \hat{L}_x + \hat{I}_{1y} \hat{L}_y) \end{aligned} \right\} \\
&- \frac{i\pi}{2} J_{HL} (M(t_1)N(t_2) - M(t_2)N(t_1)) (\hat{I}_{1z} - \hat{L}_z).
\end{aligned} \tag{3.25}$$

$$\begin{aligned}
& \left\{ \left[[\tilde{\mathcal{H}}(t_1), \tilde{\mathcal{H}}(t_2)], \tilde{\mathcal{H}}(t_3) \right] + \left[\tilde{\mathcal{H}}(t_1), [\tilde{\mathcal{H}}(t_2), \tilde{\mathcal{H}}(t_3)] \right] \right\} / (2\pi J_{HL}) \\
&= \pi\Delta\omega_0 J_{HH} \{M(t_3) - 2M(t_2) + M(t_1)\} \left\{ \hat{I}_{1z} (\hat{I}_{2x} \hat{L}_x + \hat{I}_{2y} \hat{L}_y) - \hat{I}_{2z} (\hat{I}_{1x} \hat{L}_x + \hat{I}_{1y} \hat{L}_y) \right\} \\
&+ \pi\Delta\omega_0 J_{HH} \{N(t_3) - 2N(t_2) + N(t_1)\} \left\{ \hat{I}_{1z} (\hat{I}_{2x} \hat{L}_y - \hat{I}_{2y} \hat{L}_x) + \hat{I}_{2z} (\hat{I}_{1y} \hat{L}_x - \hat{I}_{1x} \hat{L}_y) \right\} \\
&+ \left(\frac{\pi^2}{2} J_{HL}^2 + \frac{(\Delta\omega_0)^2}{4} \right) \{M(t_3) - 2M(t_2) + M(t_1)\} (\hat{I}_{1x} \hat{L}_x + \hat{I}_{1y} \hat{L}_y) \\
&+ \left(\frac{\pi^2}{2} J_{HL}^2 + \frac{(\Delta\omega_0)^2}{4} \right) \{N(t_3) - 2N(t_2) + N(t_1)\} (\hat{I}_{1x} \hat{L}_y - \hat{I}_{1y} \hat{L}_x) \\
&- \left(\frac{\pi^2}{2} J_{HL}^2 + \frac{\pi^2}{4} J_{HH} J_{HL} \right) \{M(t_3) - 2M(t_2) + M(t_1)\} (\hat{I}_{2x} \hat{L}_x + \hat{I}_{2y} \hat{L}_y) \\
&- \left(\frac{\pi^2}{2} J_{HL}^2 + \frac{\pi^2}{4} J_{HH} J_{HL} \right) \{N(t_3) - 2N(t_2) + N(t_1)\} (\hat{I}_{2x} \hat{L}_y - \hat{I}_{2y} \hat{L}_x) \\
&- \frac{\Delta\omega_0}{8} \{ (M(t_3) - M(t_2))M(t_1) + (N(t_3) - N(t_2))N(t_1) \} (\hat{I}_{1z} - \hat{L}_z) \\
&+ \frac{\pi}{4} J_{HH} \{ (M(t_3) - M(t_2))M(t_1) + (N(t_3) - N(t_2))N(t_1) \} \hat{I}_{2z} (\hat{I}_{1z} - \hat{L}_z) \\
&+ \frac{\pi}{8} J_{HH} \{ (M(t_3) - M(t_2))M(t_1) + (N(t_3) - N(t_2))N(t_1) \} (\hat{I}_{1x} \hat{I}_{2x} + \hat{I}_{1y} \hat{I}_{2y}) \\
&+ \frac{\pi}{8} J_{HH} \{ M(t_2)(N(t_3) + N(t_1)) - (M(t_3) + M(t_1))N(t_2) \} (\hat{I}_{1x} \hat{I}_{2y} - \hat{I}_{1y} \hat{I}_{2x})
\end{aligned} \tag{3.26}$$

Each pulse shown in Fig. 3.1 have an axisymmetric Hamiltonian in the rotating frame, because $M(t)$ and $N(t)$ of an anti-symmetric pulse shape are axisymmetric. According to Eq. (3.6), $M(t)$ and $N(t)$ refer to the cosine and sine value of the rotation angle $\int_0^t \Delta\omega(t') dt'$ at time t . For an anti-symmetric pulse shape, in each cycle

$$\int_0^t \Delta\omega(t') dt' = \int_0^{T-t} \Delta\omega(t') dt'. \quad (3.27)$$

Accordingly, $M(t) = M(T-t)$ and $N(t) = N(T-t)$. Therefore, the Hamiltonian is axisymmetric

$$\tilde{\mathcal{H}}(t) = \tilde{\mathcal{H}}(T-t). \quad (3.28)$$

Because of this axial symmetry, all the odd order Magnus expansions are zero.

Visualizing how each matrix element of the exact average Hamiltonian $\bar{\mathcal{H}}$ varies with the pulse period T reveals the reason why the higher order expansion could be omitted (shown in Fig. 3.4). It should be noted that the pulse period T could not be too long in most SABRE system with reasonable exchange rate (usually $\leq 50s^{-1}$), otherwise the SABRE complex only experiences a constant high magnetic field during its lifetime. Therefore, we are only interested in pulse periods that are smaller or comparable to the lifetime of SABRE complex. For the sake of conciseness, here we only plot the square pulse and ramp pulse and only display the result of one of the two 3×3 subspace since the other one has similar behavior.

In the zero-order case, only the non-secular matrix elements which connect the α_L state and β_L states are altered, and the resulting M 's and N 's are identical.

However, for the higher orders, diagonal elements are tuned as well, which is caused by the term $\hat{I}_{1z} - \hat{L}_z$ and $\hat{I}_{1z}\hat{I}_{2z} - \hat{I}_{2z}\hat{L}_z$ in the second order expansion. Even though the M 's and N 's diverge in the higher order approximation, this divergence is always very small. So are the alters of the three diagonal elements. In Fig. 3.4, we plot the diagonal elements

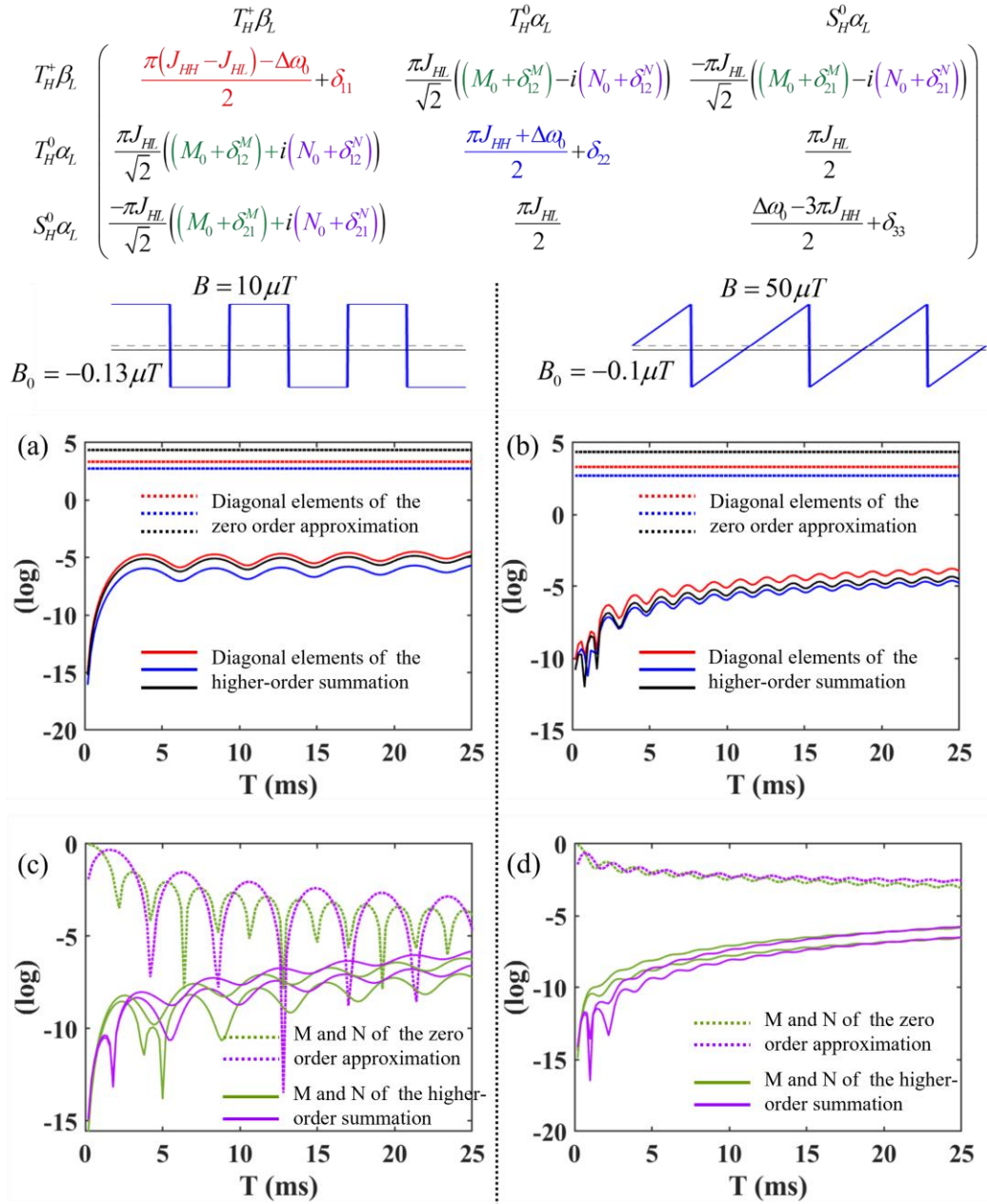


Figure 3.4: A graphical representation of both the diagonal elements and off-diagonal M and N as a function of pulse period T . The results of the square pulse (left) and the ramp pulse (right) are explicitly displayed here. The upper two plots ((a) and (b)) refer to the three diagonal elements, while the lower two ((c) and (d)) indicate the changes of the off-diagonal M and N . In all cases the dotted lines represent the zero order results while the full curves correspond to the summation of all the higher orders (excluding the zero-order). Reprinted with permission from ref. 79.

as well as the off-diagonal M and N . The way we numerically calculate the summation of all the higher-order expansions (excluding the zero-order) is subtracting the zero-order approximation from the exact average Hamiltonian. To visually demonstrate that this summation of higher-order expansions does not have a significant impact, we compare the values associated with zero order approximation to the values associated with subtraction. According to Fig. 3.4, the terms associated with the subtraction are at least two orders of magnitude smaller than their zero-order counterparts. Therefore, all higher order Magnus expansions could be neglected, and the zero-order expansion is indeed a reliable approximation of the whole average Hamiltonian.

3.1.3 Correctly Attenuated J-coupling Enhances Polarization

A direct numerical evaluation of the full effective Hamiltonian using Eq. (3.12) gives a good comparison to double check the validity of this zero-order expansion. Initially, a meticulous analysis of the square pulse is conducted. Each cycle of the square pulse can be broken down into two constant fields, $B_0 + B$ and $B_0 - B$, in time sequence. Labeling the corresponding time-independent Hamiltonians as $\hat{\mathcal{H}}_+$ and $\hat{\mathcal{H}}_-$, the propagator of this spin system is expressed as

$$\hat{\mathcal{U}} = \exp(-i\hat{\mathcal{H}}_- T / 2) \exp(-i\hat{\mathcal{H}}_+ T / 2) = \exp(-i\bar{\mathcal{H}}T). \quad (3.29)$$

Extracting the average Hamiltonian by an expression such as $\bar{\mathcal{H}} = i \log(\hat{\mathcal{U}}) / T$ can be done numerically by diagonalizing $\hat{\mathcal{U}}$ to a matrix $e^{i\Lambda}$, then taking the log of each eigenvalue (which will always have magnitude 1), $\hat{\mathcal{U}} = V e^{i\Lambda} V^\dagger$; $\log(\hat{\mathcal{U}}) = Vi\Lambda V^\dagger$, but this lead to a well-known ambiguity as the phase is only determined modulo 2π . This ambiguity is avoided by multiplying J_{HH} and J_{HL} by a scale factor a , calculating $\bar{\mathcal{H}}$ in the limit of very small a , and correcting for 2π phase jumps as a is increased to 1. This approach justifies that the zero-order expansion is already a good approximation of the average Hamiltonian (Fig. 3.5), and higher orders can be neglected. M_0 , N_0 , and $\sqrt{M_0^2 + N_0^2}$ (solid curves) calculated with the zero-order average Hamiltonian are in great agreement with their numerical counterparts (dashed curves). The coupling magnitude $\sqrt{M_0^2 + N_0^2}$ vanishes at $\theta = 2n\pi$, which agrees with the analytical expressions of M_0 and N_0 (Eq. (3.20)). $\sqrt{M_0^2 + N_0^2}$ attenuates as θ increases, in that it cannot fully recover to the previous maximum. The value of $\sqrt{M_0^2 + N_0^2}$ is in the range of $[0,1]$, which is obvious from the formula of $M(t)$ and $N(t)$ (equation (3.6)) because they are conjugate trigonometric functions. In other words, the coupling between hydrides and target nuclei can only be attenuated instead of being increased.

Unexpectedly, a diminished coupling strength yields much higher polarization for the smaller off-diagonal matrix elements reduce the coupling of unwanted states.

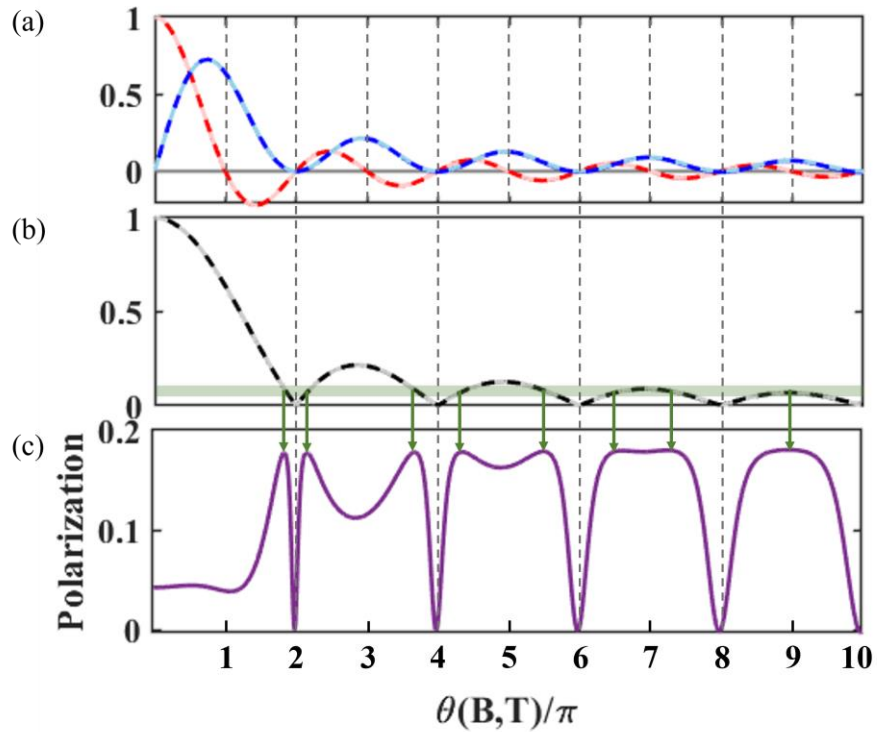


Figure 3.5: (a) Curves of M and N as a function of $\frac{\theta}{\pi}$. The solid Lines (underlying bright red and bright blue curves) are the zero-order theoretical approximation of M and N , namely, M_0 and N_0 , and the dashed lines (light red and blue) are the exact values of M and N calculated with numerical method. (b) shows how the value of $\sqrt{M^2 + N^2}$ varies with $\frac{\theta}{\pi}$. Likewise, the solid curve (underlying black) and the dashed line (grey) correspond to the theoretical approximation and the numerical result, respectively. The horizontal green bar indicates the optimal value of $\sqrt{M^2 + N^2}$. (c) Numerically simulated 15N polarization of a 3-spin system with the pulse amplitude being fixed at $10\mu T$ and the offset being maintained at $-0.13\mu T$. The green arrows mark the maximum signals and their corresponding value of $\sqrt{M^2 + N^2}$. Reprinted with permission from ref. 79.

Figure 3.5 (b) and (c) gives the relationship between the final polarization level and the value of $\sqrt{M_0^2 + N_0^2}$ with the offset field B_0 fixed at $-0.13\mu T$. The polarization is

numerically simulated with the DMEx¹³ method, and the dependence on θ indicates that when the interaction strength reduces to $\sqrt{M_0^2 + N_0^2} \sim 0.066$ (shown with a horizontal green bar in Fig. 3.5(b)), polarization is maximized. This unbalanced square wave indeed yields a large increase in signal. However, the optimal interaction strength $\sqrt{M_0^2 + N_0^2} \sim 0.066$ is very close to zero, and the polarization oscillations in Fig. 3.5 (c) imply that the large signals are not robust to imperfections of the pulse sequence such as inhomogeneity. This issue could be avoided if $\sqrt{M_0^2 + N_0^2}$ reduces gradually and maintain at 0.066 for long instead of periodically going to zero. To find a pulse sequence with this behavior of $\sqrt{M_0^2 + N_0^2}$, more complex wave forms must be considered – sine wave, chirped pulse, and ramp pulse.

3.1.4 Symmetry Reduces Robustness

Similarly, we could also visualize the M_0 , N_0 , and $\sqrt{M_0^2 + N_0^2}$ of all the other pulse sequences as a function of $\frac{\theta(B,T)}{\pi}$ (Fig. 3.6). Same as the square pulse, the M_0 and N_0 of the sine wave and the isosceles triangle pulse periodically vanish at the same time. However, the chirped pulse and ramp pulse have regularly declined curve trend which is exactly what we are looking for. The chirped pulse we study consists of evenly growing wavelength in each period, $\tau_0, \tau_0 + \Delta\tau, \dots, \tau_0 + m\Delta\tau$, and its smallest period is

$\sum_{j=0}^m (\tau_0 + j\Delta\tau) = T$. The specific chirped pulse in figure 3.6 (c) has $\tau_0 = \Delta\tau = 0.2ms$.

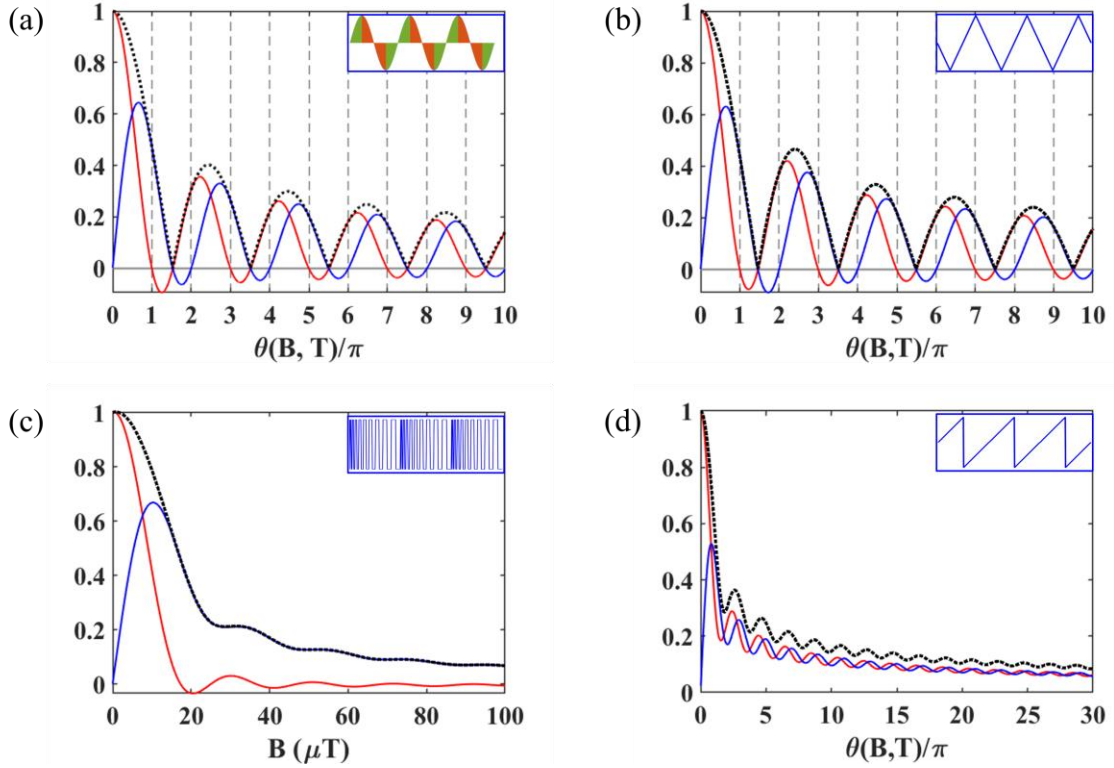


Figure 3.6: Depiction of how M_0 (red curve), N_0 (blue curve), and $\sqrt{M_0^2 + N_0^2}$ (black dotted curve) vary as a function of the pulse period and/or pulse amplitude. (a) sine wave, (b) isosceles triangle pulse, (c) chirped square pulse, and (d) ramp pulse. The offset field is maintained at $-0.13\mu T$. Reprinted with permission from ref. 79.

$\sqrt{M_0^2 + N_0^2}$ of this pulse is close to the optimal value 0.066 when the pulse amplitude B is larger than $40\mu T$, accordingly the experimental robustness to the pulse amplitude is indeed improved. The last ramp pulse (Fig. 3.6 (d)) turns out to be robust to both the pulse period and the field strength. Unlike the square pulse and the sine wave whose flip-flop terms can be fully averaged out when M_0 and N_0 vanish at the same time, the ramp pulse successfully avoids zero points, and in a wide period and amplitude domain $\sqrt{M_0^2 + N_0^2}$ always stays close to the optimal value 0.066.

All the highly symmetric pulses we have studied here share a common symmetrical property, which is central axial symmetry, since every pulse has a symmetric trajectory with respect to the center axis of each half cycle (Fig. 3.7(a)). Pulses with higher symmetry intuitively would be expected to produce cleaner pumping dynamics. However, given the cases shown above this additional symmetry causes the periodic vanishment of the effective J_{HL} . To understand this key symmetric feature, note that for an arbitrary oscillating pulse shape, M_0 and N_0 are given by

$$\begin{cases} M_0 = \frac{1}{T} \int_0^T M(t) dt = \frac{1}{T} \int_0^T \cos\left(\int_0^t \Delta\omega(t') dt'\right) dt \\ N_0 = \frac{1}{T} \int_0^T N(t) dt = \frac{1}{T} \int_0^T \sin\left(\int_0^t \Delta\omega(t') dt'\right) dt \end{cases} \quad (3.30)$$

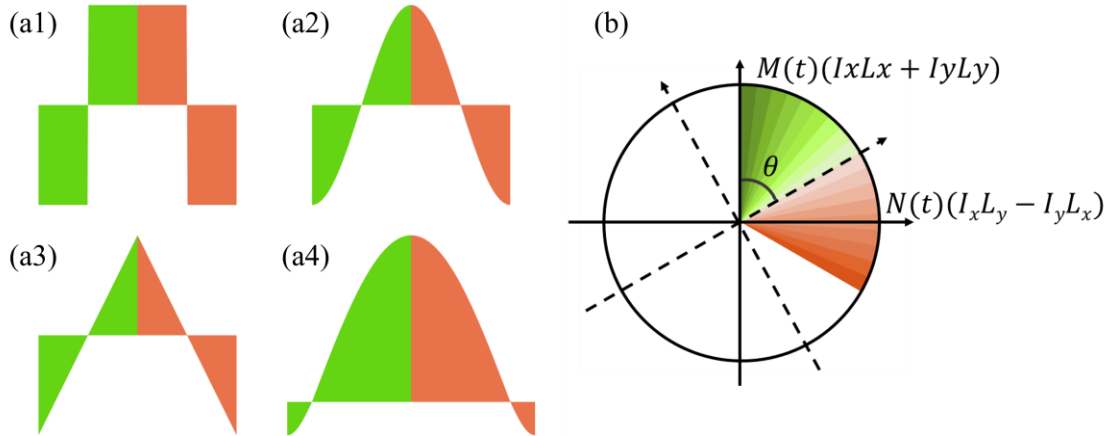


Figure 3.7: (a) Examples of center axisymmetric pulses. (a1) square pulse, (a2) sine or cosine wave, (c) isosceles triangle pulse, (d) an arbitrary axisymmetric pulse. (b) A coordinate transformation by rotating the original rectangular coordinate system (solid line) an angle θ to the new system (dashed line).

which are integrals of the cosine and sine function of the instantaneous angle $\int_0^t \Delta\omega(t') dt'$. In other words, M_0 and N_0 are the integrals of the projections of a

rotating unit vector on the x-axis and y-axis, respectively, in a rectangular coordinate system. The rotation angle of the first and second half cycle is denoted by

$$\int_0^{T/2} \Delta\omega(t') dt' = \int_{T/2}^T \Delta\omega(t') dt' = \theta \quad (3.31)$$

A coordinate transformation is made in the way that the x-axis equally divides these two θ . M'_0 and N'_0 in this new coordinate are

$$\begin{cases} M'_0 = \cos\theta M_0 + \sin\theta N_0 = \text{Number} \\ N'_0 = -\sin\theta M_0 + \cos\theta N_0 = 0 \end{cases}, \quad (3.32)$$

where M'_0 equals to some number which depends on the specific pulse shape, while N'_0 is always zero for the angular frequency $\Delta\omega(t')$ is symmetric with respect to the x'-axis. Solving M_0 and N_0 gives

$$\begin{cases} M_0 = \cos\theta \times \text{Number} \\ N_0 = \sin\theta \times \text{Number} \end{cases}. \quad (3.33)$$

To guarantee $N'_0 = 0$, one of the following condition must be true – (i) $\theta = \left(n + \frac{1}{2}\right)\pi$,

$M_0 = 0$; (ii) $\theta = n\pi$, $N_0 = 0$; (iii) $M_0 = N_0 = 0$. Consider two specific cases, $\theta = \frac{\pi}{2} + \delta$,

$M_0 = \sin\delta \times \text{Number}$, and $\theta = \frac{3\pi}{2} - \delta$, $M_0 = -\sin\delta \times \text{Number}$, with $0 < \delta \ll 1$. Since

these two values are opposite, and M_0 is a continuous function of pulse period T and

pulse amplitude B , a zero point must exist between $\frac{\pi}{2}$ and $\frac{3\pi}{2}$. However, $\cos\theta \neq 0$ in

the range of $\left(\frac{\pi}{2}, \frac{3\pi}{2}\right)$, which means that N_0 much vanish. Therefore $M_0 = N_0 = 0$ has been proved, and these coincident zero points recur after every 2π rotation which accounts for the periodic vanishment of J_{NH} . Frequent zero-crossings impose a serious constraint for all axisymmetric pulses on the unstable fields, particularly if inhomogeneity is present. Only lower symmetric pulses without axial symmetry is possible to avoid this issue, and the chirped pulse and ramp pulse shown in Figure 3.6 (c) and (d) are two prime examples.

3.2 Numerical and Experimental Verification

The main theoretical conclusions of the previous section are that a oscillating pulse with correctly tuned magnitude or period enhances the SABRE polarization by effectively adjusting the J-coupling between the hydride and the target nuclei, and an axisymmetric pulse is certain to yield a periodic vanishment of the effective J_{NH} which makes the improved polarization very vulnerable to the unstable magnetic field. In this section, we verify the analytical results with both simulations and experiments.

All oscillating pulse SABRE-SHEATH experiments were performed by bubbling 43% parahydrogen through a methanol-d4 solution under 7 bars of pressure at room temperature. The SABRE sample used here was prepared by adding 2 μ L 15 N-acetonitrile (50mM), 1 μ L natural abundance 14 N-pyridine (25mM), and 1.3mg the catalyst precursor [IrCl(COD)(IMes)] (4.4mM) into 500 μ L deuterated methanol solvent. The catalyst was first activated by bubbling hydrogen gas through the SABRE sample for 30 min to generate SABRE complex $[\text{IrH}_2(^{15}\text{N-MeCN})(^{14}\text{N-Py})_2(\text{IMes})]+(^{15}\text{N-MeCN}=\text{N-}^{15}\text{N-})$

acetonitrile)(^{14}N -Py= ^{14}N -pyridine). The whole sample was then bubbled for 60s inside a solenoid coil within a μ -metal magnetic shield (Fig. 3.8). A function generator was connected to the solenoid coil to general all kinds of magnetic pulses in the coil where the polarization transfer occurs. Finally, the sample was manually transferred (1-2s) to a 1 Tesla ^{15}N NMR spectrometer for detection.

For all the pulses displayed in Fig. 3.1, we numerically simulated how the final polarization varies with both the offset field and the oscillating pulse. Each 3D plot in Fig. 3.9 is a numerical simulation of a specific pulse sequence and comes accompanied with two 2D experimental data as well as the corresponding numerical fitting. In the cases of axisymmetric pulse, square pulse and sine wave, we swept the offset and the pulse period T . In each situation, the optimal offset field is $\sim 0.13\mu\text{T}$ rather than $\sim 0.6\mu\text{T}$

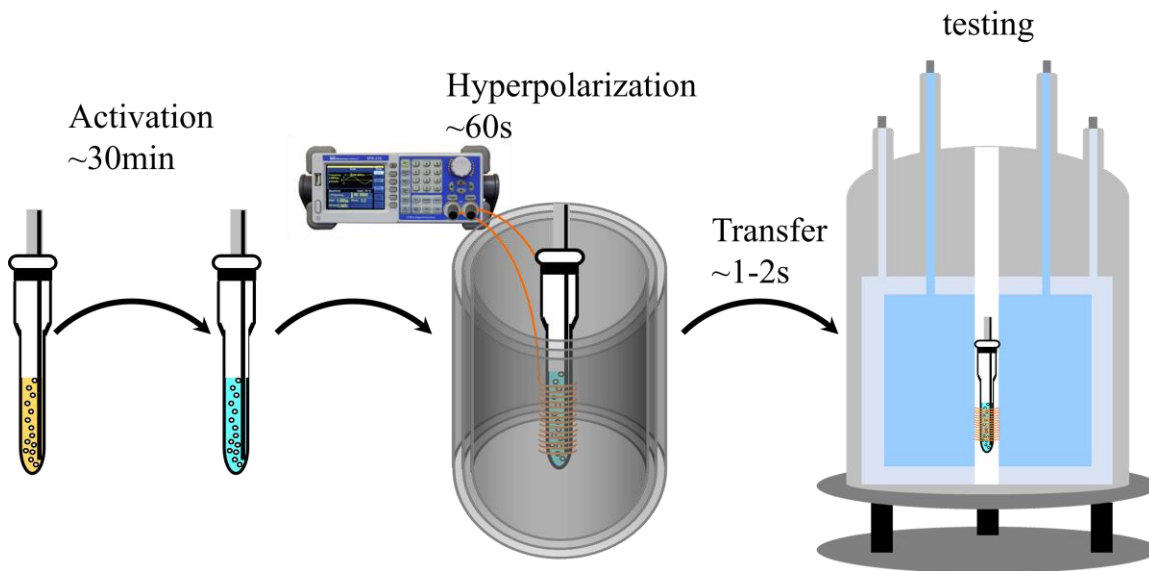


Figure 3.8: Experimental procedure of SABRE-SHEATH. First, activate the SABRE sample by bubbling hydrogen gas through the solution for about 30 minutes. Then, hyperpolarize the sample in a shield. Finally, transfer the sample into a magnetometer for detection.

in the CW SABRE-SHEATH case, and the polarization periodically vanishes with the change of the pulse period. The amplitude of the square pulse was maintained at $10\mu\text{T}$. At the points $T = 20.8\text{ms}$ and $T = 25\text{ms}$ in Fig 3.9(a2), $\theta = 2n\pi$ which means M_0 and N_0 are both zero, therefore no polarization could be produced. The polarization of the sine wave has a similar periodicity. Fig. 3.9(b1) shows the polarization of a sine wave pulse as a function of both the pulse period and the offset field while the pulse amplitude is maintained at $50\mu\text{T}$. We varied either the pulse period ($1\text{ms} \leq T \leq 8\text{ms}$, $B_0 = -0.13\mu\text{T}$) in Fig. 3.9(b2), or the offset field ($-1\mu\text{T} \leq B_0 \leq 0\mu\text{T}$, $T = 3.5\text{ms}$) in Fig. 3.9(b3). In agreement with the theoretical predictions, the final polarization periodically reduces to zero at a frequency corresponding to $\Delta\omega$, and the optimal pulse periods come close to zero polarization points.

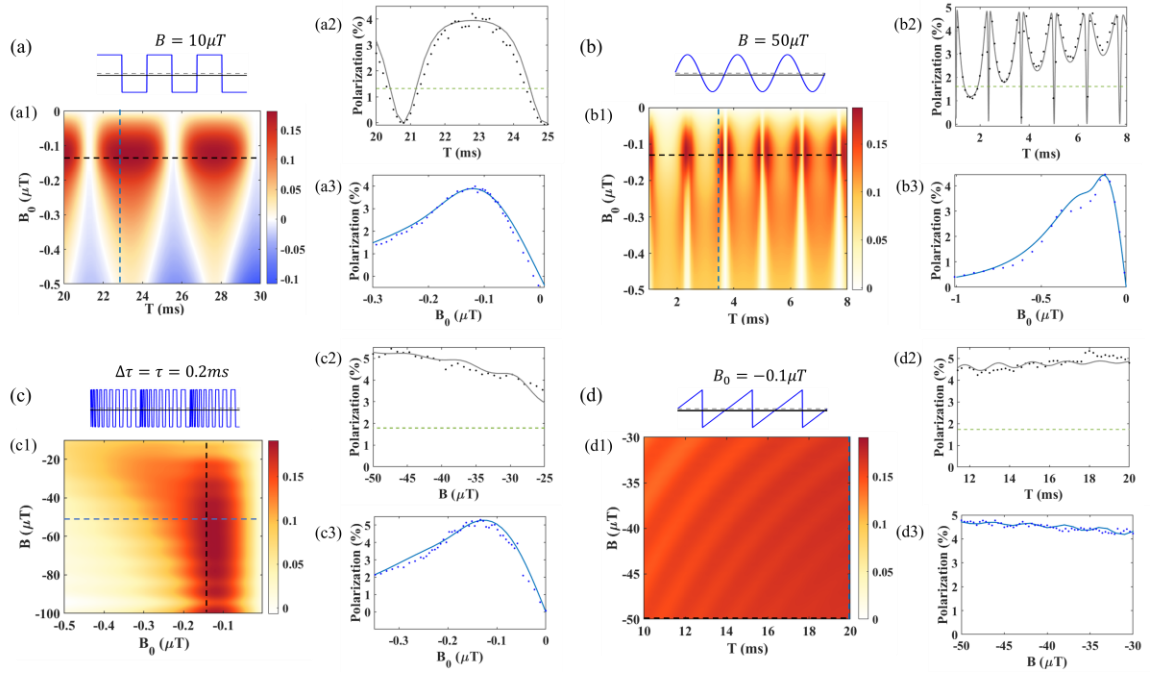


Figure 3.9: Experimental validation of the theoretical predictions. (a) Square pulse (a1) Theoretical effects of a square pulse sequence with a fixed amplitude $B = 10\mu T$ and various pulse period and offset field. (a2) Comparison of theoretical calculations with experimental data holding $B_0 = -0.13\mu T$ and varying T . (a3) Comparison of theoretical calculations with experimental data hold $T = 22.7ms$ and varying B_0 . (b) Sine wave (b1) Theoretical effects of a sine wave sequence with a fixed amplitude $B = 50\mu T$ and changing pulse period and offset field. (b2) Comparison of theoretical calculations with experimental data holding $B_0 = -0.13\mu T$ and varying T . (b3) Comparison of theoretical calculations with experimental data holding $T = 3.5ms$ varying B_0 . (c) Chirped pulse (c1) Theoretical effects of a chirped pulse with evenly increasing pulse length from 0.2ms to 2ms in a step of 0.2ms. The offset and pulse amplitude are both scanned. (c2) Comparison of theoretical calculations with experimental data holding $B_0 = -0.13\mu T$ and varying B . (c3) Comparison of theoretical calculations with experimental data holding $B = 50\mu T$ and varying B_0 . (d) Ramp pulse (d1) Theoretical effects of a ramp pulse with a fixed offset field $B_0 = -0.1\mu T$. (d2) Comparison of theoretical calculations with experimental data holding $B_0 = -0.1\mu T$, $B = 50\mu T$ and varying T . (d3) Comparison of theoretical calculations with experimental data holding $T = 20ms$ and varying B . The green dashed lines in each subfigure (2) refer to the maximum polarization obtained with the CW SABRE-SHEATH method using the same sample. Simulation parameters: 100% parahydrogen, $k_L = 24s^{-1}$, $k_H = 8s^{-1}$, $\frac{[C]}{[S]} = \frac{1}{10}$, $J_{HH} = -8Hz$, $J_{HL} = -25Hz$. The maximum polarization for a continuous field experiment (with 43% parahydrogen as used experimentally) is marked by the dashed green lines (~1.6%). Reprinted with permission from ref. 79.

In the case of chirped pulse (Fig. 3.9(c)), we swept the offset field B_0 and the pulse amplitude B because the experimental operation is much simpler compared to switching the pulse period. The periodic vanishment of the final polarization disappears. The optimal offset is maintained in the range from $-0.18\mu T$ to $-0.08\mu T$, and the polarization is robust to all pulse amplitudes larger than $40\mu T$ and stays within the range from 16.5% to 19%. Fig. 3.9(d) shows the results of the ramp pulse. We have already known the optimal offset is in close to $\pm 0.13\mu T$, so the offset field was held at $-0.1\mu T$,

and both the pulse period and pulse amplitude were varied. Fig. 3.9(d1) clearly displays that in a wide range of both the pulse period and the pulse amplitude the final polarization always stays close to the maximum, which has been confirmed by experiments (Fig. 3.9(d2) and (d3)). By varying the pulse period ($11ms \leq T \leq 20ms$, $B = 50\mu T$, $B_0 = -0.1\mu T$), we always obtained almost maximum polarization. All the analysis based on theory is in accordance with the experimental results. The signal enhancement of these oscillating pulse sequences is as high as 300%.

Based on all the theoretical analysis and experimental verification, we could safely draw some conclusions. The time-dependent information of the oscillating pulse in the lab frame is transferred to the time-varying effective J_{NH} in an interaction frame (Eq. (3.5)) created with rotation operator $\hat{U}(t) = \exp(-i\hat{L}_z \int_0^t \Delta\omega(t') dt')$, which is a general truth for all time-dependent pulses along z-direction. If the pulse is antisymmetric, with a low offset field, the zero-order average Hamiltonian is a good approximation of the spin system, which is also a generic conclusion and has nothing to do with the pulse shape. In addition, if the pulse has axial symmetry by a phase shift, the flip-flop terms periodically vanish with the pulse period or the pulse amplitude (Eq. (3.31)-(3.33)), which guarantees that $\sqrt{M_0^2 + N_0^2}$ could be any value in $[0,1]$ including 0.066. Consequently, adding an offset around $\pm 0.13\mu T$ yields maximum polarization. While, for a non-axisymmetric pulse shape, such as the chirped pulse and the ramp pulse, $\sqrt{M_0^2 + N_0^2}$ is also in the range of $[0,1]$ in theory, but it slowly approaches zero instead. We need to make sure that

$\sqrt{M_0^2 + N_0^2}$ reaches 0.066 within a reasonable region of pulse period which could not be longer than the lifetime of the SABRE complex. The chirped pulse and the ramp pulse with the specific pulse parameters are precisely modulated to work properly.

3.3 Validity of Level Anti-crossings

Different models and theories have been conceived to understand and optimize the performance of SABRE. The one which drew most attention and had long been accepted is level anti-crossings (LAC)^{66, 83-86}. LAC is a useful tool in many spectroscopic applications and has been widely used in SABRE system to predict or explain the optimal magnetic field used in SABRE experiment. Level anti-crossings describe the phenomenon that the two energy levels of a two-state quantum system avoid crossing in the presence of an extra coupling between the two basis states. For example, consider a two-level system with Hamiltonian

$$\hat{\mathcal{H}} = \begin{pmatrix} \Sigma & \kappa \\ \kappa & 0 \end{pmatrix}, \quad (3.34)$$

where Σ and κ are the energy difference and the coupling between the two basis states, respectively. Without the coupling, the two energy levels intersect at the point $\Sigma = 0$ (Fig. 3.10(a)). However, with the extra coupling κ the crossing at $\Sigma = 0$ is avoided (Fig. 3.10(b)). At the avoided crossing the two basis states are maximally superposed which leads to the maximum population flow between the two basis states.

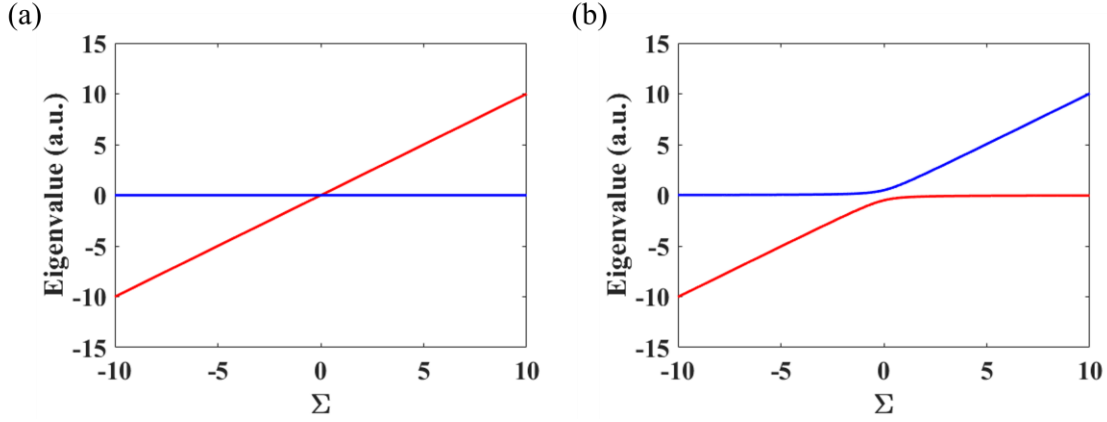


Figure 3.10: (a) Level crossing of a two-level system. (b) Level anti-crossing of the same system with an extra coupling $\kappa = 0.5$.

This LAC theory claims that the avoided crossing region reveals the optimal condition for SABRE. However, for the AA'B system used here the optimal magnetic field of SABRE-SHEATH at room temperature is $\sim \pm 0.6 \mu T$, which is far from the value $\sim \pm 0.04 \mu T$ predicted by LACs. It has been demonstrated that the LAC condition does not even give qualitatively correct predictions except for very small couplings and very slow exchange⁷⁷. Fig. 3.11 depicts that the optimal magnetic field is not fixed and unchanging but varies with the exchange rates of k_H and k_L . The failure of the LAC condition here is mainly because it oversimplifies a 3×3 (or larger) subspace to a 2×2 space and usually cannot accurately account for the dynamics of the original system. Interestingly, though, the LAC condition becomes more relevant for the oscillating pulse SABRE, because the oscillating pulse reduces the off-diagonal elements in Eq. (3.18) but not the diagonal ones, thus improving the separation from unwanted states. Fig. 3.12 depicts how the energy levels of the first subspace in Eq. (3.18) vary with the offset field.

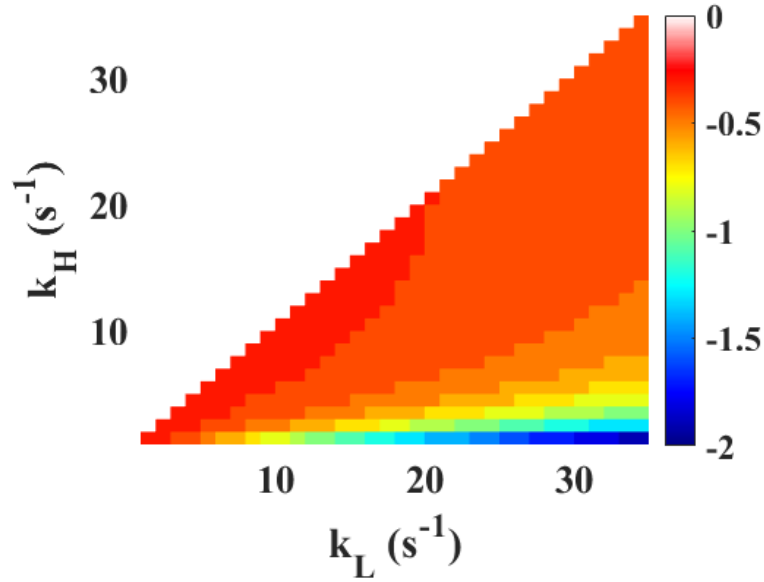


Figure 3.11: The optimal magnetic field of CW SABRE-SHEATH varies as the chemical exchange rates of both the dihydride and the target substrate. The optimal field is not fixing and changes from $-0.3\mu\text{T}$ to $-2\mu\text{T}$ (from red to blue).

The Fig. 3.12(a) relates to $J_{HL} = 0$, and no LACs occur because there is no interaction between the states. While Fig. 3.12(b) refers to the case of optimal interaction

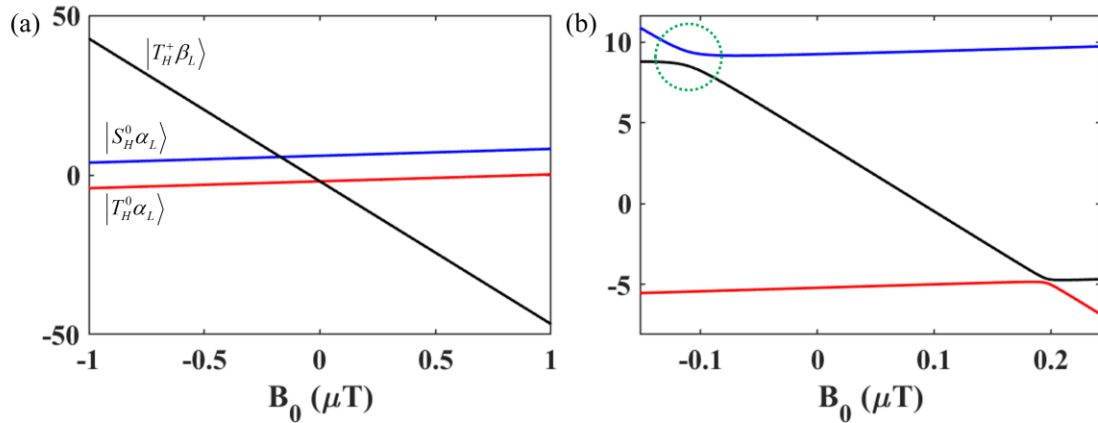


Figure 3.12: Eigenvalues as a function of the offset field. (a) corresponds to the case of $J_{HL} = 0$, while (b) refers to the case of optimal interaction $\sqrt{M_0^2 + N_0^2} \sim 0.066$ with $J_{HL} = -24\text{Hz}$. Reprinted with permission from ref. 79.

$\sqrt{M_0^2 + N_0^2} \sim 0.066$, in which the circled LAC is in great agreement with the optimal offset field $\pm 0.13 \mu T$.

A different model is introduced here to support the validity of LAC, which is also a AA'B system with the coupling between the two hydrides being positive, $J_{HH} = 8 Hz$, while $J_{HL} = -24 Hz$ stays unchanged. The same square pulse with amplitude $B = 10 \mu T$ is applied to this 3-spin system. Fig. 3.13(a) depicts how polarization varies with both the offset field and the pulse period, in which the optimal offset field is about $\pm 0.38 \mu T$. Fig. 3.13(b) displays the LACs of one 3×3 subspace with pulse period being fixed at the optimal value, 3.6ms, and the offset field changing from 0 to $0.4 \mu T$. The circled LAC at $B_0 \sim 0.37 \mu T$ agrees greatly with the optimal offset field. Therefore, the validity of LACs in oscillating pulse SABRE-SHEATH is confirmed again.

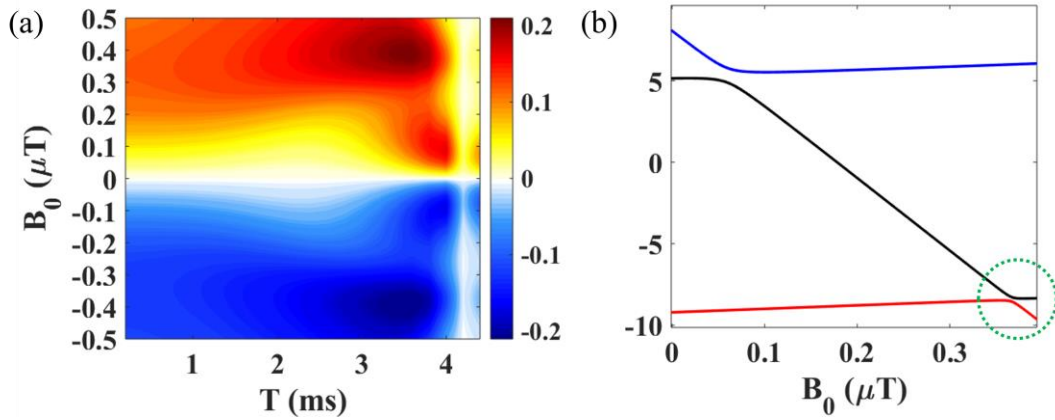


Figure 3.13: The prediction of LAC agrees with experimental optimum. The square pulse we use has a stable amplitude $10 \mu T$ while varying offset and pulse period. (a) displays polarization as a function of both the offset and the pulse period. The optimal offset and the optimal pulse period are $B_0 = \pm 0.38 \mu T$ and $T = 3.6 ms$, respectively. (b) is the corresponding LACs of one of the 3×3 subspaces. The circle LAC occurs near $B_0 \sim 0.37 \mu T$. Reprinted with permission from ref. 79.

3.4 Robustness to Exchange Rate

In this section, we use the DMEx¹³ simulation method to demonstrate that oscillating pulse SABRE-SHEATH is robust to variations of exchange rate. We use the same square pulse as in Fig. 3.9(a) and calculate the polarization, varying the exchange rate by a factor of 100. In the case of low substrate exchange rate (Fig. 3.14), the optimal condition stays around $B_0 = -0.11\mu\text{T}$ and $T = 4.1\text{ms}$. Ultimately, as the exchange rate of the substrate goes up, the optimal offset field increases and the pulse period decreases. Here we give an explanation using the quantum dynamics of SABRE. Fig. 3.15 shows the polarization of the target nuclei as a function of quantum evolution time. Both chemical exchange and relaxation processes are neglected. The four curves in Fig. 3.15(a) depicts the quantum dynamics using optimal parameters B_0 and T for the four

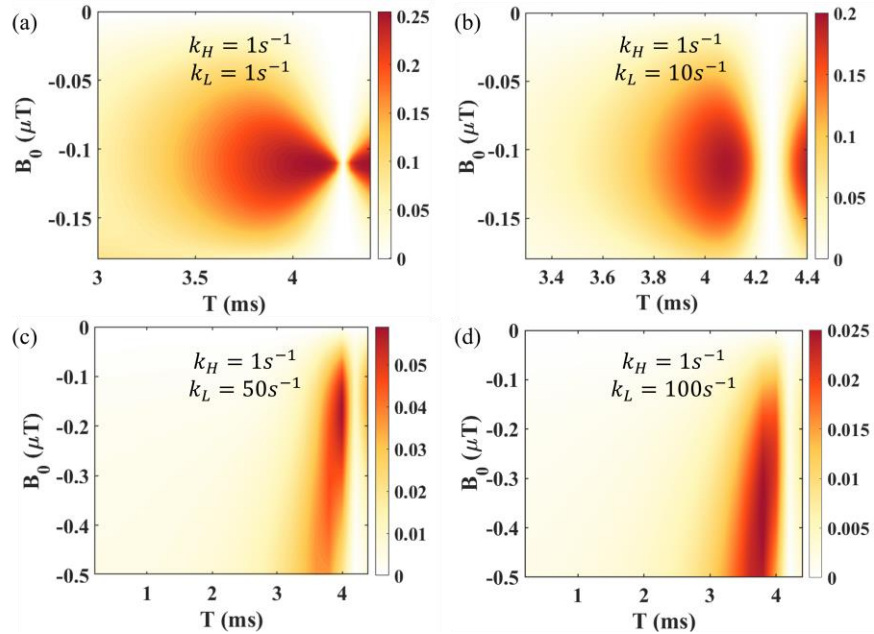


Figure 3.14: Different optimal polarization conditions caused by different exchange rates of substrate. (a) $k_H = 1\text{s}^{-1}$, $k_L = 1\text{s}^{-1}$, the optimal field is $-0.11\mu\text{T}$, and the optimal period

is 4.12ms. (b) $k_H = 1s^{-1}$, $k_L = 10s^{-1}$, the optimal field is also $-0.11 \mu T$, and the optimal period is 4.08ms. (c) $k_H = 1s^{-1}$, $k_L = 50s^{-1}$, the optimal field is $-0.17 \mu T$, and the optimal period is 4.0ms. (d) $k_H = 1s^{-1}$, $k_L = 100s^{-1}$, the optimal field is $-0.37 \mu T$, and the optimal period is 3.8ms. The four subplots have inconsistent color scales to show off more detail.

Reprinted with permission from ref. 79.

cases of Fig. 3.14, respectively. The red and blue curves clearly show that under the condition $B_0 = -0.11\mu T$ and $T = 4.1ms$, the polarization of the target nuclei could be raised up to 80%. However, when the chemical exchange processes are included, the quantum evolution is interrupted, which means the spin order transfer is interrupted. On one hand, if the lifetime of the SABRE complex is long, for example $k_L = 1s^{-1}$ or $k_L = 10s^{-1}$, there is enough time that the target nuclei could be polarized before they dissociate from SABRE catalyst. On the other hand, during a short lifetime, say $k_L = 50s^{-1}$ or $k_L = 100s^{-1}$, substantial spin order transfer process works better (the green and black curves). As pulse period T decreases, the value of $\sqrt{M_0^2 + N_0^2}$ grows, and the coupling between the hydrides and the target nuclei increases accordingly, which causes the spin order transfer faster (shown in Fig. 3.15(b)). For a fixed pulse period T , there exists an optimal offset field which maximizes the polarization of the substrate. In conclusion, maximizing SABRE polarization is a trade-off between the speed of spin order transfer and the largest transfer degree. Usually, the exchange rate k_L is in the range from $5s^{-1}$ to $50s^{-1}$, and the corresponding optimal condition remains near $B_0 = -0.11\mu T$ and $T = 4.1ms$ is still larger than the maximum signal (0.2%) produced by CW SABRE-SHEATH method.

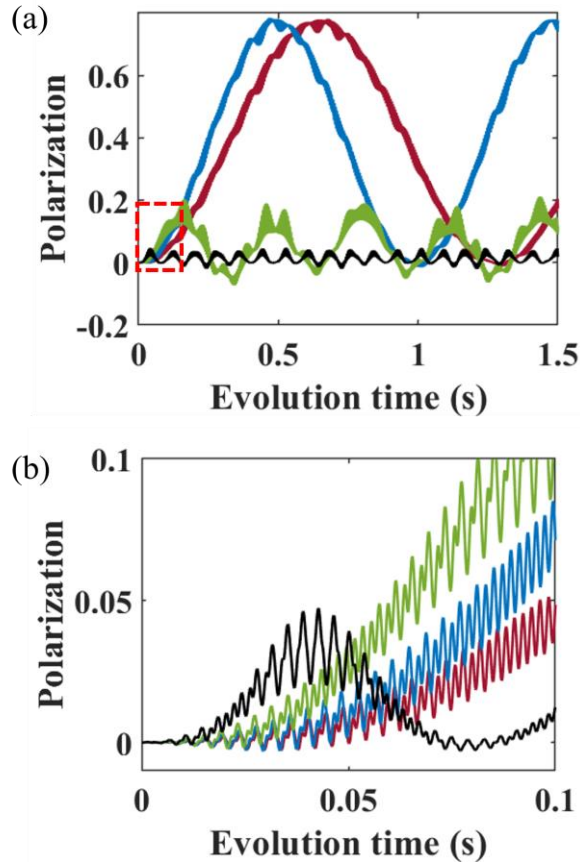


Figure 3.15: (a) Polarization generated by quantum evolution of the 3-spin system. Red curve $B_0 = -0.11\mu T$, $T = 4.12ms$; blue curve $B_0 = -0.11\mu T$, $T = 4.08ms$; green curve $B_0 = -0.17\mu T$, $T = 4.0ms$; black curve $B_0 = -0.31\mu T$, $T = 3.8ms$. (b) A zoomed-in version of the red box in figure (a). As the period goes down the spin order transfer process speeds up. Reprinted with permission from ref. 79.

3.5 Some Expansions of Oscillating Pulse SABRE

All the pulse sequences we have studied by now have such a small offset field that all the higher-order Magnus expansions are negligible. While, for relatively large offset, the zero-order expansion is no longer an eligible approximation. Based on the analysis of the CW SABRE, a high constant field ($>5\mu T$) yields ultra-low polarization (Fig. 2.10). However, in the presence of an extra oscillating pulse, a high polarization is still possible

with respect to a high offset field. Fig. 3.16 exhibits how the final polarization level change with the constant offset field while the oscillating pulse is fixed ($B = 10\mu T$ and $T = 23.5ms$). Even when the offset field is larger than the amplitude of the oscillating pulse, high polarization is still available. In both Fig. 3.2 and 3.9, the offset field is scanned but only in a narrow region of $[-0.5, 0.5]\mu T$, denoted with two blue dotted lines in Fig. 3.16. With a high offset, the Magnus expansion does not converge fast. Therefore,

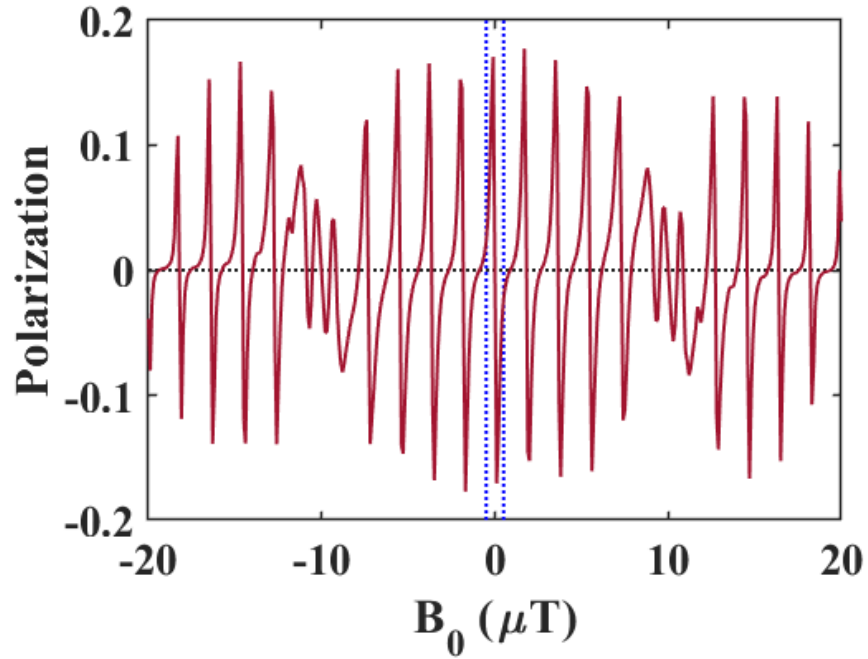


Figure 3.16: Polarization as a function of the offset field. The square pulse used here is unchanged with fixed pulse amplitude $B = 10\mu T$ and pulse period $T = 20.8ms$.

it is difficult to obtain an analytical expression of the approximate average Hamiltonian. Here, we give a qualitative description based on the investigation of the numerical average Hamiltonian. According to Eq. (3.25) and (3.26), not only the off-diagonal J_{HL}

terms are adjustable, but also the diagonal terms could be tuned by $\hat{I}_{1z} - \hat{L}_z$ and $\hat{I}_{2z}(\hat{I}_{1z} - \hat{L}_z)$ in the higher order Magnus expansions, therefore more complicated quantum dynamics arises. The periodic zero points in Fig. 3.9 are caused by two different reasons. One is that the two 3×3 submatrices are almost the same, therefore the transfer from spin-up to spin-down in the first subspace cancels out the transfer from spin-down to spin-up in the second subspace, which accounts for the sharp zero crossings. However, the generation of the curly zero crossings is because in each subspace there is almost no interaction between the spin-up state α_L and the spin-down state β_L , i.e., the effective $J_{HL} \sim 0$ in the off-diagonal elements. Between any two adjacent zeros, there exists a maximum polarization.

This high offset field has practical significance. As noted previously, the hyperpolarization of SABRE-SHEATH is generated in a solenoid coil sitting in a metal shelter, where the earth field is shielded by the mu-metal, and a ultra-low field is provided by the coil. If a high offset field works as well, the lab field ($\sim 30\mu T$) could directly work as the offset field. Fig. 3.17 depicts how the final polarization varies with the period of a sine wave with the offset being fixed at $30\mu T$ and the sine wave amplitude being maintained at $50\mu T$. By modulating the pulse period, we can easily figure out the optimum condition. Modulation of the pulse amplitude works equivalently. A ramp pulse with fixed pulse period ($T = 20ms$) and pulse amplitude ($B = 50\mu T$) is applied to experimentally verify the validity of the high-offset oscillating pulse SABRE (Fig. 3.18). The polarization undergoes a periodic change from 5% to -5% as the offset is

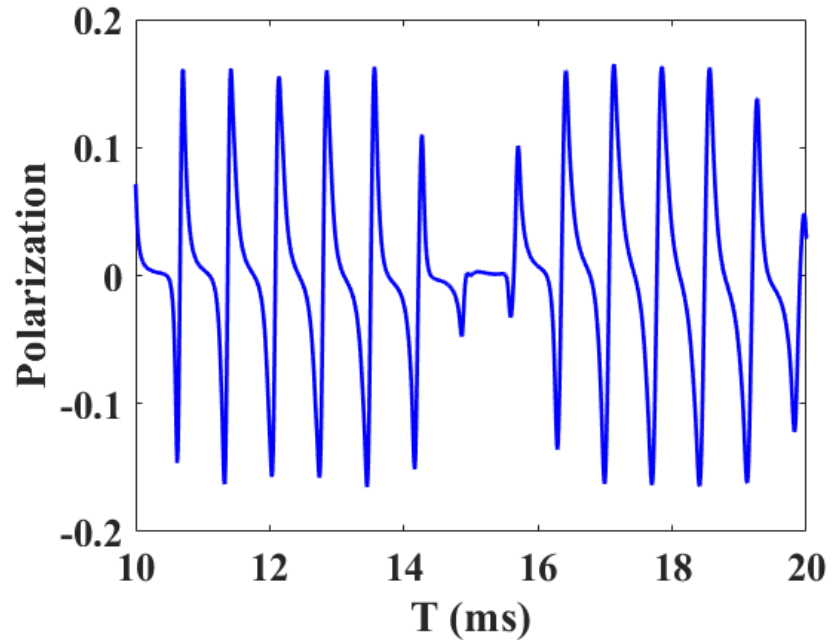


Figure 3.17: A depiction of how the final polarization varies with the period of a sine wave sequence. This sine wave has unchanged amplitude $B = 50\mu T$, and the offset is maintained at $B_0 = 30\mu T$.

scanned, even when the offset is larger than $5\mu T$. The numerical prediction (Fig. 3.18(a)) is perfectly confirmed by the experimental results (dotted line in Fig. 3.18(b)).

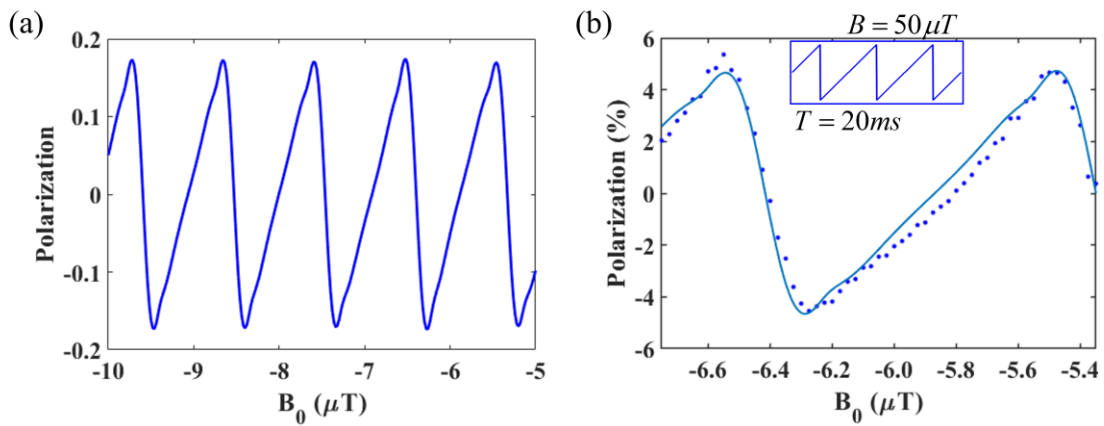


Figure 3.18: (a) A numerical simulation result shows that the polarization varies periodically with the offset field. (b) An experimental confirmation of (a).

Consider a special case that the offset field is equal to the amplitude of a square pulse, so the overall magnetic field is a unidirectional oscillating square pulse (Fig. 3.19), which we call a two-state square pulse. Similarly, the maximum polarization of this pulse could be searched by tuning the pulse period or pulse amplitude. Shannon's work⁷⁷ studied this two-state square pulse and used a different theoretical strategy, which is the Taylor series expansion of the solution of the Liouville von Neumann equation, to understand the generation of enhanced SABER signal. In addition, this signal enhancement was verified

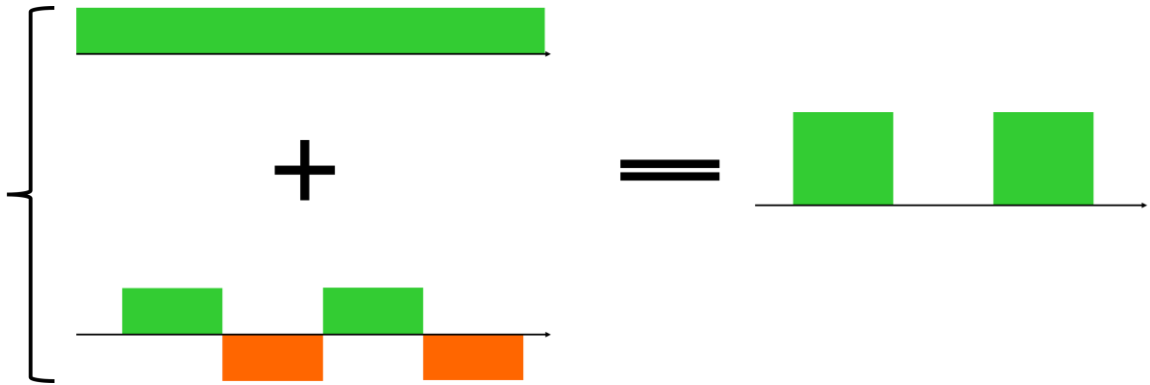


Figure 3.19: A combination of square pulse and a constant field which have identical amplitude yields a unidirectional oscillating square pulse.

by experiment (Fig. 3.20). Fig 3.20 (a) depicts a two-state square pulse with the length of the first and the second state being 3ms and 13.5ms. The signal strength varies periodically with the amplitude of the square (green lines in Fig. 3.20(c)). The vertical black dotted lines indicate the zero crossings caused by vanished effective J_{HL} . Base on Eq. (3.19), when the rotation angle of each square is $2\theta = \Delta\omega \times \tau = 2\pi$, the M and N in the off-diagonal goes to zero simultaneously. Fig. 3.20 (b) is a variant of the two-state

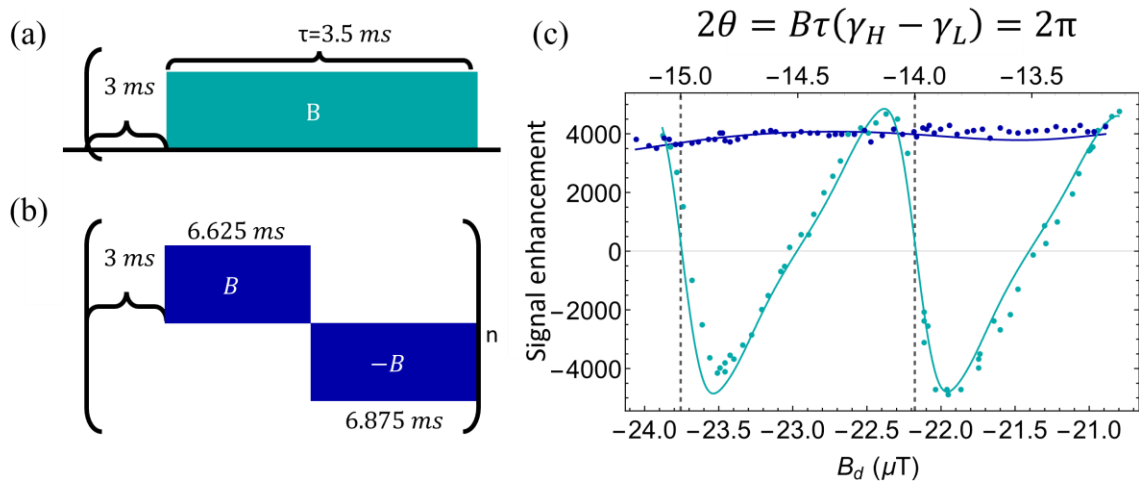


Figure 3.20: (a) A two-state square pulse. (b) A variant of two-state square pulse which loses the axial symmetry. (c) Experimental verification of signal enhancement. The green dotted line is the experimental data of the two-state pulse, while the blue dotted line refers to the variant pulse. The solid curves are the corresponding fittings. Image courtesy of S. Eriksson, et al., *Sci. Adv.* 8, 11, (2022).

pulse which is no longer axisymmetric. According to the previous theoretical analysis, this pulse is robust to the pulse amplitude and the pulse period like the ramp pulse, which is also demonstrated experimentally (blue lines in Fig. 3.20 (c)). As the pulse magnitude changes from $-24\mu\text{T}$ to $-21\mu\text{T}$, the signal always stays at the maximum. We emphasized earlier that with same symmetry the pulse shape does not make essential differences, which is supported by a positive sine wave (Fig. 3.21 (a)) and a positive triangle pulse (Fig. 3.21 (b)) without an offset field. However, in the presence of an arbitrary offset or an arbitrary free evolution interlacing with the pulse, the final polarization has similar features.

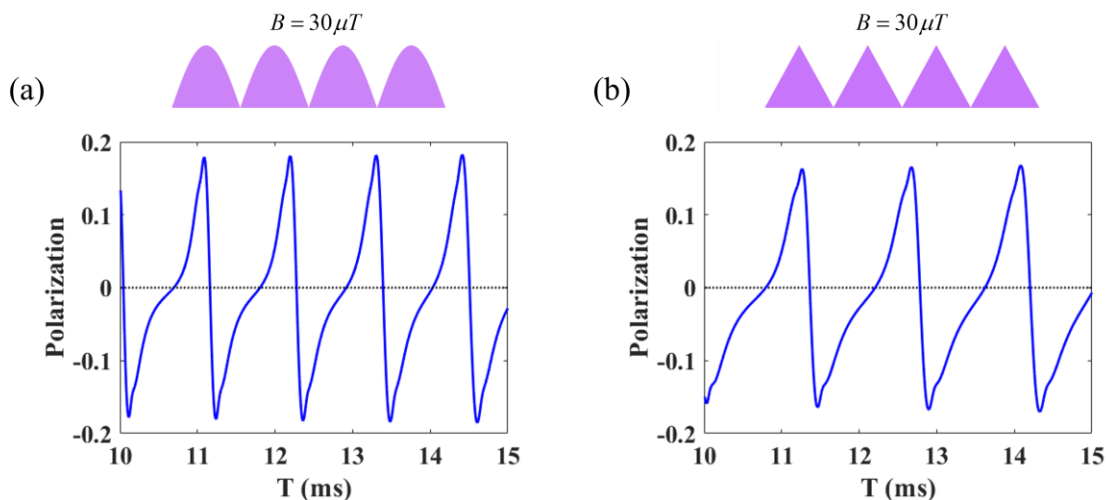


Figure 3.21: Polarization varies as the pulse period of a (a) unidirectional sine wave and (b) a unidirectional triangle wave. The offset of both cases is zero.

3.6 Conclusion and Outlook

We have shown, in both experiments and simulations, that a variety of oscillating magnetic fields can significantly improve SABRE-SHEATH hyperpolarization. In effect, the interaction between hydrides and target nuclei are adjustable by tuning the pulse amplitude, pulse period, and the offset. As described above, we improve the robustness to experimental imperfections by exploring different pulse shapes. Finally, it turns out that a pulse shape without an axial symmetry, such as a ramp wave, generates significant improvements in achievable polarization and is robust to experimental imperfections. In the last part, we show that this oscillating pulse SABRE could be expanded to any pulse shape. By correctly adjusting either the pulse period, pulse amplitude, or the offset field, one can easily obtain the maximum polarization.

In this work, the largest polarization yielded with 43% parahydrogen is $\sim 5.3\%$; this would correspond to 22% polarization with 100% parahydrogen. In our simulations,

the maximum polarization generated by SABRE-SHEATH method is as high as 60% using 100% parahydrogen. This gap between principle and reality indicates that SABRE retains room for improvement. Since this oscillating pulse in z-direction is not able to generate 100% polarization even in an ideal situation, recently, our group members are studying pulse sequences in an arbitrary direction, which has been numerically demonstrated to further enhance the polarization.

Chapter 4: High-pressure SABRE

In the previous chapter, we improved the effectiveness of SABRE from the perspective of quantum dynamics. However, SABRE includes many other complicated processes. For example, the dihydrogen inflow and outflow processes and its chemical exchange rate also play a crucial role. In this chapter, we study how the parahydrogen supply impacts the SABRE signal. This supply and loss are related to two factors. One is the exchange rate of the dihydride, which determines over what period of time the bound dihydride will be replaced by dihydrogen; and the other is the dihydrogen inflow and outflow process, which determines the stable ratio of the fresh dihydrogen to the used dihydrogen in the SABRE solution during the bubbling process.

With the exchange rate of the substrate being fixed, increasing the exchange rate of the dihydride could increase the final polarization a lot. Fig. 3.1 displays the maximum SABRE signal as a function of the exchange rate of both the dihydride k_H and the substrate k_L . Since the hydride cannot exchange faster than the substrate $k_H \leq k_L$, reducing the difference between them enhances the SABRE signal. However, in the simulation we assume that the dissociated dihydrogen was immediately blown out and would not rebind to the catalyst for recycling, which is an ideal case. When the rate of both the incoming and outgoing dihydrogen is low, the replacement of used parahydrogen with fresh parahydrogen is hindered and slowed down. It is evident that the rebinding of used dihydrogen will diminish the polarization efficiency. Fig. 3.2(a) depicts that the polarization efficiency decreases as the increased probability of dihydrogen

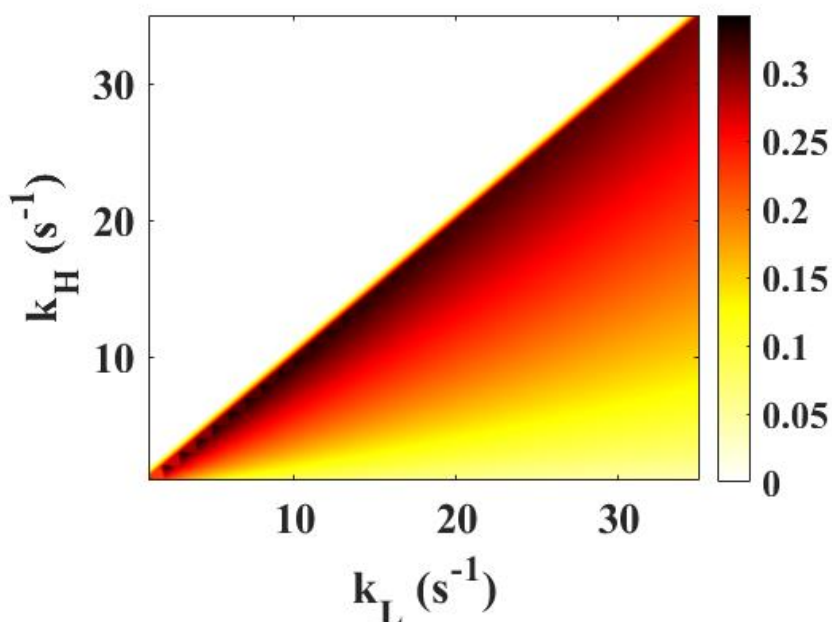


Figure 4.1: Maximum polarization as a function of both k_H and k_L (simulation parameters are the same as Fig. 3.9)

rebinding. Fortunately, in our SABRE experiment this is an easily solved problem by increasing the bubbling speed, because at room temperature and low pressure the solubility of hydrogen in the SABRE solvent methanol is relatively low so that the amount of dissolved hydrogen is consequently low. Fig. 4.2(b) shows that in our SABER experiment rebinding of dihydrogen is negligible provided the gas flow rate is higher than 80 milliliters per minute, since keeping raising the flow rate does not boost the signal further. Based on these facts, increasing the exchange rate of the dihydride is a significant factor to enhance the SABRE signal. Prior thermal experimental investigations⁸⁷ have altered the exchange rates within the SABRE system by manipulating its temperature. However, this thermal study does not improve the efficiency of SABRE, because both the exchange rate J_{HH} and J_{HL} are altered with

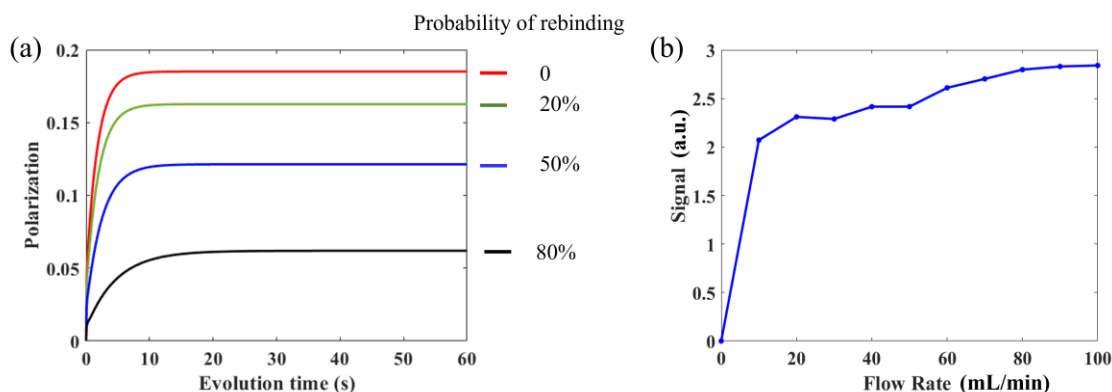


Figure 4.2: (a) SABRE signal decreases as the increased probability of dihydrogen rebinding. (b) SABRE signal varies with the flow rate of hydrogen gas

temperature. What is needed is to alter the exchange rate of the dihydride while keeping the exchange rate of the substrate almost uninfluenced. This is how the idea of high-pressure SABRE came about.

4.1 Ways to Improve the Accessibility of Dihydrogen

The solubility of hydrogen gas in methanol at room temperature ($\sim 25^\circ\text{C}$) and 1 atm pressure is approximately 0.017 g/L ⁸⁸. According to Henry's law⁸⁹⁻⁹¹, at a constant temperature, the concentration of a gas in a liquid is directly proportional to the partial pressure of that gas above the liquid. Mathematically, Henry's law can be expressed as:

$$C = k_H \times P, \quad (4.1)$$

where C is the concentration of the gas in the liquid, P is the partial pressure of the gas above the liquid, and k_H is the Henry's law constant, which is specific to each gas-liquid system and depends on factors such as temperature and the nature of the gas and liquid molecules. In traditional SABRE, the gas pressure is usually 7 bar, therefore, the solubility of hydrogen in methanol at room temperature is around 26.2mM. Since the

concentration of SABRE complex is around 4.4 mM, in average, six hydrogen molecules are sitting around one SABRE complex, and this low concentration leads to a low exchange rate of the dihydride which is generally less than $10s^{-1}$. The most straightforward way to substantially improve the accessibility of dissolved hydrogen is increasing the gas pressure. For example, at 200 bar and room temperature, the concentration of dissolved dihydrogen is increased to 748.6 mM as a result, and each SABRE complex is surrounded by 170 dihydrogen in average.

Another method to increase the concentration of dihydrogen is generating a supercritical SABRE sample instead of a liquid one such that it is miscible with hydrogen gas. A supercritical fluid⁹²⁻⁹⁶ is a substance that is at a temperature and pressure above its critical point, where it exhibits properties of both a liquid and a gas. At this point, the substance is in a state that is intermediate between a gas and a liquid. Supercritical fluids have a density that is similar to a liquid, but they also have the ability to diffuse through materials like gas. They also have the ability to dissolve materials like a liquid, but their solvating power can be adjusted by changing the temperature and pressure⁹⁷. For example, Fig. 4.3 is the phase diagram of CO₂⁹⁸ which shows the different phases of CO₂ (solid, liquid, and gas) and the conditions under which they exist, based on temperature and pressure. The top right corner of the diagram beyond the critical point represents the region where CO₂ is a supercritical fluid. In this situation of supercritical, the solvent used in SABRE must meet both the requirements that (1) it is able to dissolve the SABRE complex as well as the substrates, and (2) it has accessible critical parameters. Methanol and ethanol are most commonly used solvents because they have a

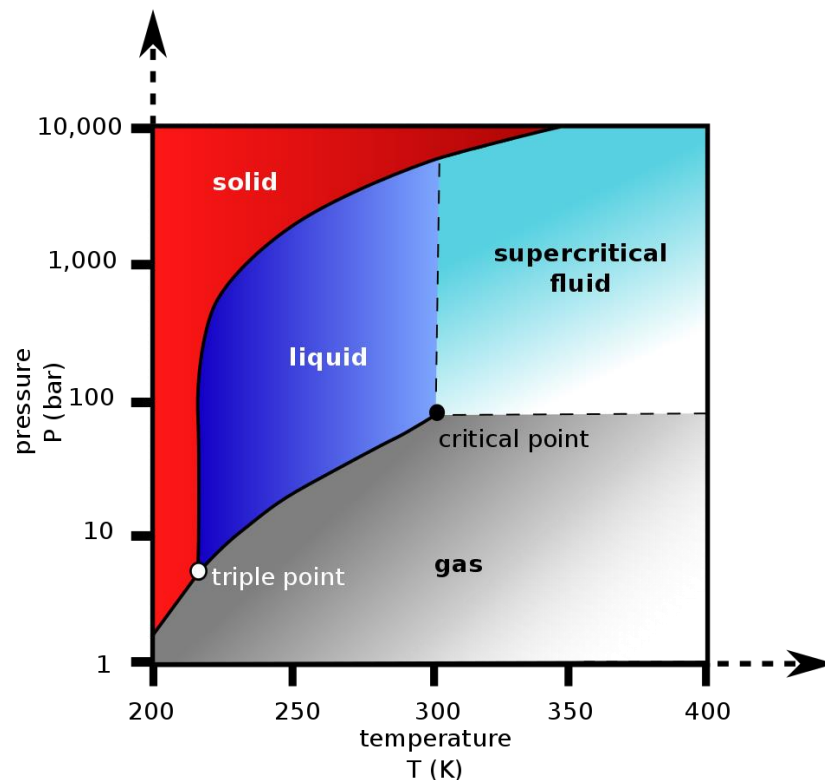


Figure 4.3: Carbon dioxide pressure-temperature phase diagram. Image credit: B. Finney and M. Jacobs, Wikipedia⁹⁹.

relatively high solubility for both the SABRE catalyst and hydrogen gas. However, their critical temperature is not easy to access. Table 3.1 list the critical temperature and critical pressure of some commonly used solvents^{100, 101}, which shows that only carbon dioxide and xenon have accessible critical parameters. Xenon is a prohibitively expensive inert gas, so carbon dioxide is the most suitable supercritical solvent. Additionally, there are many other advantages to using CO₂ as a solvent. CO₂ is a naturally occurring gas and is non-toxic, non-flammable, and non-corrosive. It is an environmentally friendly solvent. CO₂ can dissolve both polar and non-polar compounds, making it a versatile solvent for a wide range of applications. The solubility of a compound in CO₂ can be easily controlled

Table 4.1: Critical parameters of some commonly used solvents

Substance	Critical Temperature (K)	Critical Pressure (bar)
Carbon dioxide	304	74
Water	647	221
Ammonia	406	114
Xenon	290	58
Methanol	513	81
Ethanol	514	61
Acetone	508	47
Acetonitrile	546	48
Acetic acid	596	58
Benzene	562	49
Toluene	592	41

by adjusting the temperature and pressure, allowing for selective extraction of specific compounds^{102, 103}. Assuming we use a gas mixture of 20% hydrogen and 80% CO₂ at 200 bars to run a SABRE experiment, the concentration of hydrogen gas is around 1.8M. A gas mixer is used to premix H₂ and CO₂ in a supercritical SABRE experiment, otherwise H₂ is loaded to the primer pump directly. This primer pump is unidirectional, so the incoming gas cannot flow back. The downstream gas in the system could be pressurized to some value between 50 bars and 100 bars by the primer pump as needed. Then the syringe pump right after the primer pump slowly and accurately pumps the gas pressure

in the sample tube to the required value (usually in the range from 150 bars to 400 bars) (Fig. 4.4). The conventional sample tube made of glass utilized in SABRE, which permits the bubbling of gas through the solution, is limited to a maximum gas pressure of less than 10 bar. Instead, we use a high-pressure tube constructed from zirconia to sustain pressure reaching up to 1000 bar.

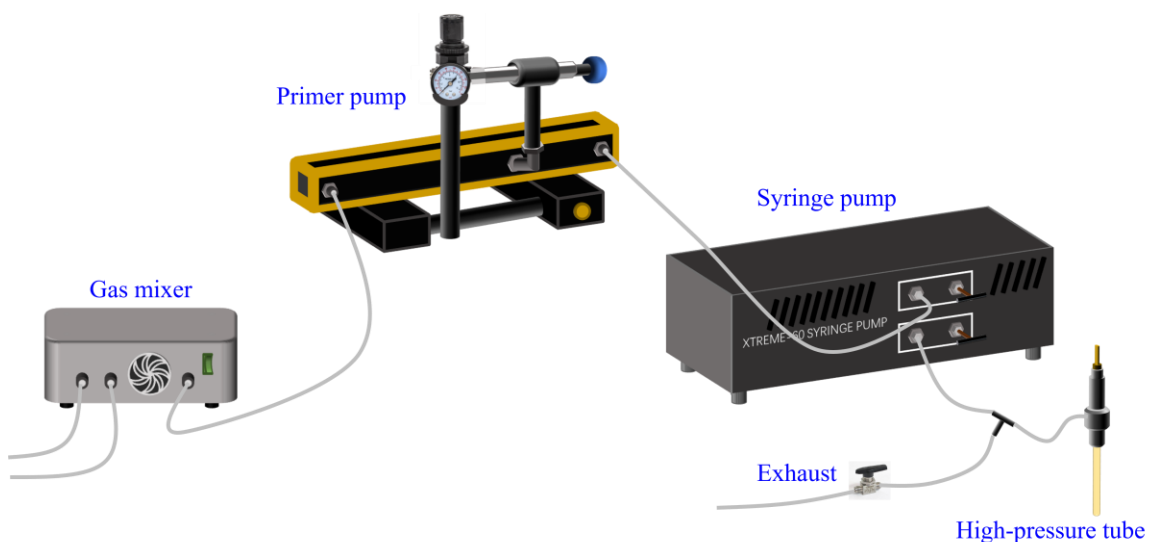


Figure 4.4: High-pressure system setup, which is composed of a gas mixture, a primer pump, a syringe pump, and a high-pressure sample tube.

Unlike the glass sample tube, this high-pressure tube does not allow bubbling of gas through the sample, therefore, after being pressurized the whole sample and the gas in the remaining space are sealed in the tube. Consequently, in the case of brute-force high-pressure SABRE, there exists an extremely low exchange between the dissolved dihydrogen and the hydrogen gas above the solution due to the permeability of the hydrogen gas in the SABRE solution. While, in the case of supercritical SABRE, there is no such exchange at all. Based on our previous analysis, no or little in-flow and out-flow

of the hydrogen gas causes recycling of the dihydrogen and then diminishes the SABRE signal. However, if the concentration of the dissolved hydrogen is way larger than that of the SABRE complex, only an extremely small fraction of the dihydrogen would be consumed during the signal build-up period of SABRE (which is usually less than 60s), and the rebinding probability could be maintained at a markedly low point (Fig. 4.5). Therefore, the master equation of the SABRE system (Eq. (2.40), (2.41)) requires some modifications. The conversion between parahydrogen and orthohydrogen is still ignored, and the in-flow and out-flow rate of hydrogen is assumed to be zero. While, recycling of the dihydrogen must be considered, and the corresponding differential equation of the density matrix of the hydrogen ensemble is

$$\partial_t \hat{\rho}_H = \frac{[C]}{[H]} \tilde{k}_H \left(\text{Tr}_{\{H\}}(\hat{\rho}_C) - \hat{\rho}_H \right), \quad (4.2)$$

where, $[H]$ is the concentration of the dissolved dihydrogen, and $\tilde{k}_H = k_H \exp\left(-\frac{k_H \Delta t}{2}\right)$ is the modified exchange rate of the dihydride. Based on the new master equation, we could simulate the polarization build-up process of the high-pressure SABRE (Fig. 4.6). In Fig. 4.6(a) we compare the traditional SABRE-SHEATH (red curve) and the high-pressure SABRE-SHEATH (blue curve), which share the same simulation parameters except that the $\frac{[C]}{[H]} = \frac{1}{1000}$ in the high-pressure case while each dissociated dihydrogen is immediately replaced by an unused molecule in the conventional SABRE case. In the

first ten seconds these two cases have the same signal build-up trajectory. As the consumption of hydrogen increases, the resultant signal experiences a decrease in

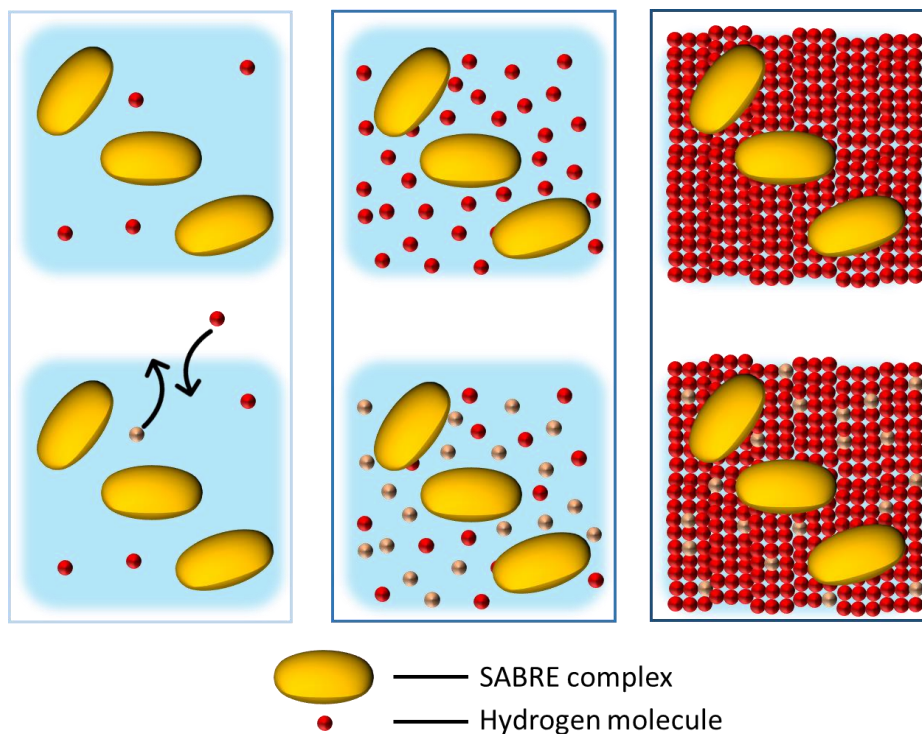


Figure 4.5: The left column refers to the traditional bubbling SABRE, in which the concentration of the dissolved hydrogen is very low, but the supplement of fresh gas is ongoing. However, in closed SABRE systems (middle and right columns) hydrogen gas is being increasingly consumed, and recycling of hydrogen is inevitable. When the concentration of the hydrogen gas is extremely higher than the concentration of the SABRE complex, the consumption of hydrogen gas becomes very slow, and recycling will not constitute a cause for concern (the right column).

magnitude. Then high-pressure case starts to fall behind the traditional case and lose polarization after ~23s. In this comparison, we assume both the cases have the same exchange rate of the dihydride. Consequently, the traditional case is in an ideal condition, which has no hydrogen recycling, and outperforms the high-pressure case without question. However, the increased concentration of hydrogen leads to a faster chemical

exchange rate¹⁰⁴⁻¹⁰⁶. By assuming that the dihydride exchanges as fast as the substrate, we depict the signal build-up curve (black line in Fig 4.6(b)), which agrees with our previous analysis (Fig. 4.1) that a faster exchange rate of the dihydride yields a higher polarization. Here, the enhancement is more than 3 times. The signal build-up time of the high-pressure SABRE is as short as 5s, and subsequently, there was a rapid decline in polarization in that the faster exchange causing a faster consumption of parahydrogen. The positive results obtained from the analysis warrant further investigation through experimental confirmation.

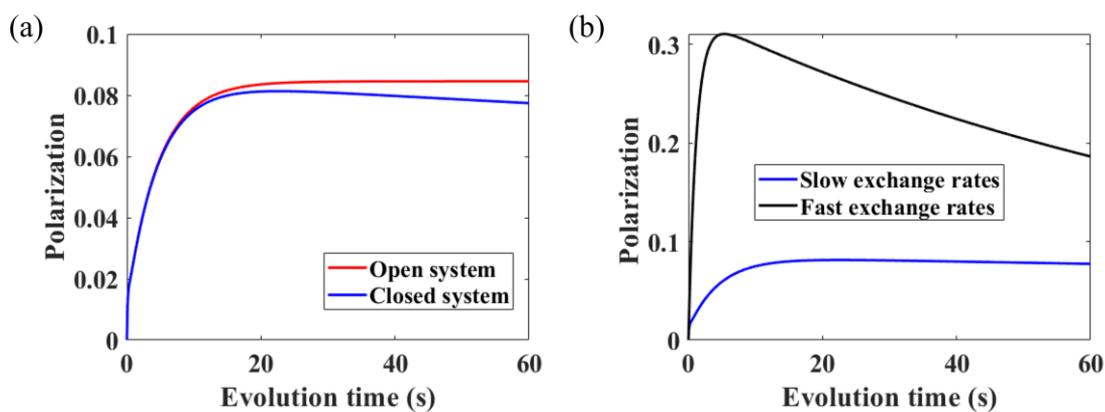


Figure 4.6: (a) Contrast an open SABRE system that permits the inflow and outflow of hydrogen gas with a closed SABRE system that does not allow an exchange of hydrogen gas. (b) Analyze the polarization build-up mechanisms in a SABRE system with a high rate of dihydride exchange, in comparison to the same system with a low rate of dihydride exchange.

4.2 Experimental Results of Brute-force High-pressure SABRE

As the name implies, the Brute-force high-pressure method straightforwardly increases the hydrogen gas pressure. The SABRE solution we prepare is the same as the one used in the last chapter which is composed of 2 μ L ¹⁵N-acetonitrile (50mM), 1 μ L natural abundance ¹⁴N-pyridine (25mM), 1.3mg the catalyst precursor

[IrCl(COD)(IMes)] (4.4mM), and 500 μ L deuterated methanol solvent. 43% parahydrogen is first loaded into the high-pressure tube and pressurized to ~200 bar to activate the catalyst. To complete the activation process, it is recommended to shake the tube a few times and maintain the high-pressure gas in the tube for at least 30 minutes. Subsequently, the gas can be slowly depressurized to several bars (which usually takes 45 minutes) using the syringe pump, and the consumed parahydrogen can be exhausted. The sample is now activated and ready for the SABRE-SHEATH experiment. Following this step, fresh parahydrogen can be repump into the high-pressure tube, which typically takes 10 minutes. The target substrate can be hyperpolarized by placing the tube in an appropriate magnetic field within the metal shield (as shown in Fig. 3.8). Immediately prior to inserting the tube into the shield, it is advisable to vigorously agitate the tube several times. This promotes the displacement of the parahydrogen gas that has been consumed in the solution with fresh gas that is present above the liquid. Finally, the tube can be transferred to a magnetometer for signal detection, and the transfer time is typically around 20 seconds.

To investigate whether there are any chemical differences between the low-pressure and high-pressure cases in SABRE, the thermal proton spectra of the high-pressure SABRE sample was detected. The purpose of this is to compare the chemical characteristics of the SABRE sample at high pressures and determine if there are any noticeable changes or alterations in its chemical composition. The proton spectrum of a sample comprising high-pressure hydrogen, substrates, and the solvent methanol, in the absence of the IMes catalyst, is depicted in Fig. 4.7 (a). The proton spectrum of pyridine

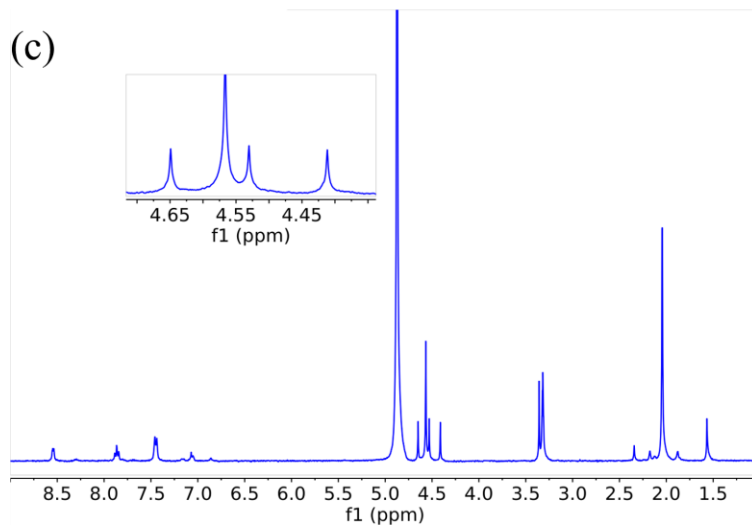
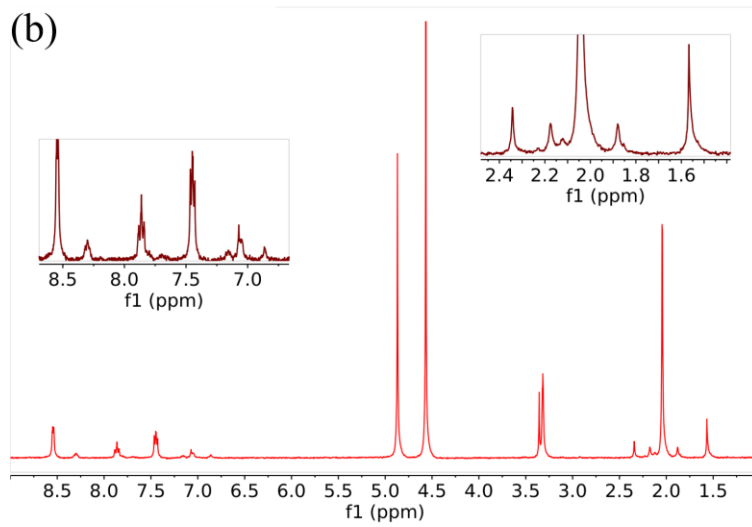
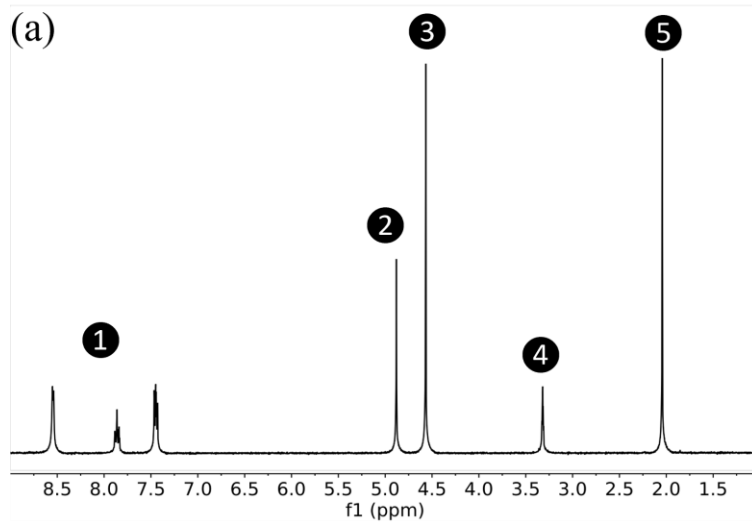


Figure 4.7: (a) Proton spectrum of a solution consisting of high-pressure hydrogen gas, substrates (pyridine and acetonitrile), and deuterated methanol as the solvent. (b) Proton spectrum of a high-pressure SABRE solution which is composed of the same sample in (a) with presence of SABRE catalyst IMes. (c) Proton spectrum of the identical sample as in (b) subsequent to being hermetically sealed for a prolonged duration (a couple of hours).

exhibits distinct peaks at three different positions, which are labeled as peak ①. Peak ② corresponding to the undeuterated hydroxyl group (-OH) of methanol or any remaining water present in the solvent. Peak ③ is attributed to the presence of dissolved hydrogen gas in the sample. Peak ④ is assigned to the undeuterated methyl group (-CH₃) of methanol. Finally, peak ⑤ is associated with the methyl group of acetonitrile. Upon addition of the SABRE catalyst to the sample and subsequent activation, the substrates pyridine and acetonitrile bind to the metal center of the catalyst. This binding interaction results in the appearance of small peaks in the proton spectrum corresponding to the extra bound species, as depicted in Fig. 4.7(b).

After prolonged sealing of the sample at high pressure within the tube, alterations are observed in the peaks of the hydroxyl group and the hydrogen gas. Specifically, the peak associated with the hydroxyl group exhibits significant growth, whereas the peak corresponding to the hydrogen gas experiences substantial shrinkage. Additionally, three peaks, which are equidistant, emerge near the hydrogen gas peak. Based on the observed chemical shift in close proximity to the hydrogen gas, as well as the splitting pattern caused by a coupling of approximately 42Hz, it can be inferred that the three additional peaks correspond to the presence of HD. This molecule is an isomer of dihydrogen, with one of its hydrogen atoms replaced by a deuterium atom. The presence of deuterium can

only be attributed to the deuterated methanol used in the experiment. This suggests that during the dissociation and association process of exchangeable substrates, methanol molecules briefly bind to the catalyst center and exchange their deuterium atoms in the hydroxyl group with the dihydride, as shown in Fig. 4.8(a). Furthermore, this observation accounts for the increase in intensity of the hydroxyl group peak in the spectrum. Nonetheless, this exchange mechanism causes a perturbation in the correlation between the two hydride species, leading to the destruction of their singlet state. Moreover, it is noteworthy that the rate of this exchange reaction exhibits an upward trend with increasing pressure, posing further challenges for accurate characterization of the SABRE system. Fig. 4.8(b) illustrates the bound species of the dihydrogen, which exhibits

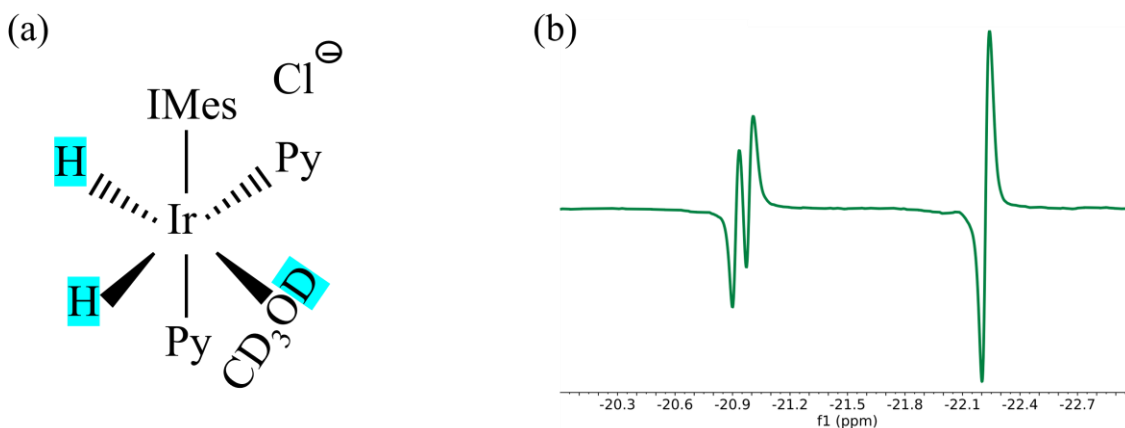


Figure 4.8: (a) Deuterated methanol molecule shortly binds to the catalyst center and exchanges its deuterium atom with one of the dihydride. (b) Hydride signal of the high-pressure SABRE system.

chemical inequivalence of the two hydrides due to the presence of two different horizontal ligands, namely, pyridine and acetonitrile. Specifically, the antiphase peak on

the right side corresponds to the hydride nucleus that forms a bond perpendicular to the acetonitrile ligand, while the antiphase doublet peak on the left side represents the hydride nucleus that forms a bond parallel to the ligand. The splitting of this doublet peak arises from the coupling between the hydride and the ^{15}N nucleus in the substrate ligand. The detection of the hyperpolarized hydride signal is a reliable indicator of successful hyperpolarization by SABRE, as it confirms the existence of hydride and its exchange process within the sample.

Through the manipulation of gas pressure, an investigation was conducted to examine the relationship between the signal of SABRE and the pressure of hydrogen gas. Specifically, Fig. 4.9(a) presents a stacked display of the SABRE signal across a range of pressures spanning from 10 bar to 400 bar, while Fig. 4.9(b) depicts the specific polarization value as a function of the hydrogen gas pressure. The findings of the present investigation support the existence of a positive relationship between enhanced solubility of hydrogen and amplification of SABRE signal, as long as the gas pressure remains below 300 bar (which corresponds to a concentration of dissolved hydrogen gas of approximately 1.15M). However, when the pressure exceeds this threshold, the signal exhibits a decrease, which suggests that a surplus of hydrogen gas can have an adverse impact on the polarization efficiency. This might be because that an excessive concentration of hydrogen gas within the SABRE system can cause the SABER complex to break down. The excess hydrogen gas can compete with the substrate for binding to the metal catalyst, leading to the formation of a different complex that is no longer capable of enhancing the NMR signal. Additionally, the excess hydrogen gas can cause

the SABRE complex to become unstable, leading to its decomposition and loss of activity. The application of the high-pressure SABRE method resulted in a maximum polarization of approximately 5.9%, surpassing the maximum polarization of 1.7%

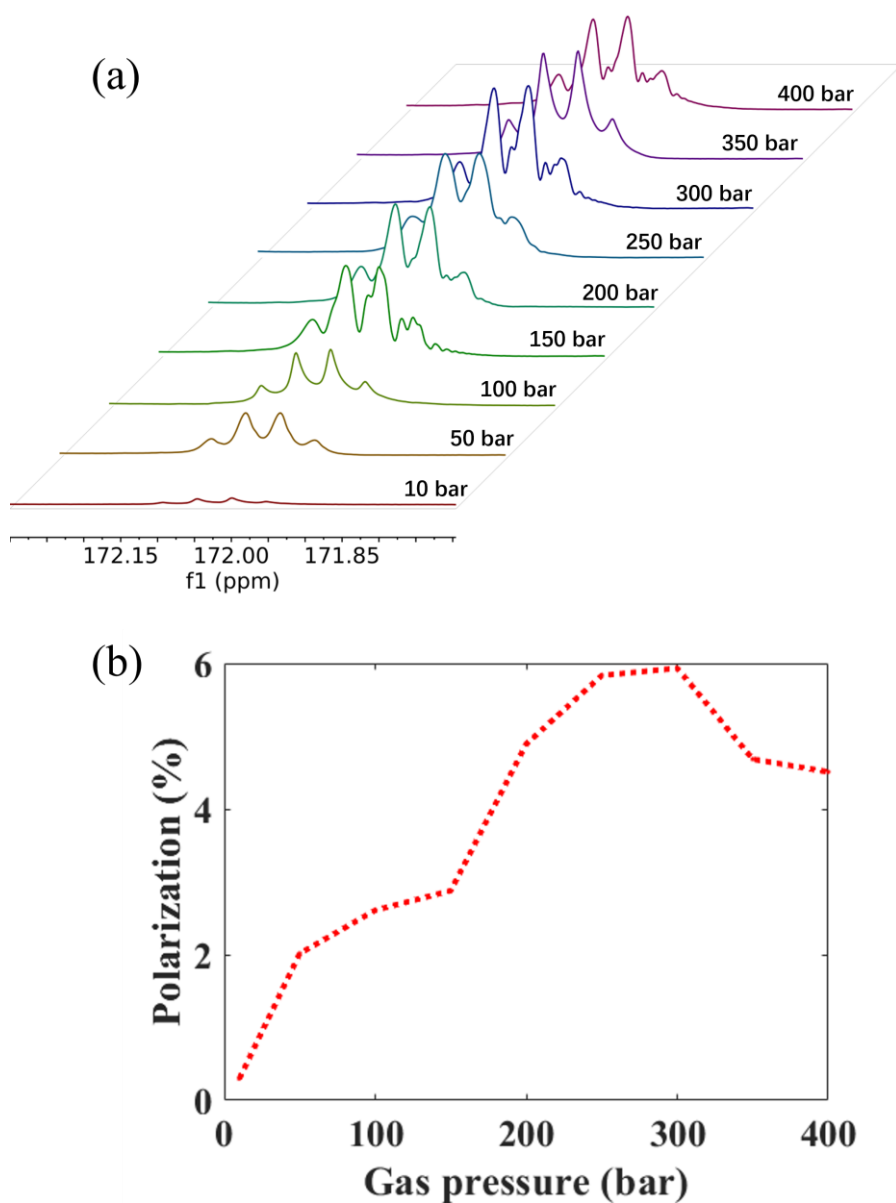


Figure 4.9: (a) A stacked display of the SABRE signal across a range of pressures spanning from 10 bar to 400 bar. (b) A depiction of the polarization value at each specific gas pressure.

achieved using the conventional SABRE-SHEATH method by more than threefold. Hence, it can be concluded that the high-pressure SABRE method represents a significant advancement over the conventional methodology.

4.3 Experimental Results of Super-critical SABRE

Another approach involves the generation of a supercritical solution of SABRE utilizing CO₂ as the supercritical solvent. In this context, the experimental protocol utilized was as follows: (1) introduction of the SABRE complex and substrates into the sample tube; (2) injection of a gas mixture of 80% CO₂ and 20% H₂ into the tube, which was subsequently pressurized to 200 bar and agitated to produce a homogenous solution; (3) sealing of the sample and allowing it to remain in this state for a minimum 30 minutes to fully activate the SABRE complex; (4) immersion of the sample tube into liquid nitrogen to freeze all components, except for the hydrogen gas; (5) release of the hydrogen gas, followed by warming of the sample to room temperature; (6) subsequent introduction of fresh hydrogen gas and pressurization to 200 bar, along with vigorous shaking to achieve a uniform solution; (7) immediate transfer of the sealed sample tube into an electrified solenoid coil (the place where polarization takes place) immersed in a hot bath to regulate the sample's temperature; (8) after exposure to the low magnetic field for a designated period, transfer of the sample for signal detection. The activated SABRE sample is reusable by repeating the procedures outlined in steps (4) to (8). It is noteworthy that the critical parameter of a mixture differs from that of its individual components and is contingent upon the weight of each component¹⁰⁷⁻¹¹¹. Hence, the gas mixture CO₂ and H₂ has distinct critical parameters in comparison to its constituents.

Specifically, at room temperature, when subjected to 200 bar pressure, a mixture of 80% CO₂ and 20% H₂ reaches a supercritical state.

In this study, we conducted an experiment using the same SABRE catalyst (IMes) and substrates (pyridine and acetonitrile) as previously mentioned. The corresponding proton spectrum of the sample is presented in Fig. 4.10. The three small peaks on the left correspond to the free species of pyridine. The strong peak in the middle indicates the

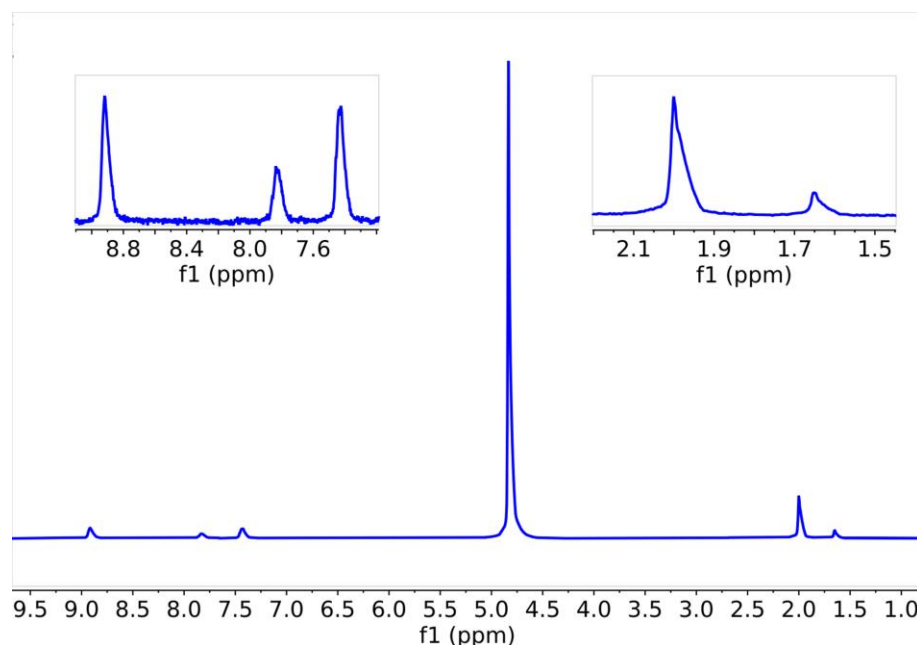


Figure 4.10: Proton spectrum obtained from a super-critical SABRE sample, which was prepared by mixing 1 μ L pyridine, 2 μ L 15N-acetonitrile, and 1 mg of IMes catalyst in the high-pressure sample tube with a volume of approximately 1 mL. The tube was then filled with a gas mixture of 20% H₂ and 80% CO₂ at a pressure of 200 bar.

hydrogen gas. On the right side, the higher peak corresponds to the free species of acetonitrile, while the lower peak represents the bound species. Interestingly, we did not observe any evidence of the presence of the bound species of pyridine, and no hydride signal was detected either. Moreover, a SABRE-SHEATH experiment using this sample

generated only a tiny polarization signal, which suggests that the sample is not suitable for SABRE. An alternative sample was then examined, wherein the solvent (CO_2) remained constant, while a phosphorus catalyst was introduced instead (illustrated in Fig. 4.11(a)). Only one substrate, acetonitrile, was employed, and no co-ligand substrate was required. The corresponding proton spectrum was exhibited in Fig. 4.11(b), wherein

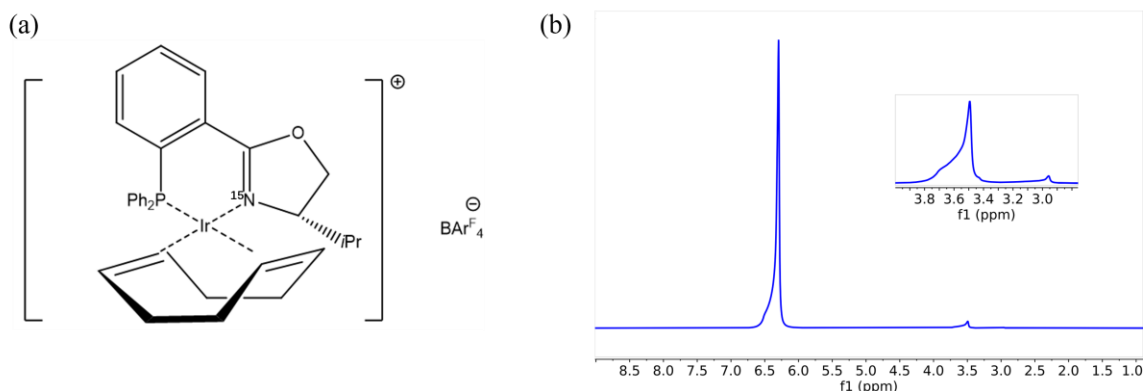


Figure 4.11: (a) Molecular diagram of the phosphorous catalyst. (b) Proton spectrum of the new supercritical SABRE sample which consists of 1 mg phosphorus catalyst, 2 μL acetonitrile, and a mixture of 20% H_2 and 80% CO_2 .

the protons present in the hydrogen gas as well as both the free and bound species of acetonitrile was detected. Encouragingly, despite the low signal to noise ratio, the hyperpolarized hydride signal linked to the phosphorus catalyst was successfully detected, as shown in Fig. 4.12(a). Additionally, as the two hydrides were chemically inequivalent, they exhibited different chemical shifts. Each peak's triplet splitting arose from the coupling of each hydride with both a ^{15}N and a ^{31}P . The configuration of this SABRE complex is displayed in Fig. 4.12(b), which is a 6-spin system comprising two hydrides, one ^{15}N in the vertical ligand of acetonitrile, one ^{15}N in the horizontal ligand of acetonitrile, as well as one ^{15}N and one ^{31}P in the catalyst itself.

Subsequently, we sought to optimize the degree of polarization by systematically varying several key parameters, specifically, the temperature of the hot bath, the duration of exposure to the low magnetic field (also called evolution time), and the strength of the low magnetic field. The temperature of the hot bath plays a crucial role in modulating the

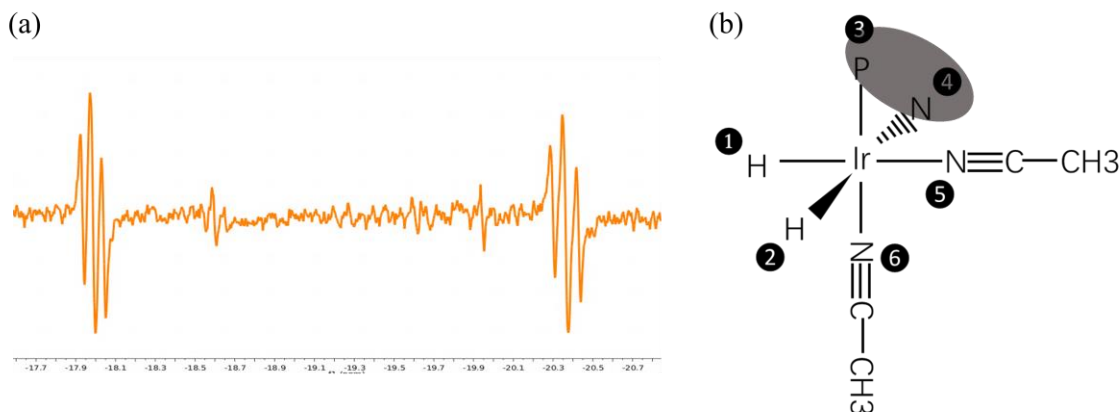


Figure 4.12: (a) Hyperpolarized hydride signal of the new SABRE system previously described in Fig. 4.11. (b) The configuration of the SABRE complex.

chemical exchange rates of both the dihydride and the exchangeable ligands. Additionally, the duration of exposure to the magnetic field is carefully chosen to ensure that the spin order transfer is stopped at the time that the system reaches the maximum achievable polarization level. Lastly, the offset field is manipulated to optimize the quantum dynamics of the spin order transfer process. Figure 4.13 presents a graphical representation of the experimental data. The sample utilized in the experiments is previously mentioned in Figure 4.10. Subfigure (a) of Fig. 4.13 illustrates the variation of the temperature of the hot bath, ranging from 40°C to 100°C while maintaining the evolution time at 30s and the magnetic field at 0.6μT. The result suggests that the optimal temperature for the hot bath is approximately 70°C. Subfigure (b) demonstrates the effect

of evolution time on the experiment, ranging from 15s to 75s while fixing the hot bath temperature at 65°C and the magnetic field at 0.6μT. The data indicates that the optimal

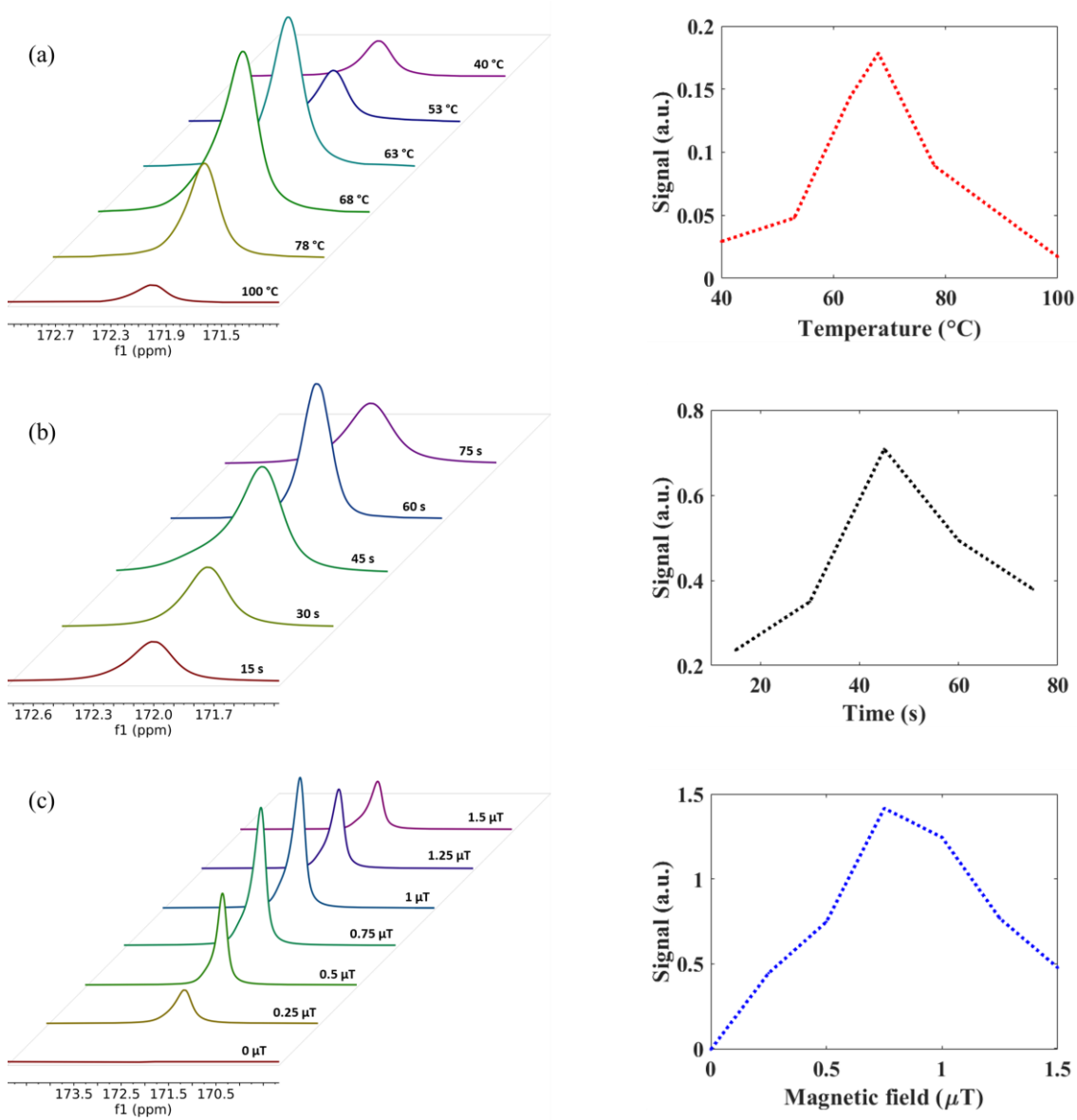


Figure 4.13: Illustration of the polarization of the supercritical SABRE changes with (a) temperature, (b) exposure time in the low field, and (c) magnitude of the low field.

evolution time is approximately 45s. Subfigure (c) depicts the variation in the magnetic field while holding the hot bath temperature at 65°C and the evolution time at 45s, and the data suggests that the optimal magnetic field is approximately 0.75μT.

Despite optimization of the three parameters, the maximum signal obtained (~1.5%) falls short of the conventional SABRE-SHEATH method (~1.7%). Even though the experimental method has a lot of room for improvement, for example, we could do a more rigorous multi-dimensional scanning rather than three one dimensional scanning, or we could explore more parameters like the H₂ to CO₂ ratio and the pressure of the gas mixture, the current experimental results do not demonstrate the potential of this supercritical method to enhance the SABRE signal. The low efficiency of this supercritical SABRE method may result from competition between CO₂ and the hydride. Indeed, CO₂ can form bonds with certain transition metals by accepting electrons from the metal¹¹²⁻¹¹⁶. An anomalous experiment phenomenon supports this hypothesis – subsequent loading of CO₂ and H₂ into the sample tube rather than premixing them results in no hyperpolarized signal of both hydride and target nuclei. This observation could be attributed to the prior binding of CO₂ and substrate to the central metal of the catalyst, rendering the site unavailable for hydrogen activation and therefore inhibiting its competition with CO₂. Despite the absence of successful signal amplification, this method holds significant application potential. The easy isolation of the substrate by depressurizing the gas converts CO₂ from a supercritical or liquid state to a gas, facilitating its separation from the SABRE complex in solid state and the substrate in liquid state. Given that most SABRE catalysts and solvents are toxic or biologically

intolerable, direct injection of the hyperpolarized sample into human or animal body for nuclear magnetic imaging is unfeasible. Consequently, this facile isolation of the substrate could broaden the scope of SABRE application in biomedical and clinical fields.

4.4 Combination of High-pressure and Oscillating Pulse

We have presented two distinct strategies for enhancing the SABRE signal. The first involves utilizing an oscillating pulse in place of a static field to improve the efficiency of spin order transfer during the quantum evolution process. The second involves augmenting the accessibility of the spin source, parahydrogen, to enhance the efficiency of the chemical exchange process. An important question that naturally arises is whether the integration of these two methods can further amplify the polarization of the signal. To address this query, a numerical simulation can be employed to obtain an answer. The SABER system employed in the simulation is the 3-spin AA'B system, previously detailed, where the J-coupling between the two hydrides is $J_{HH} = -8\text{Hz}$, the J-coupling between the target nucleus and the hydride is $J_{HL} = -25\text{Hz}$, and the catalyst to substrate concentration ratio is $\frac{[C]}{[S]} = \frac{1}{10}$. The simulation which depicts the polarization build-up

process (depicted in Figure 4.14) investigates four distinct scenarios: (1) the use of an oscillating pulse SABRE for an open system (represented by the blue curve), (2) the implementation of an oscillating pulse SABER for a closed high-pressure system (depicted by the red curve), (3) the utilization of high-pressure CW SABRE-SHEATH (represented by the green curve), and (4) the application of conventional SABRE-

SHEATH (represented by the black curve). In the open system, the gas pressure is low (~ 7 bar), resulting in a significantly lower exchange rate of the dihydride $k_H = 2s^{-1}$ compared to the substrate $k_L = 18s^{-1}$, while in the high-pressure case, because

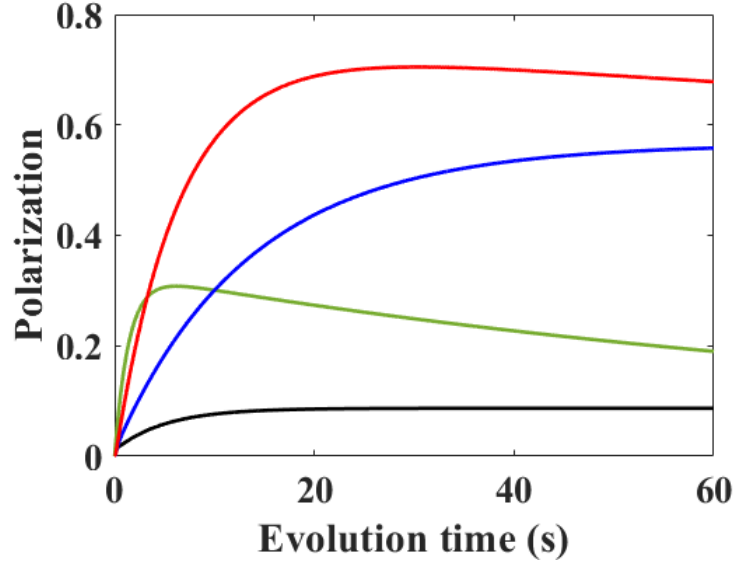


Figure 4.14: Signal build-up curves of four different scenarios. Red curve: oscillating pulse SABRE for a closed high-pressure system. Blue curve: oscillating pulse SABRE for an open system. Green curve: constant wave SABRE-SHEATH for a closed high-pressure system. Black curve: constant wave SABRE-SHEATH for an open system.

of the high concentration of the dissolved hydrogen gas, $\frac{[C]}{[H]} = \frac{1}{1000}$, we assume the exchange rate of the hydride and the substrate are approximately equivalent. In the case of oscillating SABRE, the optimal condition $\sqrt{M_0^2 + N_0^2} \approx 0.066$ is implemented using the most basic square pulse, characterized by a pulse amplitude of $B = 10\mu T$ and a pulse period of $T = 4ms$. Additionally, the optimal offset field $B_0 = -0.13\mu T$ established in Chapter 3 is applied. Whereas, for the conventional SABRE, the optimal field

$B_0 = -0.6\mu T$ is employed. The simulation has not taken into account the effects of relaxation and the inductance effect of the solenoid coil. The comparison of the four cases shown in Fig. 4.14 indicates that a combination of oscillating pulse and high-pressure hydrogen gas is able to boost the polarization higher.

In the previous simulation, the substrate's exchange rate is held constant at a given value $k_L = 18s^{-1}$. However, it is noted that this rate is temperature-dependent and can be modulated by applying temperature control. Through varying the temperature of the SABRE sample, the exchange rate of the hydrides and the substrate, which are presumed to be identical under a condition of high hydrogen gas concentration, can be equivalently modified. Fig. 4.15 illustrates the processes of signal accumulation corresponding to various exchange rates. It should be noted that the high-pressure SABRE system utilized in this study employs an optimal square pulse, as previously mentioned. At lower exchange rate, such as $k_H = k_L = 1s^{-1}$, the polarization accumulation process is relatively gradual. However, at higher exchange rates, such as $k_H = k_L = 25s^{-1}$, this composite approach forfeits its effectiveness and fails to produce higher polarization compared to the individual oscillating pulse SABRE method. By precisely controlling the temperature, we can identify the optimal exchange rate that generates the highest polarization, which is $k_H = k_L \simeq 5s^{-1}$. Theoretically, the composite method is capable of generating polarization levels up to eight times higher than those achieved by the conventional SABRE-SHEATH approach. Nevertheless, in practical experiments, several factors such as field inhomogeneity, inductance effect of the solenoid coil, and other

experimental imperfections, can result in significant reductions in observed polarization levels. All the theoretical analysis presented in this section requires experimental validation in the future.

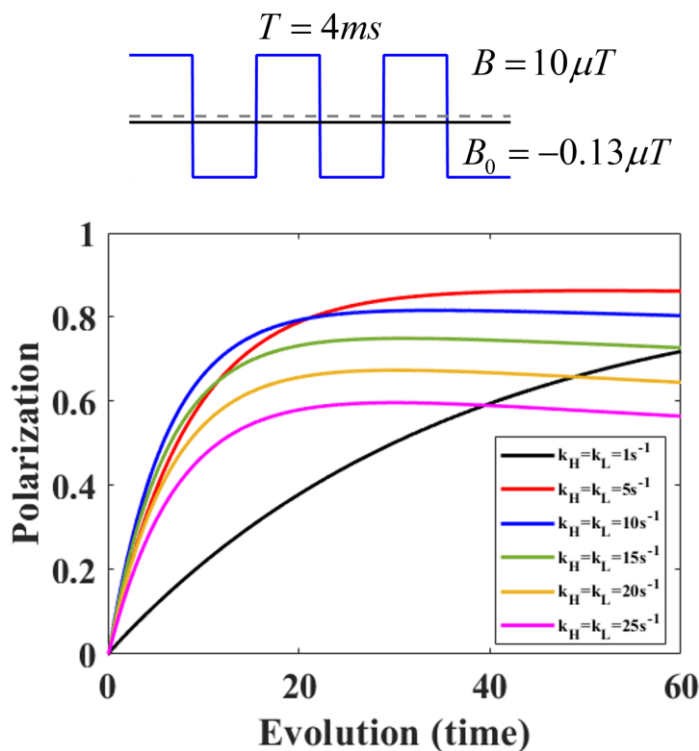


Figure 4.15: Polarization build-up process with respect to different exchange rates.

4.5 Conclusion and Outlook

In this chapter, we introduce a novel approach for improving the SABRE signal by increasing the exchange rate of the dihydride via elevated levels of dissolved hydrogen gas. To enhance the solubility of hydrogen, we explored two distinct methods. The first method, brute-force high-pressure SABRE, involved simply increasing the pressure of hydrogen gas, which led to a more than three-fold increase in the SABRE signal. The second method, creating a supercritical SABRE solution which is accordingly

miscible with hydrogen gas, failed to boost the SABRE signal due to the competition between the CO₂ used as the SABRE solvent and hydrogen gas, which reduced the efficiency of spin order transfer. To further improve the polarization level, we combined the high-pressure method with the oscillating pulse method presented in the previous chapter, and numerically demonstrated the potential for an even greater enhancement. Moving forward, we aim to experimentally validate the effectiveness of this composite method and attempt the supercritical method with different catalysts or solvents. By identifying a catalyst that can prevent CO₂ from competing with hydrogen gas in bonding, which is not impossible because we have already observed that the phosphorus catalyst works much better than IMes catalyst, or by discovering a better supercritical solvent that does not interfere with the SABRE process, we can significantly enhance the efficacy of the supercritical method. Until now, the observed increase in the generation rate of the triplet HD signal with increasing hydrogen gas pressure provides support for our hypothesis that the exchange of the dihydride also increases. To confirm this experimentally, we plan to use the 2D EXSY (EXchange SpectroscopY) method to accurately measure the exchange rate in the future.

Chapter 5: Attempt to Polarize Xenon with SABRE

5.1 Motivation

Xenon has unique physical and chemical properties that make it useful in a variety of applications^{117, 118}. Hyperpolarized xenon could be used as a contrast agent in MRI to enhance the images of the lungs, allowing for better visualization of lung function and the detection of lung diseases. In gas-phase NMR, hyperpolarized xenon can be used to study the surfaces of materials such as catalysts, zeolites, and polymers, providing valuable insights into their structure and reactivity. Furthermore, hyperpolarized xenon can also be used in environmental research to study air-sea exchange and atmospheric chemistry. Overall, hyperpolarized xenon has the potential to advance our understanding of a range of scientific and medical fields, making it an important area of research. Nowadays, the most common method to hyperpolarize xenon is Spin Exchange Optical Pumping (SEOP). The process of SEOP begins by introducing a mixture of rubidium or cesium vapor and xenon into a sealed container with a buffer gas. The container is then placed in a strong magnetic field, typically on the order of several Tesla. Next, circularly polarized light is shone onto the mixture at a specific wavelength that matches the resonant frequency of the alkali metal atoms. This excites the atoms, causing them to emit photons that are absorbed by noble gas atoms. The noble gas atoms then undergo spin exchange collisions with the polarized alkali metal atoms, transferring their spin polarization to the noble gas atoms. This process leads to a buildup of polarization in the noble gas, resulting in hyperpolarization. However, SEOP is an extremely costly method, which makes it prohibitive for most applications. SEOP requires specialized equipment

such as high-power lasers and strong magnetic fields, which can be expensive to purchase and maintain. These systems need to be precisely calibrated and maintained to ensure optimal performance, which can add to the cost. Moreover, the process of hyperpolarizing noble gases using SEOP is time-consuming and requires a significant amount of energy. The polarization process can take several hours or even days to complete, depending on the desired level of polarization, which can drive up energy costs.

In contrast, SABRE is a relatively rapid and cost-effective method for hyperpolarization. Successful hyperpolarization of xenon using SABRE could greatly expand the application of this noble gas. So far, SABRE has demonstrated successful hyperpolarization of hundreds of different organic molecules; however, the hyperpolarization of noble gases has not yet been achieved. Noble gases are known to be inert and difficult to react, as they have complete outer electron shells. Take ^{129}Xe as an example, whose electron configuration and orbital diagram are shown in Fig. 5.1. Noble gases are known for their very low reactivity due to their stable electronic configurations, with complete outermost electron shells. This stable configuration makes it difficult for them to lose or gain electrons and form chemical bonds with other elements. However, despite being a noble gas, xenon has been found to be capable of reacting chemically under certain conditions. This is due to the fact that, although xenon has a complete outer shell, it has an outermost electron shell that is relatively large and diffuse, which makes it possible for xenon to interact with other elements and molecules in specific ways that can lead to chemical reactions^{119, 120}. One such way that xenon can react is through the formation of weak chemical bonds, such as van der Waals forces, between its outer

electrons and other molecules or ions. These weak bonds allow xenon to form compounds with certain elements, such as fluorine, oxygen, and nitrogen, under specific conditions. Another way that xenon can react is through the process of ionization, where it loses one or more electrons to become a positively charged ion. The resulting xenon ions can then react with other ions or molecules to form chemical compounds.

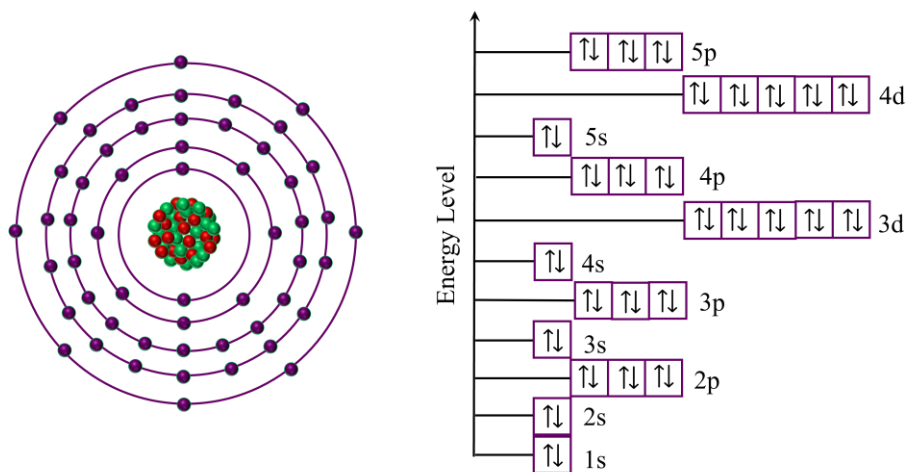


Figure 5.1: Electron configuration of xenon.

Since 1962, hundreds of noble gas compounds have been synthesized¹²¹⁻¹²⁶. In 2000, a metal-xenon compound with xenon directly binding to gold was created¹²⁷, demonstrating the possibility of xenon-metal bonding. While the formation of chemical bonds between xenon and transition metals is relatively rare and often requires specific conditions, it is possible and has been observed in a number of different compounds¹²⁸⁻¹³². Such bonding is a precondition for the hyperpolarization of xenon using SABRE, as the target substrate and the parahydrogen must bind to the metal center of the catalyst in SABRE. Therefore, the creation of xenon-metal bonding has opened up the possibility of hyperpolarizing xenon with SABRE.

5.2 Current Experimental Observations

Given the limited understanding of the iridium-xenon bond, we tried the simplest SABRE method first, continuous wave SABRE-SHEATH, to test whether SABRE could potentially achieve successful polarization of xenon. Three different SABRE catalysts (shown in Fig. 5.2) were available for testing, and each was tried separately using a high-pressure setup, which allowed for gas pressure adjustment and easy recycling of xenon gas. The experimental procedure was as follows: (1) The high-pressure sample tube was filled with 250 μ L of SABRE solvent and 1 mg of one of the SABRE catalysts. (2) Pure xenon gas was then loaded into the tube and pressurized to 50 bars. (3) The tube was then loaded with parahydrogen and pressurized to 200 bars, shaken vigorously to achieve a homogeneous solution. (4) The tube was sealed and left for at least 30 minutes to fully activate the catalyst. (5) The solution was then frozen by immersing the sample tube in liquid nitrogen, and then hydrogen gas was released. (6) Till the sample warmed up to room temperature, fresh parahydrogen gas was then reloaded into the tube and pressurized to 200 bars again. Subsequently, sealed the tube and vigorously shook it for a couple of minutes. (7) A CW SABRE-SHEATH experiment was performed, with the magnetic field and sample temperature varied, but unfortunately, no hyperpolarized signal was detected.

However, an unexpected phenomenon was observed during the experiment. After the addition of xenon gas but before the introduction of hydrogen gas, the dark red solution containing the first catalyst (Fig. 5.2(a)) lost its color and turned pale yellow. This fading effect was unique to the first catalyst and was not observed with the other two

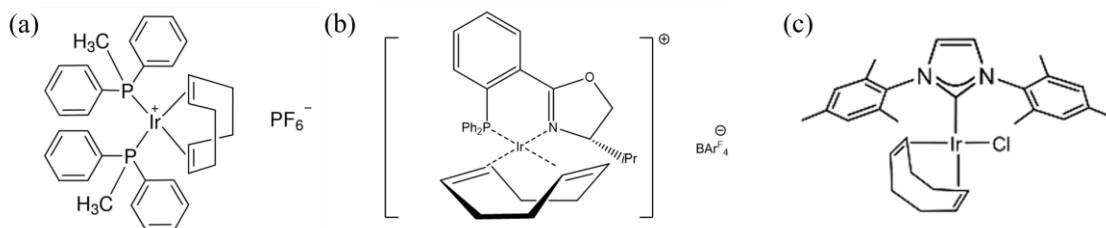


Figure 5.2: Molecular diagram of the three available SABRE catalysts.

catalysts. The color change was verified using the UV-Vis method, as demonstrated in Fig. 5.3(a), which compares the absorption spectra of the sample before and after the addition of xenon gas. In the absence of xenon, the red curve exhibits absorption of blue and ultraviolet light and therefore appears red. In contrast, the black curve in the presence of xenon absorbs a small portion of blue light and ultraviolet light, and thus appears pale yellow. However, upon closer inspection of the absorption peaks in Figure 5.3(b), it can be observed that both samples absorb light of the same wavelength, with only differences in the amount of absorption.

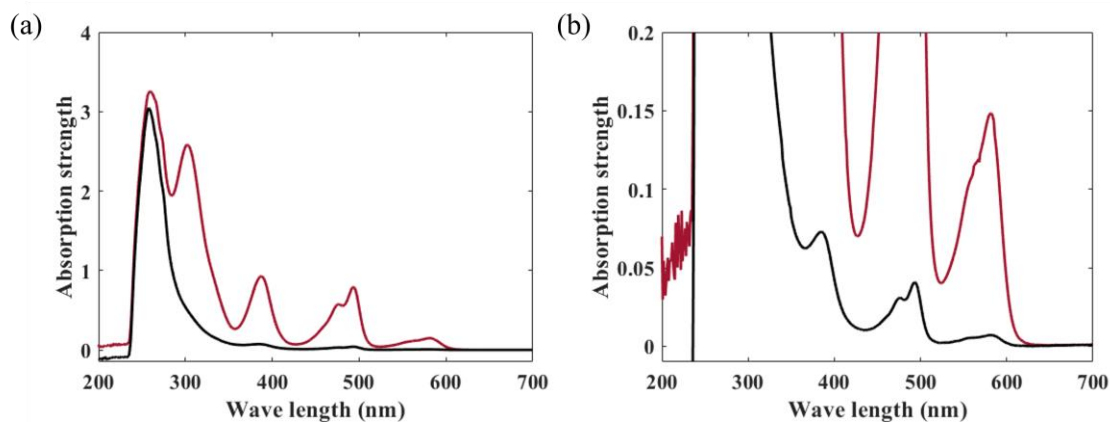


Figure 5.3: (a) A comparison of the absorption spectra of the sample before (red) and after (black) the addition of xenon gas. (b) Zoomin of the absorption peaks.

The color change in the SABRE solution suggested that the chemical bonds associated with the central metal underwent a change. Typically, in the activation process of SABRE, the cyclooctadiene moiety is hydrogenated and removed from the Iridium complex, resulting in a colorless and transparent liquid. However, in this case, the color change was caused by the introduction of xenon gas since hydrogenation could not occur before the addition of hydrogen gas. To investigate the effect of xenon gas, the proton spectrum of the sample was compared with and without xenon. The solvent used was a liquid mixture of 150 μ L DMSO-d₆ and 100 μ L methanol-d₄, because the catalyst has low solubility in pure methanol but is relatively more soluble in DMSO, while xenon has low solubility in DMSO but is relatively more soluble in methanol. The upper green spectra in Fig 5.4 represent the sample after the addition of xenon, while the lower red spectra represent the sample before the addition of xenon. The peaks ①, ②, and ③ in the lower spectrum of Fig 5.3(a) belong to the aromatic group in the catalyst; the peaks ④, ⑦, and ⑧ belong to the cyclooctadiene moiety; The peak ⑨ refers to the methyl group in the catalyst; The peaks ⑤ and ⑥ are the residual methanol and DMSO, respectively. The only peak in the lower ³¹P spectrum is represents the ³¹P atom binding to the iridium center. The significant difference between these spectra suggests that xenon reacted with the catalyst, resulting in the observed color fading. Therefore, in addition to the free species of xenon, there should also exists a bound species of xenon in some compounds, even though the concentration of which is low. However, only the signal of the ¹²⁹xenon atom was detected (illustrated in Fig. 5.5), and no bound species was observed as expected even after a frequency range of thousands of ppm. This may be

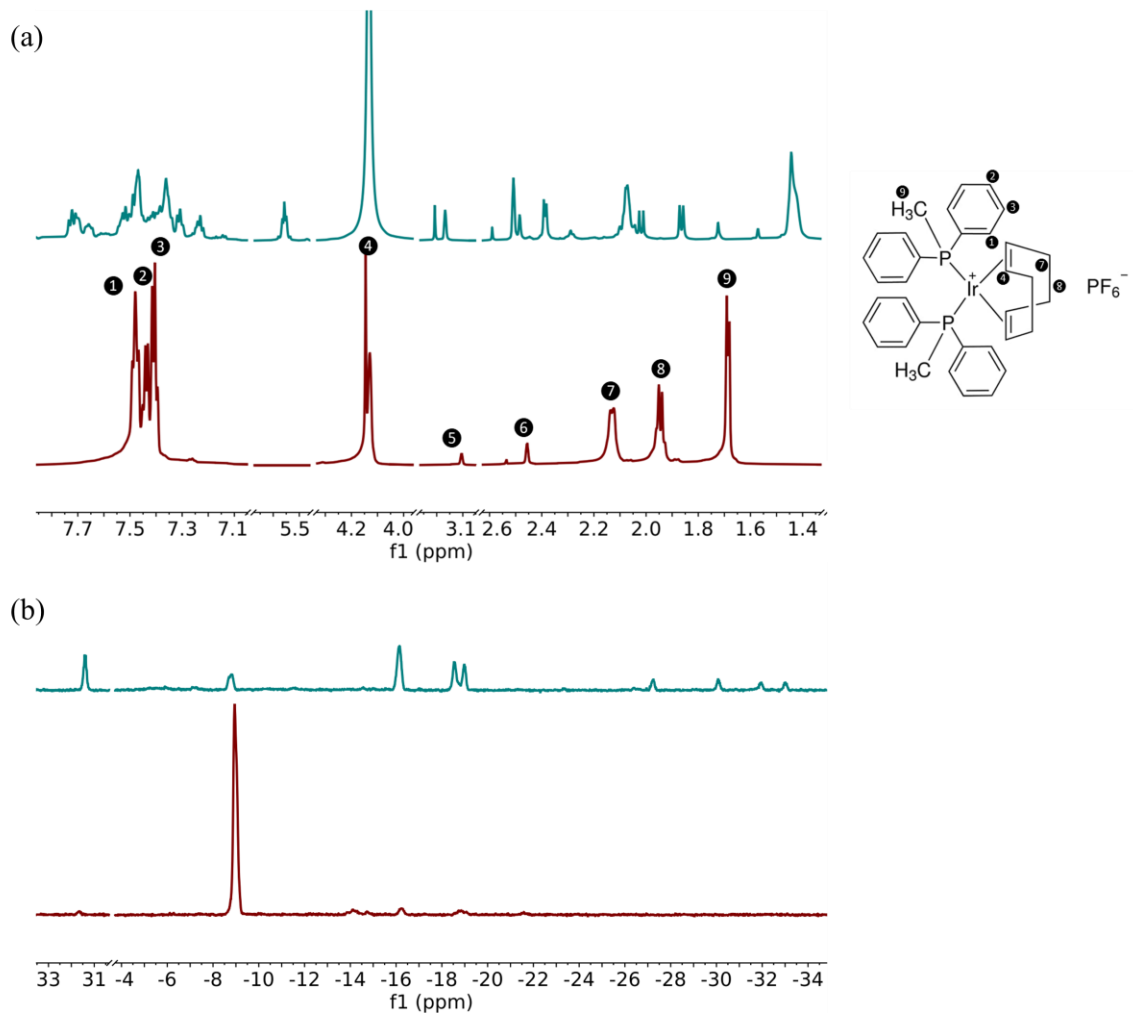


Figure 5.4: (a) Proton spectra and (b) ³¹P spectra of the SABRE sample before (upper) and after (lower) the addition of xenon.

because the sample concentration is too low, resulting in an extremely low signal to noise ratio. Or it could be because the exchange rate between the bound and free xenon is too fast, causing two signals to merge into one. More efforts are needed to reveal the truth.

To figure out the configuration of the SABRE complex in the presence of xenon, we executed several more experiments. Fig. 5.6 illustrates (a) the ³¹P decoupled proton spectrum and (b) the proton decoupled ³¹P spectrum of the SABRE sample in the

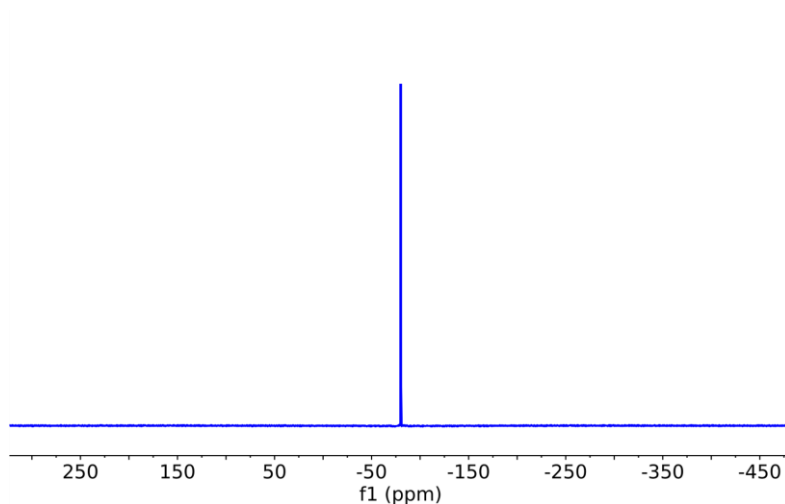


Figure 5.5: Xenon spectrum of the SABRE sample. Only the free xenon atoms are observed.

presence of the xenon. The decoupling method²⁸ used here is a typical technique in NMR to simplify the spectrum of coupled spins, which nullifies the coupling effect by applying a on resonant radiofrequency pulse to one of the spins in the coupled system to induce a transition between two energy states of the spin. In Fig. 5.6(a), Only the protons in the blue box have detectable coupling with the ^{31}P nuclei since they are simplified from doublet to singlet with the decoupling of ^{31}P , thus these protons must come from the catalyst complex which is the only molecule including ^{31}P . In Fig. 5.6 (b), all the peaks are narrower and have less splitting, which means that each ^{31}P couples with some protons, which is expected.

We next used 2D NMR spectrum to reveal more information about the couplings and components of the sample. The two methods we tried here are COSY and

DOSY. COSY, which stands for COrrrelation SpectroscopY, is used to identify correlations between different types of protons in a molecule. In a 2D COSY spectrum,

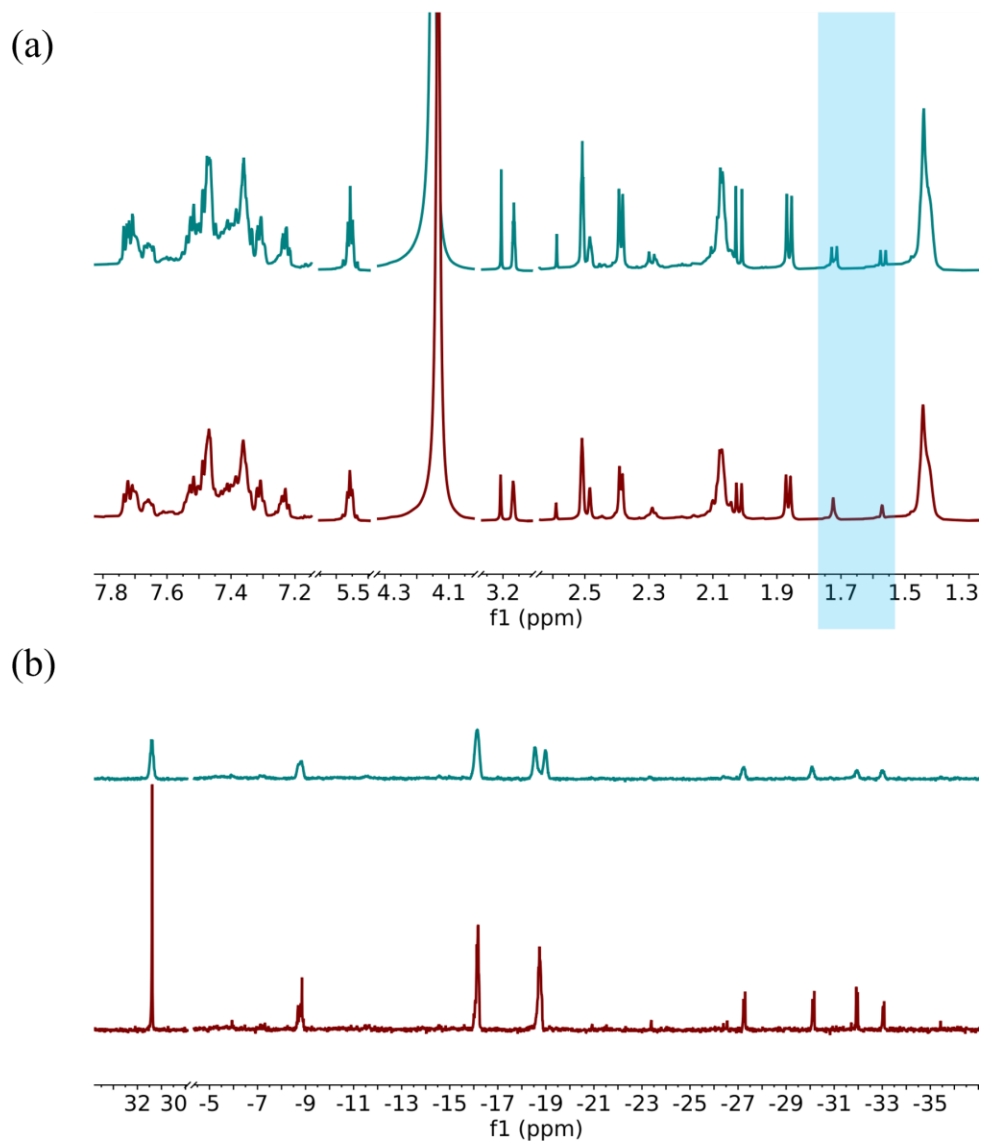


Figure 5.6: Illustrations of (a) the ^{31}P decoupled proton spectrum and (b) the proton decoupled ^{31}P spectrum of the SABRE sample in the presence of the xenon.

correlations between protons can be seen as cross-peaks on a two-dimensional plot with

one axis representing the frequency of one proton type and the other axis representing the frequency of another proton type, which allows for easier interpretation of the spectral data. The cross-peaks in the 2D COSY spectrum reveal the correlations between the two proton types. DOSY, which stands for Diffusion-Ordered Spectroscopy, provides information about the size and shape of molecules, by measuring the rates of diffusion of different components in a mixture. In a 2D DOSY spectrum, the signals are separated based on their diffusion rates with one axis representing the chemical shift and the other axis representing the diffusion coefficient. The diffusion coefficient provides information about the size and shape of the molecule, since larger molecules diffuse more slowly than smaller molecules.

Fig. 5.7 and 5.8 are the COSY and DOSY spectrum of the SABRE sample in the presence of xenon, respectively. The three grey dotted lines in Fig. 5.7 indicate three peaks whose protons couple with each other. Consequently, they belong to the same molecule. In Fig. 5.8, peaks that have the same diffusion coefficient belong to the same molecule. Dots in the red boxes have significant error, because the peaks they correspond to overlap with nearby peaks and the resulting integrals are imprecise. However, by closely looking at the rest of the peaks, we can still conclude that the peaks whose diffusion coefficients lie in the lower grey box all come from the catalyst, the dots in upper box are the solvent molecules (methanol and DMSO), and the dots lies in the middle box implies a new molecule generated after the addition of xenon, and this molecule most likely does not contain any phosphorus elements because the proton signals have no change after the decoupling of ^{31}P . So far, what we can be certain of is

the addition of xenon gas causes some part of the catalyst detaches and forms a new molecule. This research is still in progress and requires further investigation in the future.

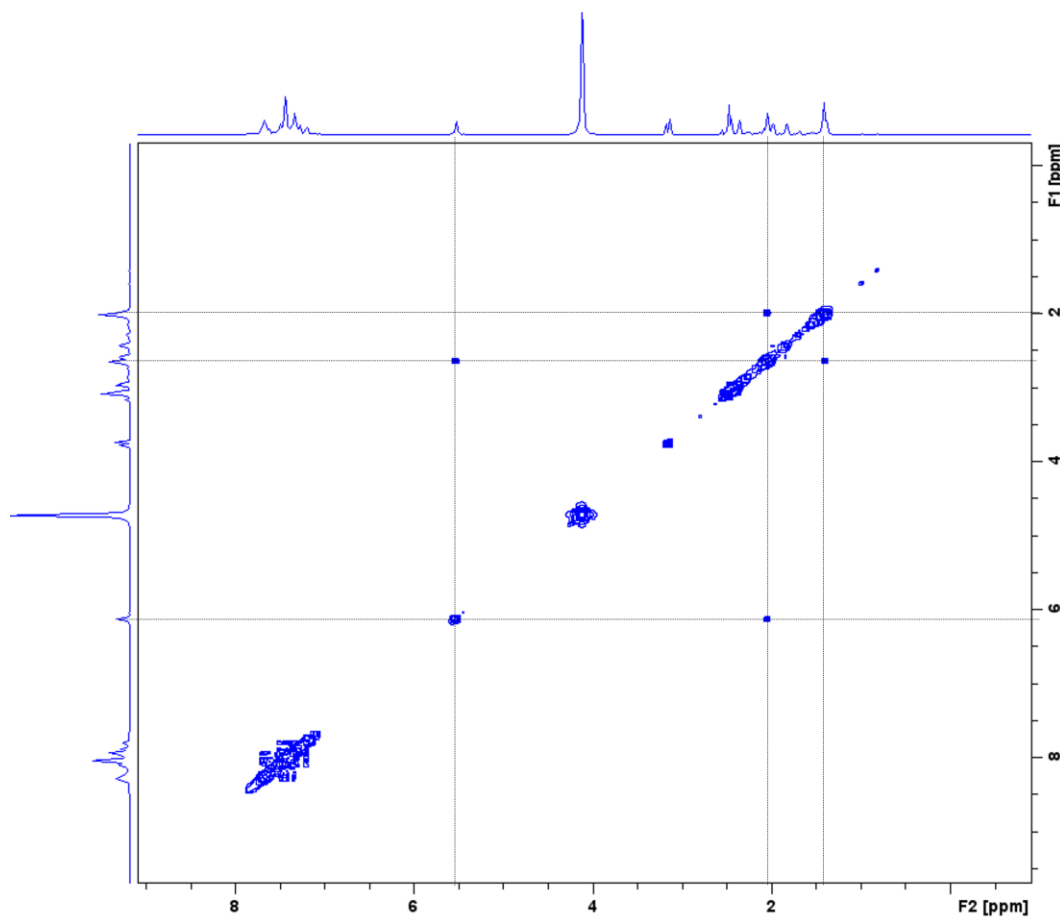


Figure 5.7: 2D COSY of the SABRE sample. The three grey lines connect the three peaks which are coupling together; therefore, they form the same molecule.

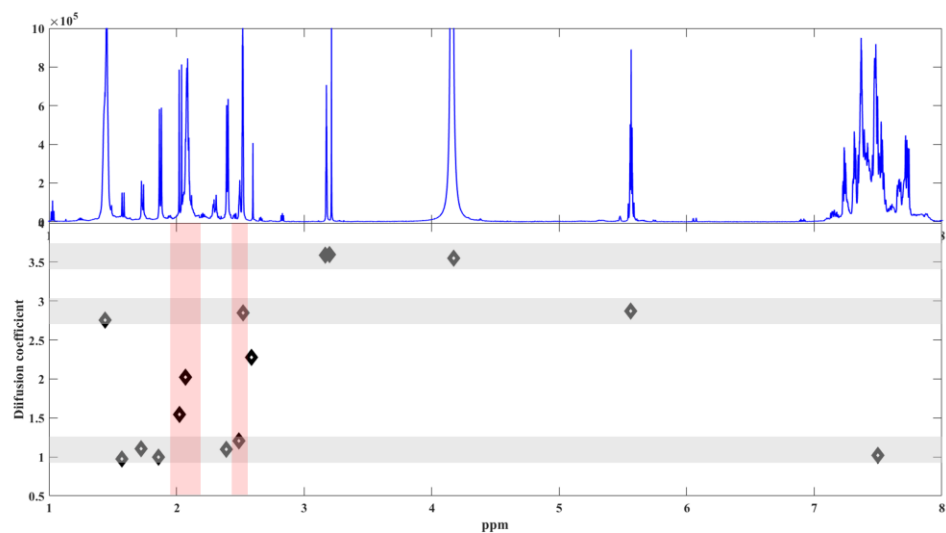


Figure 5.8: 2D DOSY of the SABRE sample. Peaks which have the same diffusion coefficient belong to the same molecule. Peaks lies in the three different grey bar indicate three different molecules. However, the peaks in the two red boxes have significant error, since they overlap with nearby peaks and the resulting integrals are imprecise.

Chapter 6: Conclusions

In summary, this study has provided various methods to improve the SABRE signal, including oscillating pulse SABRE, high-pressure SABRE, and their combination. The oscillating pulse SABRE could increase the polarization to more than three times that of the convention SABRE-SHEATH method. We have shown, in both experiments and simulations, that a variety of oscillating magnetic fields can significantly improve SABRE-SHEATH hyperpolarization, relative to a continuous field or even one pulsed to optimize polarization transfer. In effect, in a toggling frame the interactions between hydrides and target nuclei are adjustable by tuning the pulse amplitude and pulse period. Surprisingly, we observed that the optimal effective J-coupling between the hydrides and the target nuclei is significantly smaller than the actual coupling, with a coefficient of 0.066. In addition, the optimal magnetic field strength shifts from approximately 0.6 μ T in conventional SABRE-SHEATH to \sim 0.1 μ T. Notably, the highest level of polarization is independent of pulse shape, as any oscillation wave can exhibit an effective coupling strength between 0 and J_{HL} , depending on the pulse period and amplitude. However, it turns out that a pulse shape with reduced symmetry, such as a ramp wave, generates significant improvements in achievable polarization and is robust to experimental imperfections.

We have introduced two feasible methods to significantly increase the concentration of hydrogen gas for high-pressure SABRE. The first method involves increasing the pressure of the hydrogen gas, which can increase the solubility by tens of time. The second method involves using CO₂ to generate a supercritical SABRE solution

that is miscible with hydrogen gas. The brute-force method has successfully enhanced the SABRE signal by over 3 times at a gas pressure around 300 bar. However, beyond this pressure, the signal starts to decrease. Our hypothesis is that a too high concentration of hydrogen gas may deactivate the catalyst and reduce the effectiveness of SABRE. This hypothesis requires further experimental confirmation. The supercritical SABRE method has not yet produced a higher polarization to date, possible due to the competition between CO₂ and H₂ for bonding with the catalyst center. However, there is still potential for success with a more suitable catalyst or a more appropriate supercritical solvent. Numerical analysis has confirmed that by utilizing temperature control, a combination of the oscillating pulse method and the high-pressure method can effectively increase the polarization to a higher level.

Finally, we attempted to polarize ¹²⁹xenon using the SABRE method, with the aim of achieving a higher efficiency at a lower cost. While we have not yet achieved hyperpolarized xenon using SABRE, our experimental observations suggest that xenon did react with the catalyst and caused it to fade. This ongoing research remains unfinished, and further investigation will be conducted in the future.

According to our simulations, the SABRE-SHEATH method has the potential to achieve a maximum polarization of up to 80% (with 100% parahydrogen). However, in real-world applications, the polarization is constrained by the magnetic field's inhomogeneity and the self-inductance of the solenoid coil responsible for generating the oscillating pulse. This discrepancy between theory and practice suggests that there is still room for improvement in SABRE. Despite this, our approach is technologically

straightforward and has demonstrated significant enhancements, indicating that there is still potential for further exploration of the method.

References

1. K. H. Hausser and D. Stehlik, *Advances in Magnetic and Optical Resonance*. (1968).
2. J. H. Ardenkjaer-Larsen, B. Fridlund, A. Gram, G. Hansson, L. Hansson, M. H. Lerche, R. Servin, M. Thaning and K. Golman, *Proc. Natl. Acad. Sci. U. S. A.* **100**, 10158 (2003).
3. T. G. Walker and W. Happer, *Rev. Mod. Phys.* **69**, 629 (1997).
4. T. C. Eischenschmid, R. U. Kirss, P. P. Deutsch, S. I. Hommeltoft, R. Eisenberg, J. Bargon, R. G. Lawler and A. L. Balch, *J. Am. Chem. Soc.* **109**, 8089 (1987).
5. C. R. Bowers and D. P. Weitekamp, *J. Am. Chem. Soc.* **109**, 5541 (1987).
6. R. W. Adams, J. A. Aguilar, K. D. Atkinson, M. J. Cowley, P. I.-P. Elliott, S. B. Duckett, G. G.-R. Green, I. G. Khazal, J. Lopez-Serrano and D. C. Williamson, *Science* **323**, 1708 (2009).
7. K. D. Atkinson, M. J. Cowley, P. I.-P. Elliott, S. B. Duckett, G. G.-R. Green, J. Lopez-Serrano and A. C. Whitwood, *J. Am. Chem. Soc.* **131**, 13362 (2009).
8. L. D. Vazquez-Serrano, B. T. Owens and J. M. Buriak, *Inorg. Chim. Acta.* **359**, 2786 (2006).
9. M. J. Cowley, R. W. Adams, K. D. Atkinson, M. C.-R. Cockett, S. B. Duckett, G. G.-R. Green, J. A.-B. Lohman, R. Kerssebaum, D. Kilgour and R. E. Newis, *J. Am. Chem. Soc.* **133**, 6134 (2011).
10. T. Theis, M. L. Truong, A. M. Coffey, E. Y. Chekmenev and W. S. Warren, *J. Magn. Reson.* **248**, 23 (2014).
11. T. Theis, M. L. Truong, A. M. Coffey, R. V. Shchepin, K. W. Waddell, F. Shi, B. M. Goodson, W. S. Warren and E. Y. Chekmenev, *J. Am. Chem. Soc.* **137**, 1404 (2015).
12. X. Li, J. R. Lindale, S. L. Eriksson and W. S. Warren, *Phys. Chem. Chem. Phys.* **24**, 16462 (2022).

13. J. R. Lindale, S. L. Eriksson, C. P.-N. Tanner and W. S. Warren, *Sci. Adv.* **6**, 32 (2020).
14. J. S. Waugh, L. M. Huber and U. Haeberlen, *Physical Review Letters* **20 (5)**, 180-182 (1968).
15. H. Y. Carr and E. M. Purcell, *Physical Review* **94**, 630-638 (1954).
16. H. Oschkinat, C. Griesinger, P. J. Kraulis, O. W. Sorensen, R. R. Ernst, A. M. Fronenborn and G. M. Clore, *Nature* **332 (6162)**, 374-376 (1988).
17. A. Abragam, *The principle of nuclear magnetism*. (Oxford, Clarendon Press, 1961).
18. W. Gerlach and O. Stern, *Zeitschrift für Physik* **9(1)**, 349-352 (1922).
19. R. Shankar, *Principles of Quantum Mechanics*. (1980).
20. J. C. P. Slater, *Physical Review* **81 (3)**, 385-390 (1951).
21. I. I. Rabi, J. R. Zacharias, S. Millman and P. Kusch, *Physical Review* **53**, 318 (1938).
22. F. Bloch, W. W. Hansen and M. Packard, *Physical Review* **69**, 127 (1946).
23. E. M. Purcell, H. C. Torrey and R. V. Pound, *Physical Review* **69**, 37 (1946).
24. M. Born and R. Oppenheimer, *Annalen der Physik* **389 (20)**, 457-484 (1927).
25. E. M. Purcell and R. V. Pound, *Physical Review* **69 (1-2)**, 37-38 (1946).
26. N. F. Ramsey and E. M. Purcell, *Physical Review* **85**, 143 (1952).
27. C. P. Slichter, *Principles of Magnetic Resonance*. (Springer, 1990).
28. R. R. Ernst, G. Bodenhausen and A. Wokaun, *Principle of Nuclear Magnetic Resonance in One and Two Dimensions*. (Oxford University Press, 1987).
29. D. G. Cory and T. F. Havel, *Annual Review of Physical Chemistry* **52**, 275-297 (2001).

30. C. Kittel and H. Kroemer, *Thermal Physics (2nd Edition)*. (1980).
31. B. Cowan, *Nuclear Magnetic Resonance and Relaxation* (Cambridge University Press, 1997).
32. M. H. Levitt, *Spin Dynamics: Basics of Nuclear Magnetic Resonance*. (Wiley; 2nd edition, 2008).
33. J. W. Cooley and J. W. Tukey, *Math. Comp.* **19**, 297 (1965).
34. L. M. Jackman and S. Sternhell, *Applications of NMR Spectroscopy in Organic Chemistry*. (2nd edn., Pergamon Press, Oxford, 1969).
35. T. J. Batterham, *NMR Spectra of Simple Heterocycles*. (Wiley, New York, 1973).
36. A. L. Burlingame, H. M. Fales and R. J. Highet, *J. Am. Chem. Soc.* **86**, 4976 (1964).
37. O. Jardetzky and C. D. Jardetzky, *J. Am. Chem. Soc.* **79**, 5322 (1957).
38. M. Saunders and A. Wishnia, *Ann. N. Y. Acad. Sci.* **70**, 870 (1958).
39. F. A. Bovey, G. V. D. Tiers, G. Filipovich and J. Polym, *Science* **38**, 73 (1959).
40. A. Kumar, D. Welti and R. R. Ernst, *J. Magn. Reson.* **18**, 69 (1975).
41. L. Muller, A. Kumar and R. R. Ernst, *J. Chem. Phys.* **63**, 5490 (1975).
42. W. P. Aue, E. Bartholdi and R. R. Ernst, *J. Chem. Phys.* **64**, 2229 (1976).
43. O. W. Sorenson, G. W. Eich, M. H. Levitt, G. Bodenhausen and R. R. Ernst, *Prog. NMR Spectrosc.* **16**, 163 (1983).
44. D. J. States, R. A. Haberkorn and D. J. Ruben, *J. Magn. Reson.* **48**, 286 (1982).
45. D. Marion and K. Wuthrich, *Res. Commun.* **113**, 967 (1983).
46. A. Bax and R. Freeman, *J. Magn. Reson.* **44**, 542 (1981).
47. G. Bodenhausen, R. Freeman and G. A. Morris, *J. Magn. Reson.* **23**, 171 (1976).

48. G. Bodenhausen, R. Freeman, R. Niedermeyer and D. L. Turner, *J. Magn. Reson.* **24**, 291 (1976).
49. G. Bodenhausen, R. Freeman and D. L. Turner, *J. Chem. Phys.* **65**, 839 (1976).
50. R. Freeman, S. P. Kempell and M. H. Levitt, *J. Magn. Reson.* **34**, 663 (1979).
51. L. Muller, A. Kumar and R. R. Ernst, *J. Magn. Reson.* **25**, 383 (1977).
52. K. F. Morris and C. S. Johnson, *J. Am. Chem. Soc.* **114** (8), 3139-3141 (1992).
53. J. Jeener, B. H. Meier, P. Bachmann and R. R. Ernst, *J. Chem. Phys.* **71**, 4546 (1979).
54. P. C. Lauterbur, *Nature* **242**, 190 (1973).
55. M. P. Williamson, D. Marion and K. Wuthrich, *J. Mol. Biol.* **173**, 341 (1984).
56. M. P. Williamson, D. Marion and K. Wuthrich, *J. Mol. Biol.* **182**, 295 (1985).
57. J. R. Singer, *Science* **130**, 1652 (1959).
58. C. T. W. Moonen, P. C. M. v. Zijl, J. A. Frank, D. L. Bihan and E. D. Becher, *Science* **250**, 53 (1990).
59. R. L. Bowman and V. Kudravcev, *IRE Trans. Med. Electron.* **ME-6**, 267 (1959).
60. R. E. Halbach, J. H. Battocletti, A. Sances, R. L. Bowman and V. Kudravcev, *Rev. Sci. Instrum.* **50**, 428 (1979).
61. A. Farkas, *Orthohydrogen, Parahydrogen and Heavy Hydrogen*. (Cambridge University Press, London, 1935).
62. T. Jonischkeit and K. Woelk, *Adv. Synth. Catal* **346**, 960 (2004).
63. D. Canet, C. Aroulanda, P. Mutzenhardt, S. Aime, R. Gobetto and F. Reineri, *Concepts Magn. Reson. A* **28A**, 321 (2006).
64. M. L. Truong, T. Theis, A. M. Coffey, R. V. Shchepin, K. W. Waddell, F. Shi, B. M. Goodson, W. S. Warren and E. Y. Chekmenev, *J. Phys. Chem. C* **119**, 8786-8797 (2015).

65. J. R. Lindale, S. L. Eriksson, C. P.-N. Tanner, Z. Zhou, J. F.-P. Colell, G. Zhang, J. Bae, E. Y. Chekmenev, T. Theis and W. S. Warren, *Nat. Commun.* **10**, 395 (2019).
66. A. N. Pravdivtsev, A. V. Yurkovskaya, N. N. Lukzen, H.-M. Vieth and K. L. Ivanov, *Phys. Chem. Chem. Phys.* **16**, 24672-24675 (2014).
67. J. R. Lindale, C. P. Tanner, S. L. Eriksson and W. S. Warren, *J. Magn. Reson.* **307**, 106577 (2019).
68. S. S. Roy, G. Stevanato, P. J. Rayner and S. B. Duckett, *J. Magn. Reson.* **285**, 55-60 (2017).
69. S. Knecht, A. S. Kiryutin, A. V. Yurkovskaya and K. L. Ivanov, *Mol. Phys.* **117**, 2762-2771 (2019).
70. M. E. Gemeinhardt, M. N. Limbach, T. R. Gebhardt, C. W. Eriksson, S. L. Eriksson, J. R. Lindale, E. A. Goodson, W. S. Warren, E. Y. Chekmenev and B. M. Goodson, *Angew. Chem.* **59**, 418-423 (2020).
71. N. M. Ariyasingha, J. R. Lindale, S. L. Eriksson, G. P. Clark, T. Theis, R. V. Shchepin, N. V. Chukanov, K. V. Kovtunov, I. V. Koptyug and W. S. Warren, *J. Phys. Chem. Lett.* **10**, 4229-4236 (2019).
72. M. J. Burns, P. J. Rayner, G. G. Green, L. A. Highton, R. E. Mewis and S. B. Duckett, *J. Phys. Chem. B* **119**, 5020-5027 (2015).
73. V. V. Zhivonitko, I. V. Skovpin and I. V. Koptyug, *Chem. Commun.* **51**, 2506-2509 (2015).
74. J.-B. Hcvener, A. N. Pravdivtsev, B. Kidd, C. R. Bowers, S. Glcggler, K. V. Kovtunov, M. Plaumann, R. Katz-Brull, K. Buckenmaier, A. Jerschow, F. Reineri, T. Theis, R. V. Shchepin, S. Wagner, P. Bhattacharya, N. M. Zacharias and E. Y. Chekmenev, *Angew. Chem. Int. Ed.* **57**, 11140-11162 (2018).
75. J. F. Colell, A. W. Logan, Z. Zhou, R. V. Shchepin, D. A. Barskiy, G. X. O. Jr, Q. Wang, S. J. Malcolmson, E. Y. Chekmenev and W. S. Warren, *J. Phys. Chem. C* **121**, 6626-6634 (2017).
76. A. N. Pravdivtsev and J.-B. Hovener, *Chem. Eur. J.* **25**, 7659-7668 (2019).

77. S. L. Eriksson, J. R. Lindale, X. Li and W. S. Warren, *Sci. Adv.* **8**, 11 (2022).
78. L. Dagys, C. Bengs and M. H. Levitt, *J. Chem. Phys.* **155**, 154201 (2021).
79. A. N. Pravdivtsev, N. Kempf, M. Plaumann, J. Bernarding, K. Scheffler, J.-B. Hovener and K. Buckenmaier, *ChemPhysChem* **22**, 2379 (2021).
80. J. S. Waugh, *Solid State NMR Studies of Biopolymers*. (Wiley, 2010).
81. M. M. Maricq, *Phys. Rev. B* **25**, 6622_6632 (1982).
82. A. Brinkmann, *Concepts Magn. Reson. Part A* 2016 **45A**, c21414 (2017).
83. A. N. Pravdivtsev, A. V. Yurkovskaya, H.-M. Vieth, K. L. Ivanov and R. Kaptein, *Chem. Phys. Chem.* **14**, 3327-3331 (2013).
84. L. D. Landau, *Zur theorie der energieubertragung ii*, *Z. Sowjetunion* **2**, 46-51 (1932).
85. K. L. Ivanov, A. N. Pravdivtsev, A. V. Yurkovskaya, H.-M. Vieth and R. Kaptein, *Prog. Nucl. Magn. Reson. Spectrosc.* **81**, 1-36 (2014).
86. B. A. Rodin and K. L. Ivanov, *Magnetic Resonance* **1**, 347-365 (2020).
87. J. F. P. Colell, A. W. J. Logan, Z. Zhou, R. V. Shchepin, D. A. Barskiy, J. G. X. Ortiz, Q. Wang, S. J. Malcolmson, E. Y. Chekmenev, W. S. Warren and T. Theis, *J. Phys. Chem. C* **121**, 6626-6634 (2017).
88. E. Brunner, *J. Chem. Eng. Data* **30** (3), 269-273 (1985).
89. W. Henry, *Royal Society* **1** (1), 103-104 (1832).
90. D. Mackay and W. Y. Shiu, *Journal of Physical and Chemical Reference Data* **10**, 1175 (1981).
91. M. H. Hiatt, *J. Chem. Eng. Data* **58**, 902-908 (2013).
92. B. Berche, M. Henkel and R. Kenna, *J. Phys. Studies* **13**, 3201-3209 (2009).
93. J. Cowan and J. Cann, *Nature* **333**, 259-261 (1988).

94. C. A. Eckert, B. L. Knutson and P. G. Debenedetti, *Nature* **383**, 313-318 (1996).
95. R. Kessel, M. W. Schmidt, P. Ulmer and T. Pettke, *Nature* **437**, 724-727 (2005).
96. D. Bolmatov, V. V. Brazhkin and K. Trachenko, *Nat. Commun.* **4**, 2331 (2013).
97. J. Chrastil, *J. Phys. Chem.* **86 (15)**, 3016-3021 (1982).
98. R. Span and W. Wagner, *Journal of Physical and Chemical Reference Data* **25**, 1509 (1996).
99. B. Finney and M. Jacobs, *Supercritical carbon dioxide - Wikipedia* (2010).
100. Z. K. Myltykbayeva, Z. T. Yeshova and M. B. Smaiyl, *Oil Shale* **39 (3)**, 217-240 (2022).
101. Z. Knez, E. Markocic, M. Leitgeb, M. Primožic, M. K. Hrnčić and M. Skerget, *Energy* **77**, 235-243 (2014).
102. M. Zhang, M. Dou, M. Wang and Y. Yu, *Journal of Molecular Liquids* **248**, 322-329 (2017).
103. L. M. Valenzuela, A. G. Reveco-Chilla and J. M. d. Valle, *The Journal of Supercritical Fluids* **94**, 113-122 (2014).
104. C. A. Ward, *J. Chem. Phys.* **79**, 5605 (1983).
105. S. K. Upadhyay, *Chemical Kinetics and Reaction Dynamics*. (2006).
106. G. L. Miessler, P. J. Fischer and D. A. Tarr, *Inorganic Chemistry 5th edition*.
107. X. Yao, X. Dong, Y. Zhao, J. Shen and M. Gong, *J. Chem. Eng. Data* **67 (9)**, 2128-2135 (2022).
108. B. E. Eaton, J. Stecki, P. Wielopolski and H. J. M. Hanley, *Journal of Research of the National Bureau of Standards* **86 (5)**, 419-427 (1981).
109. J. Liu, Z. Qin, G. Wang, X. Hou and J. Wang, *J. Chem. Eng. Data* **48 (6)**, 1610-1613 (2003).

110. S. H. Page, S. R. Sumpter and M. L. Lee, *J. Microcolumn Separations* **4 (2)**, 91-122 (1992).
111. S. Lebonnois, G. Schubert, T. Kremic, L. M. Nakley, K. G. Phillips, J. Bellan and D. Cordier, *Icarus* **338**, 113550 (2020).
112. D. H. Gibson, *Coordination Chemistry Reviews* **185-186**, 335-355 (1999).
113. C. Creutz and E. Fujita, *Carbon Management: Implications for R&D in the Chemical Sciences and Technology*. (National academies press, Washington, DC, 2001).
114. D. H. Gibson, *Chem. Rev.* **96 (6)**, 2063-2096 (1996).
115. M. Aresta, R. Gobetto, E. Quaranta and I. Tommasi, *Inorg. Chem.* **31 (21)**, 4286-4290 (1992).
116. C. S. Yeung and V. M. Dong, *J. Am. Chem. Soc.* **130 (25)**, 7826-7827 (2008).
117. J. G. Malm, H. Selig, J. Jortner and S. A. Rice, **65 (2)**, 199-236 (1965).
118. P. D. Harris and R. Barnes, *Anaesthesia* **63 (3)**, 284-293 (2008).
119. K. S. Pitzer, *Science* **139**, 414-415 (1963).
120. A. Frontera, *Molecules* **25**, 3419 (2020).
121. W. Grochala, *Chem. Soc. Rev.* **36 (10)**, 1533-1696 (2007).
122. H. H. Claassen, H. Selig and J. G. Malm, *J. Am. Chem. Soc.* **84**, 3593 (1962).
123. K. A. Goettel, J. H. Eggert, I. F. Silvera and W. C. Moss, *Phys. Rev. Lett* **62**, 665 (1989).
124. R. Reichlin, K. E. Brister, A. K. McMahan, M. Ross, S. Martin, Y. K. Vohra and A. L. Ruoff, *Phys. Rev. Lett* **62**, 669 (1989).
125. H. Guo and F. Zaera, *Nat. Mater.* **5**, 489 (2006).
126. L. H. Krouse, C. Hao, C. E. Check, K. C. Lobring, L. S. Sunderlin and P. G. Wenthold, *J. Am. Chem. Soc.* **129**, 845 (2007).

127. S. Seidel and K. Seppelt, *Science* **290**, 117 (2000).
128. C. C. Lovallo and M. Klobukowski, *Chem. Phys. Lett.* **368**, 589 (2003).
129. J. V. Burda, N. Runeberg and P. Pyykko, *Chem. Phys. Lett.* **288**, 635 (1998).
130. W. P. Hu and C. H. Huang, *J. Am. Chem. Soc.* **123**, 2340 (2001).
131. P. Pyykko, *Angew. Chem. Int. Ed.* **43**, 4412 (2004).
132. W. Grochala, R. G. Egdell, P. P. Edwards, Z. Mazej and B. Zemva, *Chem. Phys. Chem.* **9**, 997 (2003).